Development of new Strategies for Autonomous Space Surveillance and Tracking Cataloguing Systems

Guido Pedone

Contents

Acknowledgments

Abstract

The use of satellites is nowadays paramount in our daily life. The importance of these assets has grown so much, in the last 50 years, to make them indispensable for our sustenance.

Such a vital role in our societies makes those operative satellites a vulnerable target from external attacks and uncontrolled events such as collisions with Space Debris.

For this reason, the importance of *Space Situational Awareness* (SSA) is becoming a priority for most of the countries.

As of now, the principal threat to operative satellite missions is constituted by the presence of Space Debris. Their evolution in number and representation models are going to be presented in this Thesis. They will be used as population models to test the main algorithms together with real data from operational satellites.

The aim of the Thesis is to study the Cataloguing strategies for space objects. The Thesis itself is reinforcing the two main pillars of the cataloguing approach: the Catalogue Creation and catalogue Maintenance, from the point of view of observation scheduling. The first aims to generate a comprehensive catalogue of objects orbiting around the Earth. The latter studies their evolution in the future and possible observability. These two foundations will allow the sustainable development of Space Debris catalogues and the correct exploitation of the sensing resources.

This Thesis will show how a simple different approach to the cataloguing problem can lead to new strategies for the creation and maintenance of space object databases.

The first two chapters of the Thesis will explain the two main innovations that have been introduced in the scope of this work and is going to describe the general framework of observation scheduling for cataloguing.

The following chapters will describe in detail and present the results of the development of Catalogue Maintenance and Catalogue Creation strategies.

Finally, the last chapters will present the *Special Perturbations Orbit determination and Orbit analysis toolKit* (SPOOK) software framework that supported the development of the Thesis, the possible applications and use cases consequences of the previous chapters, and the conclusions.

Zusammenfassung

Die Verwendung von Satelliten ist heutzutage in unserem täglichen Leben von größter Bedeutung. Die Bedeutung dieser Vermögenswerte ist in den letzten 50 Jahren so stark gewachsen, dass sie unverzichtbar für unsere Existenz geworden sind.

Eine so wichtige Rolle in unseren Gesellschaften macht diese operativen Satelliten zu einem anfälligen Ziel für externe Angriffe und unkontrollierte Ereignisse wie Kollisionen mit Weltraummüll.

Aus diesem Grund wird die Bedeutung der SSA für die meisten Länder immer mehr zur Priorität.

Bis heute stellt die Hauptbedrohung für operative Satellitenmissionen die Anwesenheit von Weltraummüll dar. Ihre Entwicklung in Bezug auf die Anzahl und die Darstellungsmodelle werden in dieser Arbeit vorgestellt. Sie werden als Bevölkerungsmodelle verwendet, um die Hauptalgorithmen zusammen mit echten Daten von operativen Satelliten zu testen.

Das Ziel der Arbeit besteht darin, die Katalogisierungsstrategien für Raumobjekte zu untersuchen. Die Arbeit selbst stärkt die beiden Hauptpfeiler des Katalogisierungsansatzes: die Katalogerstellung und die Katalogpflege aus Sicht der Beobachtungsplanung. Die erste zielt darauf ab, einen umfassenden Katalog von Objekten zu erstellen, die die Erde umkreisen. Die letztere untersucht deren Entwicklung in der Zukunft und deren mögliche Beobachtbarkeit. Diese beiden Grundlagen ermöglichen die nachhaltige Entwicklung von Weltraummüllkatalogen und die korrekte Nutzung der Sensing-Ressourcen.

Diese Arbeit wird zeigen, wie ein einfacher, anderer Ansatz für das Katalogisierungsproblem zu neuen Strategien für die Erstellung und Pflege von Raumobjektdatenbanken führen kann.

Die ersten beiden Kapitel der Arbeit werden die beiden wichtigsten Innovationen erläutern, die im Rahmen dieser Arbeit eingeführt wurden, und den allgemeinen Rahmen der Beobachtungsplanung für die Katalogisierung beschreiben.

Die folgenden Kapitel werden im Detail beschreiben und die Ergebnisse der Entwicklung von Katalogpflege- und Katalogerstellungsstrategien vorstellen.

Schließlich werden die letzten Kapitel das SPOOK-Software-Framework vorstellen, das die Entwicklung der Arbeit unterstützt hat, die möglichen Anwendungen und Auswirkungen der vorherigen Kapitel sowie die Schlussfolgerungen.

List of Figures

List of Tables

List of Acronyms

List of Variables

The following list of symbols encompasses the most frequently used variables in this Thesis along with their respective meanings. It is, however, crucial to note that all these variables will be thoroughly described within the text when they are first introduced, referenced, or mathematically derived. Some of these symbols may have different interpretations when taken out of their context. Hence, it is important to pay attention to their indexing, as well as whether they are used as vectors (highlighted in bold) or scalars.

Symbol	Description
$\varnothing$	Diameter (or main dimension).
i	Orbital inclination angle.
Ω	Right ascension of the ascending node angle.
α	Celestial right ascension.
δ	Celestial declination.
λ	Latitude of the observer.
h	Object Altitude angle.
El	Object Elevation angle.
Az	Object Azimuth angle.
$\boldsymbol{x}$	Object state vector.
σ	Variance of a state element.
$\boldsymbol{K}$	Covariance matrix of the object state vector.
$K_{x_i x_j}$	Covariance associated with the ith and j^{th} of the state vector $\boldsymbol{x}$.
B_i	Benefit of an observation schedule at time i.
b_i	Benefit of a single observation task at time i.
$\hat{f}_t$	Probability density function estimate at time t.
$\mathcal{N}(x_i, m_i, K_i)$	Normal distribution evaluated in x_i, conditioned by the mean m_i and covariance K_i.
ω_i	Weight of the kernel i in a Gaussian Mixture.
$f_{k\|k-1}$	Prior density function of the time k.
g_k	Likelihood density function at time k.
p_k	Posterior density function at time k.

$\boldsymbol{X}_k$ list of objects of a Gaussian Mixture at time k.

$\boldsymbol{K}_k$ list of measurements of a Gaussian Mixture at time k.

ν_k Posterior intensity function at time k.

J_k Estimated number of components in a Gaussian Mixture at time k.

$\boldsymbol{F}_k$ State transition matrix at time k.

$\boldsymbol{Q}$ Process noise.

$\boldsymbol{\Psi}$ CPHD vectorial functions.

$\boldsymbol{S}$ Uncertainty defined by the unscented transformation.

$\boldsymbol{R}(u)$ Reward function associated with pointing task u.

p_D Probability of detection.

$\boldsymbol{A}$ Attributable vector.

Γ Covariance matrix of the attributable vector.

$\boldsymbol{r}_{obj}$ Cartesian coordinates of the object.

$\dot{\boldsymbol{r}}_{obj}$ Cartesian velocity of the object.

$f,\, g,\, \dot{f},\, \dot{g}$ Lagrange coefficients.

$\boldsymbol{\xi}$ Vector of the known variables in a linear system.

$\boldsymbol{pos},\, \boldsymbol{vel}$ Position and velocity of particles in a
particle swarm optimization context.

$\boldsymbol{W}$ Matrix of weights.

$\boldsymbol{LOS}$ Line of sight vector.

$\boldsymbol{R}$ Matrix of rotations.

$\boldsymbol{r},\, \boldsymbol{v},\, \boldsymbol{n}$ Position vector, velocity vector and normal vector to the orbit.

$\boldsymbol{u}$ Pointing vector.

$\boldsymbol{R}_{Earth}$ Earth's Radius.

"When you look at yourself from a universal standpoint, something inside always reminds or informs you that there are bigger and better things to worry about". —*Albert Einstein*

This Thesis takes place in the field of *Space Situational Awareness* (SSA) for the observation and cataloguing of space debris. It comprehends a work longer than three years done in Airbus Defence and Space GmbH in Friedrichshafen, Germany. The main topic of this work revolves around the sensor's observation strategies; how to optimize and automatize them. This chapter will provide the reader with general background knowledge of space debris to understand the motivation behind the selection of this topic and its importance for SSA.

1.1 Motivation - Cataloguing and Observation Strategies

Today, space debris is one of the principal threats to satellites. In order to avoid collisions with them, the orbits of objects in space must be known.

The goal of SST is to build-up and maintain a catalogue which contains information about the detected objects, such as their orbits and physical properties [10].

Monitoring and processing the catalogue data is a necessary step to schedule new observations in advance. This process is shown in Fig.1.1. The quality of products depends on several aspects of the entire *End-2-End* (E2E) SST chain: sensor accuracy and sensitivity, the number of sensors and their location, minimal and optimal timelines for observations and measurement collection, the fidelity of data processing (orbit determination, correlation methods) and fidelity of observation planning and scheduling. The aim of this dissertation focuses on the last task, to optimize observation strategies for several relevant use cases.
This Thesis work will try to overcome the dichotomy between cataloguing techniques and observation strategies. While the first is aiming in improving the cataloguing
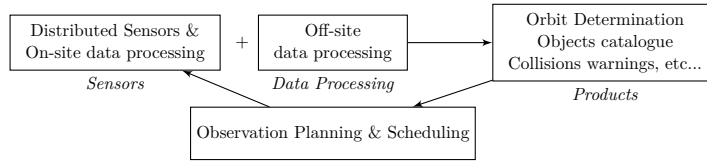
FIGURE 1.1: E2E chain of SST system.

pipeline that transforms the measurements into object information to append to a catalogue. The second tries, instead, to close the chain providing optimal methods to perform new observations. It will be shown how the previous research has proceeded in developing these two subjects separately, either improving the cataloguing techniques to make the best use of the observation data or optimizing the sensor scheduling to observe as many objects as possible.

This Thesis will try to seek some points of contact between these two sectors, in particular, some of the strategies and results utilized for cataloguing will be reproduced in a simulation environment and used for observation scheduling. This is the case of the *Finite Set Statistics* (FISST)-based multi-target filters, of great application in cataloguing pipelines to streamline the tracklet linking, correlation and orbit determination activities in a single step [19][7], that, for this work, has been adopted into a real-time single step simulation framework for *Catalogue Maintenance* (CM). The innovation, in this case, is to use a well-documented cataloguing tool inside a new framework, where the processed measurements are simulated of few instants of time ahead instead of being real, to find the best pointing position for a sensor, and eventually perform the new observation.

The second innovation of the Thesis is in the field of *Catalogue Generation* (CG) or Catalogue Creation. In this case, the *Constrained Admissible Region* (CAR) *Orbit Determination* (OD) theories from Milani [29] [11], which have been introduced for cataloguing purposes to improve correlation activities, will be translated into a new framework for observation scheduling. In this case, the orbital hypothesis generated by short arc observations, which are usually not enough for a proper catalogue initialization, are kept alive in a *virtual* catalogue and used to generate new observation tasks to observe again the objects that originated those measurements. This first chapter will introduce more in detail what is meant by the terms of CM and CG, why they are so important for SST, what are the current limits of the state-of-the-art, and how the new innovations are going to address those problems. Further innovations are going to be presented within this thesis, to highlight how some of the new methodologies can be applied to different scenarios and use cases. referring to Fig. 1.2, it is possible to see a simplified structure of the Thesis, to summarize to the reader what has been said in this first introduction. Inside the blue scope is collected the CM research and in the green one the CG. The overall structure is divided into three blocks which collect the key research questions and the Thesis innovations, the methodology and results and the possible development and use cases. The main body of the dissertation will be structured into three symbolic blocks: the key research question, the methodology and results, and the possible applications, use cases and validation of the Theories. The overall study can be divided into two main sub-subjects that are: CM and CG.

Key Research Questions	Autonomous Centralized Sensor Network → overcome the current limitations of offline planning and open loop cataloguing chain.	Information Sources → first time introduction of techniques for re-observation of unknown observed targets.
Methodology & Results	Simplified (single step) real-time Markov decision problem for closing the loop cataloguing-scheduling.	Deterministic study on tracklet follow-up: merging of the state-of-the-art correlation and IOD studies into statistical planning.
Possible Development and Use Cases	Studies for future sensor networks or constellations.	Fragmentation detections, Catalogue build-up, Survey planning, ...
	Catalogue Maintenance	*Catalogue Generation*

FIGURE 1.2: Structure of the Thesis.

1.1.1 Literature Review

In contrast to the extensive population of *Resident Space Object* (RSO)s, the number of sensors available for collecting independent information is relatively limited. The substantial relative velocity disparities between sensors and objects in various orbital regions hinder the simultaneous detection of a diverse range of objects, even if the sensor's field of view allows for it [39]. The challenge of optimizing the observation schedule relies on a complex convex representation. Achieving this task in real-time is a critical step toward enhancing the autonomy of both systems and sensors. From a ground-based perspective, the ability to control a network of sensors is essential for maintaining an up-to-date space debris catalogue. Typically, this is accomplished through centralized data processing and planning systems. Automating and optimizing such centralized systems is the initial step in improving the quality of the object catalogue. Conversely, granting more autonomy to sensors themselves has the potential to enhance on-board spacecraft detection and tracking strategies, as well as collision avoidance maneuvers. The current US space object catalogue contains approximately 22300 objects larger than 10 cm. As we move towards higher-resolution sensors, significantly larger detection numbers are anticipated, particularly

when considering smaller objects. Managing the discovery and tracking of all these objects poses a formidable challenge for a network of observers, which must optimize coverage not only for known (already catalogued) objects but also to maximize the detection of unknown ones. This task can be tackled through heuristic modeling, offering a wide array of potential solutions. To date, various research groups have independently explored this problem, and there is no universally preferred roadmap. C. Frueh's work in [17] and [25] attempts to consolidate the methods studied thus far. Traditionally, optimal survey and follow-up strategies have been developed for geosynchronous orbital regions [1] [43] [42] [31]. Similar strategies have been adapted for the low Earth region, particularly for radar sensors [9]. The importance of having an optimized scheduling system cannot be overstated, given that the number of sensors capable of independently collecting information is small compared to the vast amount of space debris. It is essential to avoid overloading systems with redundant tasks and instead make optimal use of available resources. Studies presented thus far indicate that real-time observation scheduling is feasible for at least some orbital ranges, representing the initial step toward future autonomous systems, whether centralized or on-board. Future mission proposals, especially those from *European Space Agency* (ESA), reflect an increasing interest in space-based assets for monitoring debris objects. Achieving autonomous detection of space targets necessitates a real-time scheduling system [32]. Such a system should operate without the need for external interaction, a characteristic that is currently dominant in almost all modern SST systems.

1.1.2   Key Research Questions

The primary objective of the latest SST research is to enhance the quality of the space debris catalogue in terms of:

- Completeness (increased object count),

- Accuracy (improved state vectors and covariances), and

- Frequency of updates (timely detection and revisits to detect transient events such as fragmentations or maneuvers).

This improvement should be achieved through enhanced observation planning and sensor scheduling without the need for substantial modifications to our existing hardware, computational power, and data processing loads. As of today, it is important to merge in a deterministic way, the knowledge gained in fields such as image processing, measurement collection and orbit determination methods with optimal observation strategies. For example, longer detection periods for objects yield more accurate results for in-orbit determination, while shorter detection periods enable more efficient correlation methods. Up to this point, the validation of sensor strategies has primarily relied on observation requirements (e.g., percentage of coverage, minimum time between two observations of the same object, and the minimum apparent magnitude for detection in the case of optical observers). *Deterministic* in this context refers to establishing a consistent alignment between sensor observation scheduling and the underlying physics principles. Ground-based

observations benefit from ample resources but face challenges in accessing certain orbital regions or objects of specific dimensions. Conversely, space-based sensors allow for in-depth study in densely populated LEO and GEO regions but are constrained by limited computational resources and steering capabilities. In both scenarios, optimizing observation strategies is critical, with the overarching goal of improving the aforementioned assets. This research aims to harness the latest optimization methods in the field to develop new heuristic algorithms capable of real-time observation scheduling. It also seeks to enhance existing methods, emphasizing the increased autonomy of this complex system. Furthermore, the study investigates the advantages of increasing sensor autonomy. It is important to clarify that a centralized autonomous system is one that can process SST products and autonomously generate schedules for a network of observers without external input, which has been the norm until now. In contrast, sensor autonomy refers to a sensor's ability to process the outputs of its observations to plan subsequent observation strategies. The goal of this thesis is to lay the foundation and conduct feasibility research for a fully autonomous sensor scheduler, applicable in both space-based and ground-based applications. This research will contribute to the validation of future prototype software systems and the evaluation of more straightforward remote monitoring and control techniques. To elevate the quality of SST products, including the quantity and accuracy of catalogued objects, as well as to support critical projects such as collision avoidance with on-board autonomous detectors and laser tracking-based stare and chase techniques (vital for debris deflection studies), an optimized automated data processing and observation planning chain is essential. Studies presented in the State of the Art section indicate that real-time observation scheduling is feasible for at least some orbital ranges, representing the initial step toward future autonomous systems, whether centralized or on-board. The key research questions addressed in this thesis are as follows:

1. How can we overcome the current limitations of offline planning and open-loop cataloguing chains to enhance scheduling autonomy for a network of sensors? The answer to this question, involving the adoption of the *Cardinalized-Probability Hypothesis Density* (CPHD) filter for single-step optimal sensor scheduling, will be presented in Chapter 3.

2. How can we effectively integrate the latest research in measurements correlation and orbit determination without the ability to follow-up objects that are not catalogued? The response to this question, covering post-processing and real-time follow-up techniques for unknown objects, will be provided in Chapter 4.

1.1.3 Methodology

The main project of the thesis will be focused on the implementation of the optimization algorithms for observations scheduling, both for ground and space observers (optical, radar, laser), with the goal to make it computationally in real-time. The implementation of an automatic scheduler will optimize both coverage and accuracy of targets. Afterwards the studies have been focused on the implementation of real-time test cases and simulations (eventually real testing with *Airbus Robotic*

Telescope (ART) [47]). Results from correlations techniques and images processing pipelines, will participate together with real-time autonomous sensor tasking to autonomously control the telescope interface. Different observation modes for catalogue creation have been tested at this step, from fences and stripes coverage techniques to stare-and-chase observation modes. All the development has been realized hand to hand with a dedicated visualization framework of the simulations and real observations. Results have been extended also to space-based observers, in different orbital regions and payload conditions, in order to create a baseline for future on-board autonomous space debris detection. The initial state of the art research took care of defining the most specific requirements for observations (mainly optical) to enhance both initial orbit determination of unknown objects, correlation and object characterization. Sensor properties and measurement processing requirements will be part of the new observation strategy definition. Attention will be given to GEO synchronous fence-survey strategies and LEO statistical sampling for debris model definition.

For the aforementioned use cases, it will be necessary to define a proper real-time scheduling technique able to most accurately exploit the sensor properties and optimize the SST products for different kind of objects. At this step, new algorithms exploiting probabilistic density function (PDF) for heuristic optimization will be developed.

Following, the optimization techniques for observation strategies will be implemented and applied to different scenarios (ground or space-based observers). In details, the literature review is focusing on the definition of Use Cases and optimization goals. In fact, sensor autonomy has the potential to enable completely new concepts of operations such as:

- Automatic follow-up of fast and faint small debris objects.

- Support of automated collision avoidance in space, e.g. for emerging Megaconstellations.

- Debris tracking and (potentially in the far-term) deflection via lasers.

Above examples apply to both ground-based sensors (often located in remote locations) and Space-based sensors (for which *Telemetry and Telecommands* (TMTC) often cannot be achieved 24/7).

After that definition, will be established and demonstrated a baseline (working with available facilities in Airbus) of an autonomous real-time observation scheduler for CM. Improvements of this baseline, based on results, has been performed and validated through simulations.

The developments will be integrated into the existing Airbus tool: *Special Perturbations Orbit determination and Orbit analysis toolKit* (SPOOK). SPOOK is a space debris cataloguing framework developed by Airbus Defence and Space in Immenstaad [36]. Inside such background SPOOK's measurement generator offers the possibility to simulate observations by arbitrary sensor networks. Additionally, access will be available to ART located in Spain. ART is an optical ground based sensor utilized for real world observations and automatically commanded from Immenstaad.

Besides the presented R&D activity, some external activities took place as tutoring

of Master Thesis and internship students, in order to collaborate together in specific SST improvements and presentation of the works during university seminars and international conferences.

1.2 Preface on Space Debris

The activity of men in Space set up incredible achievements for the development of modern life. The operations of active satellites in space are vital for most people's daily life. Unfortunately, the sustainability of the space environment is threaded by the presence of uncontrolled objects such as space debris.

Modern statistical models [10] estimates about 130 million space debris between $1\,\mathrm{mm}$ and $1\,\mathrm{cm}$ are currently present in orbit. The collision of even these small fragments with operative satellites may compromise their activities, due to high relative velocities and delicate appendices. Some orbital regions are already reaching their operational capacity and safety standards need to be constantly updated.

The first aim of SST is to catalogue most of these uncontrolled objects and offer anti-collision services to satellite operators. However, this task is becoming a great challenge for most of the current services. In late 2021 already the well-known *North American Aerospace Defense Command* (NORAD) cataloguing system for *Two Lines Element* (TLE) has been deprecated to allow the introduction of a 9-digits based identifications due to the increased number of tracked satellites [23].

To have an idea of the weight of space debris in the orbital framework it is necessary to consider that over the c.a. 37290 currently tracked and maintained satellites by the *Space Surveillance Network* (SSN), only 5800 are known active satellites still functioning and 31490 are debris. In such a scenario, close conjunctions between them are at the order of the day, with around 630 collisions resulting in fragmentation detected so far.

1.3 Cataloguing and Observation Strategies

As introduced in the previous sections, this Thesis will start studying the cataloguing and observation strategies with the final goal of merging them to increase their operability. It is, however, important to this step to give a definition of the two research sectors.

With Cataloguing it is meant the data processing activities that transforms the measurements into object's information. Parts of the cataloguing activities, as represented in Fig. 5.2, are:

- *Image Processing*: that comprehends all the techniques to process raw optical or radar images into measurements. In case of optical images, the techniques that is usually adopted is astrometry reduction, where the stars in the background are recognized and matched to the real star to increase the accuracy of the measurements.

- *Tracklet-Linking*: it concerns all the processes to prune the measurements as result after image processing. Tracklet-linking has the duty to collect more images and recognize which of the feature has a typical object behaviour (e.g.

same direction, constrained angular velocity, etc.). The result of this task is the creation of tracklets, single elements that collects measurements coming from the same object.

- *Tracklet-to-Catalogue Correlation*: this task can be also referred as data association. The tracklets are attempted to be associated to object inside a catalogue.

- *Tracklet-to-Tracklet Correlation*: when the previous step is failing, the resulting uncorrelated tracklets are associated between each other, to see if more tracklets may have been generated by the same object.

- *IOD*: a batch of tracklets associated between each other can be used at this step to compute a first guess of the object orbit that originated them. If successful, a new instance is added to the catalogue.

- *OD*: the last step of the cataloguing pipeline is the refinement of the orbits inside a catalogue by using an estimation filter. As soon new measurements are available for an object inside a catalogue, they are used to refine its orbit state vector and covariance.

Cataloguing activities are very important for SST systems. Currently, they have also a lot of constraints in terms of required computational resources and performances with big catalogues. The correlation methods, for example, are pure combinational problems, which computational time is inversely proportional to the dimension of the system. However, the more are the tracklets and objects combined, the more efficient will result the algorithm. The all nature of the cataloguing problem is stochastic. While the canonical state-of-the-art for cataloguing is considering only the first-order statistical moment, conversely the state vector and covariance, where the strong Gaussian assumption is implicit; the modern literature is starting to analyse also the higher-order statistical moments, such as Gaussian mixtures or particle filters.

Observation strategies are instead concerning the scheduling problem.

The observation scheduling refers to the allocation problem of N_{tasks} possible observation tasks in $N_{windows}$ available observation windows, where usually $N_{tasks} > N_{windows}$.

Since the high difference between the number of possible observation tasks with respect to the number of available observation windows the number of possible permutations (ordered combinations) can be quite high. This usually requires an heuristic solution to the problem due to the computational unfeasibility of a complete analysis of all the solutions. The scheduling problem is usually associated with a cost function that helps to express in a deterministic way the benefit of performing a certain observation instead of another. So posed the problem, the observation scheduling is usually referred as an offline problem, where the available observation windows are allocated all in advance. The innovation introduced with this thesis will try to step over this limitations and consider different observation strategies which are operating in real-time.

1.4   Challenges of Space Surveillance and Tracking

The environment in some orbital regions reached already its maximum capacity in terms of number of objects. The saturation of some orbital regions and the every-day increasing probability of collisions is pushing the cataloguing operations to criticality. The incredibly high number of debris and objects that need to be monitored requires higher computational resources.

In order to make best use of these resources and to exploit at best the data extracted from observations, an optimal sensor scheduling capability is paramount. The ability to optimally control a network of sensors can give great advantages in terms of quality and quantity of the obtained data. Observing objects at the right moment and maximizing the coverage at same time is the main goal of the scheduling system for SST. As said, the final goal of SST is to delivery an up-to-date catalogue, comprehensive of most of the objects orbiting around Earth. Assuming to start a new SST system, the catalogue needs so to be first populated with object instances. In this case, CG processes will take place to observe uncatalogued objects and trigger the first correlation cataloguing activities. With the time, the objects now catalogued must be maintained (their information inside the catalogue must be updated). To absolve this task, CM strategies shall be adopted to keep track of the catalogued objects. However, new objects need to be observed as well. The main activity of a cataloguing system can be so recognized in cataloguing generation activities and in catalogue maintenance.

Modern SST systems, in fact, use to subdivides the sensor resources into two main groups: survey sensors and tracking sensors [15]. The survey sensors are used to absolve to CG tasks and tracking ones to CM. However, such a separation, much practical in terms of operations, it is not optimal for cataloguing since it is not making that best use of the available resources. A performant SST system shall be able to control all the sensors available by means of a centralized processing unit, which is always in communications with the sensors, receiving the imaging data and sending out commands. Of course, such a configuration, can result quite unpractical, especially when the number of sensors in the network is high and are very heterogeneous between each others (e.g. space-based telescope and ground-based radar arrays). What is already a practical trade-off is to create cooperation framework where more sensor operators and SST systems can share their data and measurements, it is an example of this the EU-SST program and *Small Aperture Robotic Telescope Network* (SMARTnet).

1.4.1   Catalogue Creation

The challenges connected with catalogue generation or creation are due to the a-priori unknowability of the objects that are going to be observed. Depending on some interests of the operators and characteristics of the sensors, an idea of the objects that can be accessible can be done. Once the orbital range of the accessible objects has been defined a scan of the sky must be performed. These kind of operations, that are usually referred to as survey campaigns. It is example of this the GEO fence studies, proposed during this work, to scan the GEO belt, or the LEO mapping strategies to map subsections of a LEO catalogue.

All of these observation strategies need to cope with a performant cataloguing systems that shall be able to process the observation data and perform correctly correlation and IOD. For such a reason, the strategies for CG shall be strictly related with the cataloguing processes to understand the best observation conditions and not only the highest coverage.

1.4.2 Catalogue Maintenance

The most important capability for an SST system is to maintain the current status of information inside a catalogue of objects and update them before their connected uncertainty becomes to high. The problem of catalogue maintenance is of the most studied by the SST literature and operators. It is has been extensively addressed in its convex version of a linearised model that optimes the information gain of each observation task. Depending on the degree of approximation, number of realistic constraints taken into account and dimension of both network and catalogue the problem can be solved via analytical or heuristic optimization approaches.

1.4.3 Special Event Scenarios

The cataloguing purposes are usually combined with events of interest that for different reasons may need to be observed. The classical example of that is the survey of close conjunctions between objects, that may evolve in a collision and, if catastrophic, a fragmentation event. These kind of situation require a different prioritization inside the operative scheduling systems. Most of the modern scheduling tools, i.e. [19], adapt the cost functions necessary for scheduling decision making to incorporate priorities due to not-strictly-cataloguing factors, like collision probability or manoeuvring probability.

During the work of this Thesis, the adoption of different prioritization strategies has been studied. In particular, it is relevant the example of collision survey, presented in sec. 4.2.2.4, that shows how the addition of LEO close conjunctions survey is not affecting a normal cataloguing plan too much and can be daily introduced inside a cataloguing scheduling system.

1.4.3.1 Fragmentation Scenario

Some specific events, anyway, are so relevant for the orbital space environment that require total attention of the scheduling systems and dedicated observation plans. This is the case of fragmentation events, which effects can be uncontrolled and unpredictable. The wrong and unmonitored evolution of fragments can escalate in further collisions with operative satellites and eventually a cascade disaster of catastrophic events, that is, the so-called Kessler syndrome. The first detection and subsequent follow-up of the fragments is the real challenge for SST. The fragments are initially close to each others for the first orbits, and then tends to disperse themselves as the different orbital perturbations acts on them (this is especially fast for LEO collisions). The unpredictability of the fragments positions, due to their first unknowability, results often in short arc observations [30], [44]. Different techniques have been exploited for this kind of scenarios, either involving up to date processing techniques to improve IOD [8][53] or involving more sensors like the

Along-track search strategy in [44].

A dedicated survey scenario, which makes use of the innovative *Virtual Debris* (VD) algorithm, is going to be presented in sec. 6.3.1.2.

1.4.3.2 Mega-Constellation

The rise of new mega-constellations (hundred of thousand of satellites) is going to force the evolution of the current SST systems and services. A forced path to this will go through a multinational cooperation between SST facilities, satellite owners and operators. As for satellite operators, their knowledge of precise orbit determination through GPS positioning, star trackers and finally telemetry data is a precious source of information for SST [5]. Companies that are aiming on launching thousands of satellites are OneWeb, Boeing, SpaceX and Samsung that are delivering their constellation in LEO for worldwide coverage of broadband communications. Other sources are aiming in delivering nano-satellites constellation, the Blackjack program by *US Defense Advanced Research Projects Agency* (DARPA), are instead for military applications. The saturation of some orbital regions is close to saturation and anti-collision manoeuvre are starting to be daily operations for such operators. More manoeuvres means also additional effort for SST and correlations. The hope for the future is so that the continuously increasing exploitation of orbital capacity will go hand in hand with a more evolute SST system, which needs to be managed in worldwide context and multinational sharing of data.

1.5 Use Cases

The main use cases that can be directly connected with the work of this Thesis are going to be presented in Chapter 6.

The use cases can be interpreted as direct consequences and results of the algorithm developed on this thesis for practical use. Additionally, a use case can be seen whatever additional result can be achieved with the same mind set utilized in the completion of the thesis. It is an example of this the *stare-and-chase* scenario, where a new algorithm will be presented for a possible future development of a complete real-time observation strategy.

Real-time observation strategies are becoming of great importance to cope with a continuously evolving space scenarios. Real-time activities are precious resources for surveys of high interest events, like collision and fragmentations.

In 6 the proposed use cases will refer to Fig.6.1 and they can be interpreted as validation examples of the new Thesis development proposed in chapters 3 and 4. In particular, the use cases will be so divided:

- *Space-Based study*: it consists on a detectability study in different scenarios. It will be explained how the new methods introduced in the thesis can support the feasibility studies of a space-based mission.

- *GEO-fence study*: in this section a study of the survey strategy for GEO fence will be presented. It will be explained how it is possible to obtain specific information for that specific orbital class.

- *Autonomous Cataloguing*: this section will show the direct applications of the new CG methods presented in the previous chapter 4, such as: the conjunction surveys and fragmentation detection.

- *Dynamic tracking*: presentation of the stare-and-chase scenario in close-loop control system.

The great number of objects in Space and the numerous presence of players involved in the SST scenario, each of them interested in protecting their own assets, requires also the necessity of sharing certain amount of data: from raw images or measurements to processed orbits and ephemerides. The quality of those data relies on their associated uncertainty, that becomes the key to understand how well the data can be trustable, how can be used at best and, most importantly, for how long can be used to predict future states before the information content expires.

This chapter will propose in the first section, sec. 2.1.1, a study performed during these years to assess the accuracy of the data provided by the most famous space object catalogue: space-track. Most of the simulations and real observation campaigns performed with ART have used these data to initialize a set of objects.

2.1 State of Art - What Data do we have now?

One of the main sources of data for SST is the online available space-track [3] catalogue. Most of the work of the Doctoral Thesis is based on the usage of the space-track catalogue. In particular, on the *Genetal Perturbations* (GP) data. GP data are provided by the US government, SSN, since the 1970s. They consist in mean classical orbital elements plus some information on body acceleration, shape and some other parameters more related with SGP4 propagators than with real physical meanings. However, for historical reasons, the usage of GP data became quite a common practice in the SST world for sharing data and orbital information. If, from one side, the most famous format for GP is the TLE or *Three Lines Element* (3LE), as of 2020 the *The Consultive Commitee for Space Data Systems* (CCSDS) recommends the new *Orbit Mean-Elements Message* (OMM) format that allows a wider cataloguing pool (i.e. it is based on a 9-digits numbering cataloguing systems instead of the 5-digits of TLE) [23]. What characterizes the space-track catalogue data is the absence of uncertainty information. Aim of the next section will be an attempt to assess the quality of that data.

Table 2.1: Examples for GEO case of errors obtained downloading the last 30 instances:

Statistical Variable	R	T	N	V_R	V_T	V_N
	km	km	km	km/s	km/s	km/s
Average	1.017528	16.70975	3.213651	0.001201	$6.93E-05$	0.000229
Standard error	0.031297	0.442073	0.156557	$3.26E-05$	$1.88E-06$	$1.14E-05$
Median	0.830331	15.68679	0.475227	0.001143	$5.73E-05$	$4.03E-05$
Mode	10	10	10	0.0001	0.0001	0.0001
Standard deviation	0.969709	13.69712	4.850728	0.001011	$5.82E-05$	0.000352
Sample variance	0.940336	187.6112	23.52957	$1.02E-06$	$3.38E-09$	$1.24E-07$
Kurtosis	106.5823	-1.11011	4.798069	-1.12738	68.05007	8.354632
Schiefe	7.84271	0.446104	2.063975	0.447647	5.666208	2.397164
Range of values	17.5759	51.55394	31.59631	0.003784	0.000972	0.002974
Minimum	0	0	0	0	0	0
Maximum	17.5759	51.55394	31.59631	0.003784	0.000972	0.002974
Sum	976.8269	16041.36	3085.105	1.152932	0.066486	0.219575
Number of samples	960	960	960	960	960	960

2.1.1 All studies on Space-Track data

As said, TLE data are available to the general public through the *Air Force Space Command* (ASSPC) by the web platform space-track.org. A TLE set for a certain object contains the value information of a specific set of mean orbital elements at a precise epoch, with no information about the accuracy. However, among various methods present in the literature to assess this lack, two main philosophies can be applied:

1. Precision of the data: Vallado in [48] evaluates the accuracy considering the number of digits in which the values are given inside the two line set. Concerning the epoch time value, only 8 decimal places are given, that corresponds to $\pm 5 \cdot 10^{-9}$ days, that are 0.0004 s. Moreover, the eccentricity is given with seven decimal places, this introduces an error of about 2 m for a GEO satellite ($r \approx a \cdot \Delta e$) in the radial direction; while the angles have only four digits, which led to errors around 6 m in LEO and 35 m in GEO.

2. Consistency with precise orbit propagators: more precise orbit propagators can be used to propagate and compare more instances of the same object defined via GP. As an example relevant for SPOOK, in [12], a consistency method [33] is used to extract the uncertainty related to TLE.

The latter is going to be briefly discussed in the next section.

2.1.1.1 Consistency Method

The following examples are split accordingly to three different orbital regions: GEO, MEO and LEO. The results presented in Tab. 2.1 show that for GEO objects, retrieved from space-track in TLE format, the consistency analysis suggests an average tangential uncertainty of 16.7 km, with a standard deviation of 13.7 km. However, looking also at the average error distribution presented in Fig. 2.1, a
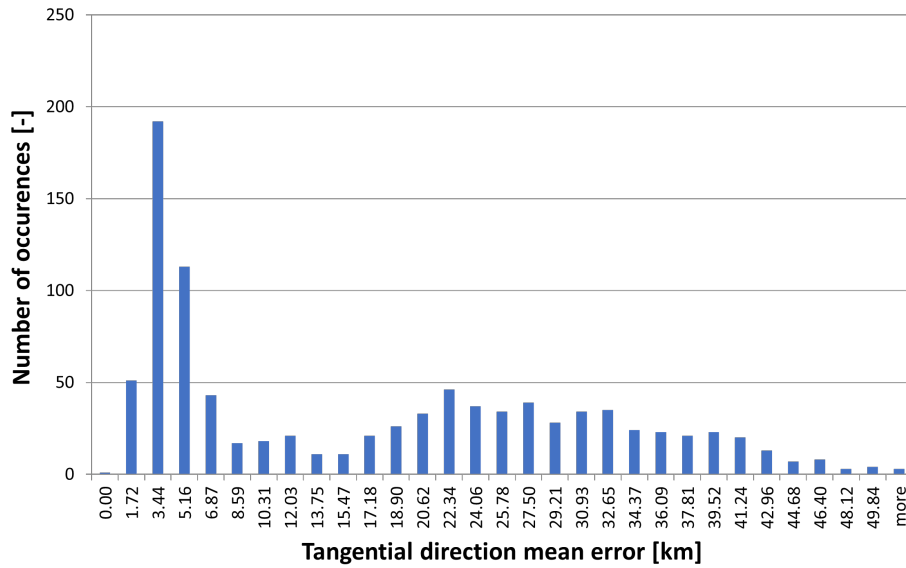
FIGURE 2.1: Distribution of the mean error in the tangential direction for GEO objects.

normal distribution is not the best fit to model a standard error for these kind of objects and a multi-modal analysis should be properly applied. As best practice for the usage of those values, it is so suggested to threat each object on its own. Depending on the number of instances, proportional to the number of times the object has been observed, each object may have a different consistency index, that can clarify how well its information can be trusted.

As matter of facts, the most common value in the distribution presented in Fig. 2.1, is the range between 1.7 and 3.4 km. A detail of the error distribution on the main three axes, of an object-fixed reference frame, has been reported also in Fig. 2.2. the distribution of the errors in the three main body-fixed axis are reported on the upper graph and the relative first derivative errors on the lower one. The distribution clearly shows the highly-crowded area of the GEO belt at the classical geostationary distance around 42 000 km where most of the active and controlled satellites are. Considering the results of the MEO population presented in Tab. 2.2 and Fig. 2.3, the consistency analysis suggests an average tangential uncertainty of 3.7 km, with a standard deviation of 3.6 km. The most common value is in the range between 0.7 and 2.7 km of tangential error. As for the LEO population, presented in Tab. 2.3 and Fig. 2.4, the consistency analysis suggests an average tangential uncertainty of 5.8 km, with a standard deviation of 10.2 km. The most common value is within the range below 3.8 km of tangential error. This short study presented for the GP, or TLE, data represents some of the possible way to assess the accuracy of that information. Despite this general lack of knowledge of an accurate value of uncertainty of these data, their usage is quite convenient for more reasons. First of all, they are publicly available and refer to the widest catalogue of objects. Most importantly, there are several analytical tools (e.g. the SGP4) that allow to process
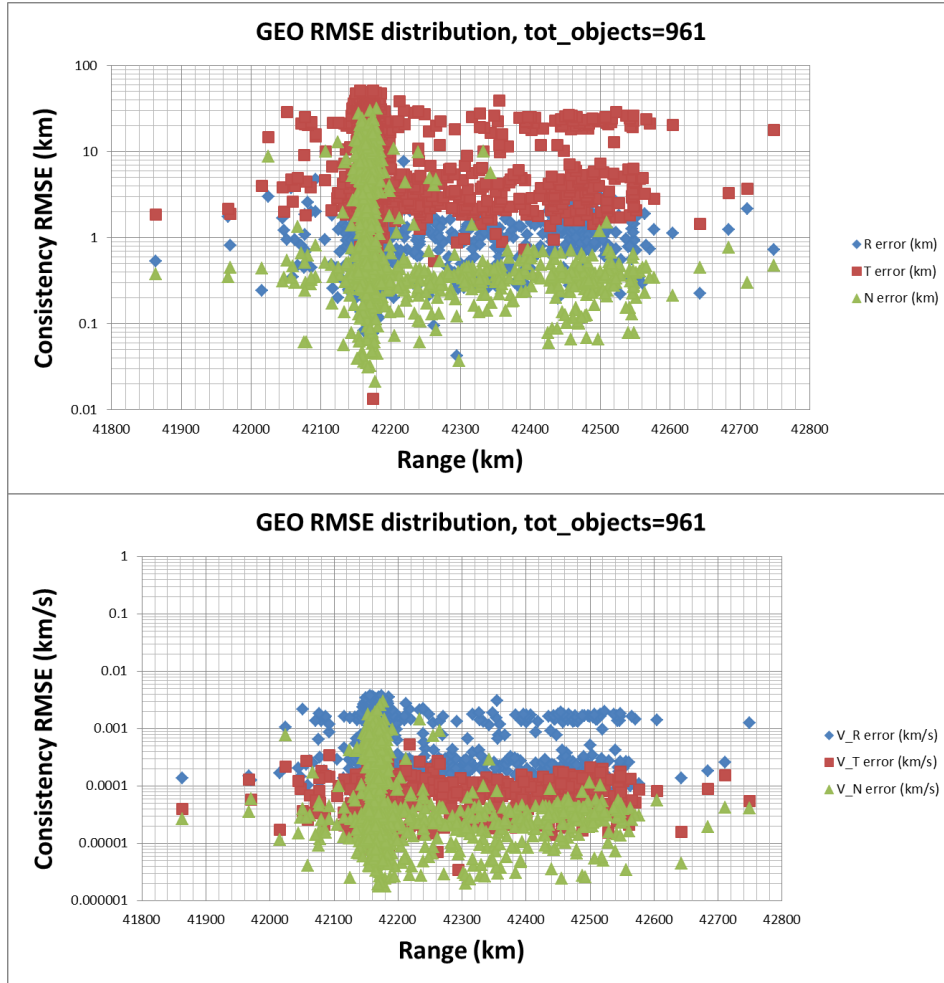
FIGURE 2.2: Distribution of the *Root Mean Square Error* (RMSE) for the GEO region objects.

Table 2.2: Examples for MEO case of errors obtained downloading the last 30 instances:

Statistical Variable	R	T	N	V_R	V_T	V_N
	km	km	km	km/s	km/s	km/s
Average	0.287797658	3.678259731	0.143550053	0.000524222	$4.24411E-05$	$2.82445E-05$
Standard error	0.016555282	0.230761831	0.006357004	$3.39473E-05$	$2.42989E-06$	$1.77467E-06$
Median	0.191571883	2.46416773	0.113575086	0.000350979	$2.81349E-05$	$2.29269E-05$
Standard deviation	0.259659446	3.619357889	0.099705718	0.000532443	$3.81113E-05$	$2.78345E-05$
Sample variance	0.067423028	13.09975153	0.00994123	$2.83495E-07$	$1.45247E-09$	$7.74761E-10$
Kurtosis	3.76917434	13.9323751	7.05361597	15.73730016	4.20173801	48.60661192
Schiefe	1.712003597	3.147805018	2.097021972	3.327020039	1.776024087	6.007856162
Range of values	1.546754513	29.46456003	0.718569716	0.004432193	0.000224154	0.00030322
Minimum	0.009106976	0.726267286	0.013934226	0.000128501	$1.89649E-06$	$5.32639E-06$
Maximum	1.555861489	30.19082732	0.732503941	0.004560694	0.00022605	0.000308546
Sum	70.79822393	904.8518939	35.31331304	0.128958589	0.010440522	0.006948148
Number of samples	246	246	246	246	246	246
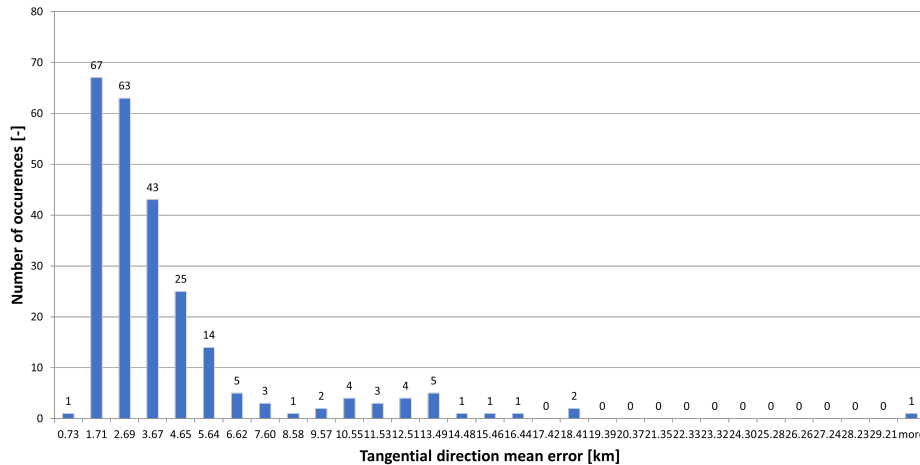
FIGURE 2.3: Distribution of the mean error in the tangential direction for MEO objects.

Table 2.3: Examples for LEO case of errors obtained downloading the last 30 instances:

Statistical Variable	R	T	N	V_R	V_T	V_N
	km	km	km	km/s	km/s	km/s
Average	0.191898839	5.874938368	0.173601052	0.006420381	0.000170158	$9.95465E-05$
Standard error	0.005384219	0.194602252	0.00343681	0.000216584	$3.28613E-06$	$1.84004E-06$
Median	0.162224267	0.869810526	0.113055376	0.000841914	0.000168231	$8.0445E-05$
Standard deviation	0.277326503	10.02343287	0.177020751	0.011155648	0.00016926	$9.47753E-05$
Sample variance	0.076909989	100.4692064	0.031336346	0.000124448	$2.86489E-08$	$8.98235E-09$
Kurtosis	266.8146594	3.17496793	5.331167877	3.251402275	799.4263966	43.18314074
Schiefe	13.29751492	2.050506746	2.121717928	2.066061657	21.15184158	4.80764752
Range of values	7.317395297	57.49516794	1.185739822	0.065495548	0.00662967	0.001372999
Minimum	0	0	0	0	0	0
Maximum	7.317395297	57.49516794	1.185739822	0.065495548	0.00662967	0.001372999
Sum	509.1076209	15586.21149	460.56359	17.03327037	0.451428048	0.264096764
Number of samples	2653	2653	2653	2653	2653	2653

those data with great precision and low computational effort, without the need of any further processing. To provide few practical examples, there are SST activities where this data can be used very efficiently:

- To create pointing profiles for a telescope;

- to generate statistic object population references;

2.2 Observation Strategies - an history

With observation strategies are meant all the algorithms and systems necessary to command a sensor or a network of sensors. The observations of the space objects are then used by post-processing systems to extract the information of the objects themselves.
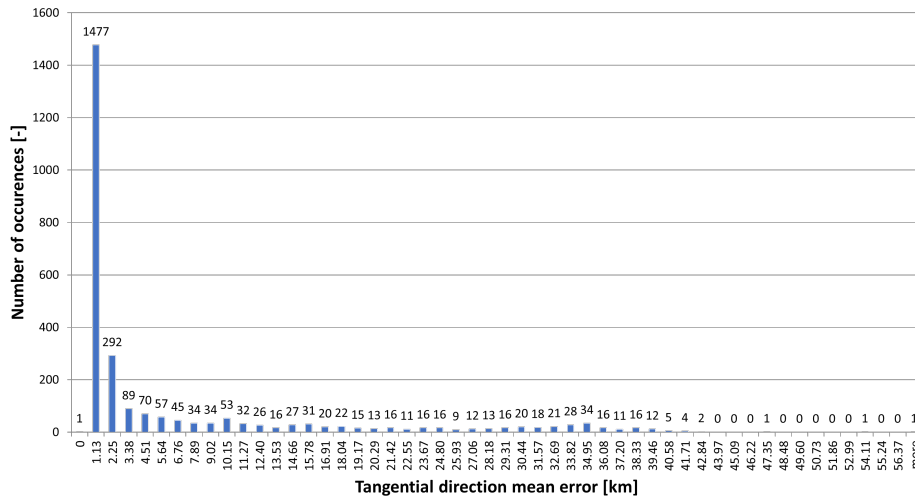
Figure 2.4: Distribution of the mean error in the tangential direction for LEO objects.

Sensor tasking is quite a complex problem nowadays to the multitude of objects in space that need to be constantly observed. Some key dates for space observations:

- 7 January 1610, Galileo Galilei uses his early version of the telescope to observe and track for the first time, three celestial bodies. He discovered the Jupiter's Moons: Io, Europa and Ganymede. In the following days, he will discover a fourth one: Callisto.

- 4 October 1957, The Sputnik rocket body has the first assigned NORAD number inside the NORAD classification.

- 11 January 2007, the Chinese *Anti-Satellite* (ASAT) mission destroys the Chinese weather satellite, the FY-1C polar orbit satellite of the Fengyun series, at an altitude of 865 km, with a kinetic kill vehicle travelling with a speed of 8 km/s in the opposite direction. The test produced at least 2087 pieces of debris large enough to be routinely tracked by the US Space Surveillance Network and the NASA Orbital Debris Program Office estimated it generated over 35000 pieces of debris down to 1 cm in size.

Except for the first example, conveniently chosen to show how tracking strategies of celestial bodies have always existed, it is impressive to note how in just 50 years, from 1957 to 2007, the space debris scenario is rapidly escalated.
From the first ever satellite launched on space, to the more recent mega-constellations, the environment around our planet changed considerably. What became more and more challenging, but never changed instead, is the necessity to track and catalogue all the satellites orbiting around our planet.
In the recent years new radar and optical systems have been built all around the Earth in order to absolve this challenging task. On spring 2021 [46] the Space Fence on Kwajalein Atoll reached operational capacity, increasing of more than 100
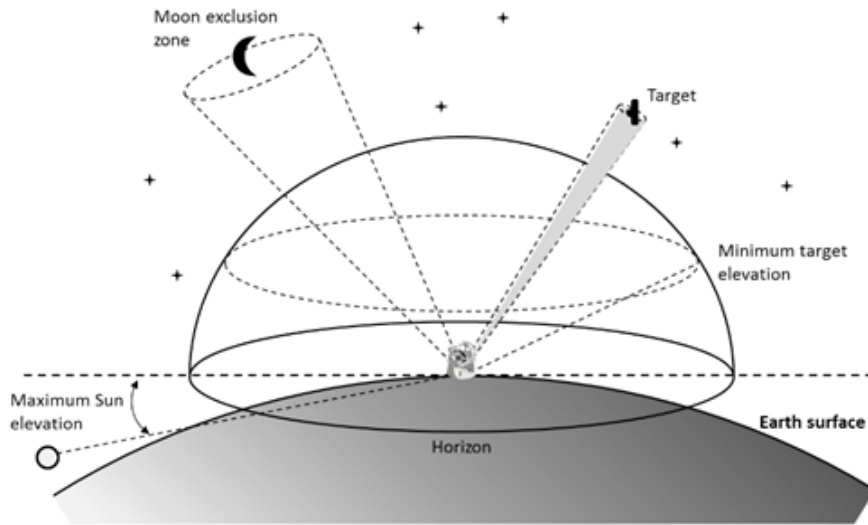
FIGURE 2.5: Visualization of the accessible sphere of a ground-based optical observer. Credits: [37].

thousand the number of the objects tracked by the *SSN* US network. New projects involving space radar and optical observers are foreseen to increase additionally the number of tracked objects.

Together with this exponential increment of observed objects the sensor tasking demand will become more and more challenging. The quantity of information a single entity or nation, is able to procure on its own is also becoming paramount for the intelligence of the single states. The last are starting in these years to give more and more attention to this topic. An example of this is the establishment of the European Space Debris centre for SSA, the EU SST.

Depending on the coordination with the various partner and data collection systems, the amount of tasks a single network of sensors should perform can change considerably.

2.3 Observation Geometry

The limits of space observations from ground observer can be explained in Fig. 2.5 in simplified way. The observation geometry, that means the environment around the observer, describes the range of allowed pointing directions accessible by the sensor itself. The accessibility sphere is the so called portion of the local celestial sphere where the telescope can steer and point. The observation direction of a ground-based sensor can be constrained by the location of the mount itself, the walls of the observatories or buildings in the proximity. This can constrain the minimum observable elevation of the objects crossing the sky over the observer. In the case of optical observation, also the position of the Sun becomes important. It is defined the astronomical Sun set, when the Sun is 9° below the local horizon. This corresponds to conditions of complete darkness. A necessary condition to reduce to the minimum

FIGURE 2.6: Observation geometry for a classical on-ground observer.

the noise in the observed images.

Looking at Fig. 2.6 it is possible to recognize some of the most used taxonomy in SST field. The observer O is placed on the Earth's surface. The elevation $\boldsymbol{El}$ of an observable target is identified from the $\boldsymbol{horizon}$, that is the tangential plane to the Earth's surface at the observer location. The declination $\boldsymbol{\delta}$ and right ascension $\boldsymbol{\alpha}$ are based instead on the local celestial reference frame, equal to the Earth centered reference frame but shifted to the latitude $\boldsymbol{\lambda}$ of the observer. In general, for optical observations, the important quantities that are considered for observed measurements are the coordinates of the observed objects:

- The right ascension α: the coordinate of the object measured in the local celestial equator.

- The declination δ: the coordinate of the object measured long the object local meridian.

These two coordinates, in the case of optical observations, corresponds also to the so-called observables of a telescope. A detailed and complete description of the reference systems that may be adopted for space object observations is proposed by the author in [35].

2.4 Benchmark

This section will present some of the SST operating systems to underline their characteristics and current limitations.

The most extensive SST network in the world is the US SSN [5]. It operates primarily with phased array radars and optical telescopes. SSN makes use additionally of mechanical tracking radars and the largest in the world space-fence located along the southern United States. It has also a optical space-based telescope constellations, the *Space-Based Space Surveillance* (SBSS) satellite and the Canadian Sapphire [52]. All data from the SSN are collected by the central command and control center, that is *Joint Space Operations Center* (JSpOC) located in California.

It is from there that the most extensive online available catalogue, space-track, is maintained by the 18th Space Control Squadron.

The second largest network of sensors is controlled by Russia instead. Russia maintains, in fact, a complete catalogue of space objects. The Russian *Space Surveillance System* (SSS) controls a network of phased array radars and optical telescopes. Similarly to SSN, the Russia SSA system consists of a centralized processing unit called *Automated Space Danger Warning System* (ASPOS), that has the aim of cataloguing space debris and support national security.

Other initiatives, that are mentionable, are the EU-SST and *International Scientific Optical Network* (ISON) partnerships, in Europe and Russia respectively.

The most extensive catalogues, are generically identifiable with a world wide distributed network of sensors (primarily phased array radars for LEO regions and optical telescopes for GEO tracking) and a centralized processing unit for the data collection and analysis.

2.4.1 Operative Systems

As said, the most extensive and documented operative system is provided by the US $18SPCS$. The SSN comprehends phased array radars, mechanical radars, optical sensors, and space-based telescopes. This complex system of sensors distributed all around the world allows to build-up and maintain a catalogue of approximately $24\,000$ objects. The daily operations of the network are scheduled both independently by some sensors and in a coordinated way between more sensors. However, the big amount of data and special events to be monitored requires a centralised and sensor-dislocated computation centers where the data are gathered and new commands are generated. In particular, events like fragmentations, collisions, and new launches are monitored with particular attention. For every new launch or a predicted catastrophic collision, models allow to generate raw virtual object elements (called ELSET) that allow the sensors to predict the future positions and point the telescope in that direction. In this easy scheduling approach, the object can either cross the sensor *Field Of View* (FOV) and contribute to upgrading the object information or be missed and not observed. Phased array instruments with large FOV and a relatively high range to cover most of the LEO regions are still a good approach for this kind of problem. Redundancy is often applied and multiple observations are generally performed. As a result, the scheduled tasks are generally overestimated and conflictual, and all possible network capabilities are not exploited.

Smaller-scale SST systems, like the private European national ones, are usually dependent on JSpOC data and update the orbital information of the assets that are of interest to the region. This is the example, previously cited of the Portuguese SST [15], which involves survey sensors for GEO scanning and tracking sensor for catalogue maintenance tasks.

With this Thesis, a small catalogue of mainly GEO objects has been deployed in Airbus servers to test and validate the observation strategies studied during this work. This Airbus catalogue will be presented in chapters 5 and 6. As visible from Fig. 6.18, as of November 2021 the catalogue was counting 519 correlated objects, mainly from geostationary (orbital period around 24 h).

In the near future, it is estimated that space objects (active satellites and debris) catalogues will contain the order of hundreds of thousands of tracked objects. Therefore, new challenges arise in the development of algorithms that will perform the maintenance of these catalogues. CM implies keeping the orbital information of the objects that are inside the catalogue within a certain level of reliability – i.e., limiting the associated uncertainty below a certain upper bound. To achieve that, objects need to be observed on a regular basis; however, currently, the number of objects to observe is considerably higher than the number of sensors available, which results in a task overload of the latter. Thus, an optimal sensor scheduling strategy shall be able to select the objects to observe in order to maximize the overall coverage and obtain as much relevant information as possible, avoiding task redundancies. Theoretically, this can be achieved by taking into account all the possible object-sensor combinations for the complete desired observation time window in order to allocate the best observation task to each object. Such a computationally expensive scheduling tool requires centralized systems to manage a diverse network of sensors that may not have enough resources locally for such computations (e.g. ground sensors in remote areas or eclipse/latency periods and data rate limits for space-based sensors). This work addresses the necessity of moving the scheduling ability from a centralized system to a local (on-board) processing framework within the sensor in order to enhance its autonomy. Within Airbus Defence and Space a tool has been created to reduce the computational load for observation scheduling and to provide support for a future real-time scheduler. In fact, the proposed baseline in sec. 3.2.3 does not try to allocate all the sensor tasks beforehand for the full observation period (e.g. one entire night). It evolves in a myopic state-space way, simulating just the imminent observing scenario, and together with the previously collected information performs an optimization of the next task to execute, eventually converging to an optimal coverage condition of the objects. The advantage of this approach is that it can be adopted for real-time decision-making strategies that, based on past and currently obtained measurements, may change the plan execution, compromising the

forecasted optimality of a plan obtained completely offline. The proposed baseline makes use of a modern CPHD filter for internal prediction and update of the first two statistical moments of a pool of objects represented by a Gaussian Mixture. The proposed work summarizes the implementation of the scheduler within the orbit propagation and determination tool SPOOK, which is developed at Airbus Defence and Space.

A comparison with state-of-the-art scheduling optimization algorithms, from simple greedy-methods to the heuristic genetic algorithms will be also presented.

3.1   State of the Art

Despite the literature for general Space Debris cataloguing problem is wide, it refers usually to the post-observations-to-catalogue steps. That means, the cataloguing processes like: image processing, measurement extraction, tracklet linking, correlation and orbit determination are well covered and developed with modern methods (i.e. machine learning and convolutional neural networks [14].

Few attention is anyway given to the last closing ring of the cataloguing chain: the observation scheduling. With observation scheduling are meant all the processes addressed to the management and tasking of a specific sensor or a network of sensors. As introduced before, the observation scheduling is becoming one of the most challenging task of operative SST systems. This is mostly due to the hard framework in which this systems are usually involved, that means, a number of objects that need to be observed is much higher than the number of allocatable resources to observe them. On top of this, there is also a quite practical constraint due to the lack of intercommunication between most of these systems and resources which end up usually performing redundant tasks and not performing at the best of their possibility.

On the other side, a big network of sensor is also difficult to be controlled and requires a lot of computational resources and fast transfers of data. The last issue becomes quite constraining when in the network of sensors are present also on-orbit platforms that with their lack of communications with ground define quite heavy constraints for a system centred processing system. Observation scheduling becomes so a hard trade-off between optimizing the performances of a network of sensors and the increased autonomy of single sensors that have constrained communication capabilities.

Catalogue maintenance observation strategies are connected with an updated catalogue of objects. Depending on the size of the catalogue and the number of sensors involved the strategies can be quite different and complex. Literature presents diverse strategies to perform CM for simply one-observer systems and small catalogues. This is the case of GEO catalogue maintenance strategies which makes use of either heuristic optimizations or greedy-methods [24]. The use of FISST-based methods to streamline cataloguing activities like tracklet-linking and OD is wide in the literature, and showed already a good range of applicability for maintenance of big catalogues [16] and [50]. Tangentially to this, sensor tasking algorithms evolved to assess better the characteristics of the sensors, their constraints and optics [18]. This allowed to asses better the observation and detection conditions of simulated scenarios to

find an accurate discriminant for pointing direction decision-making. This accurate detectability techniques, find a good application base again in multi-target filtering methods for cataloguing, for measurement estimation [19]. More rarely has been seen, instead, the integration of accurate models of the platforms of the telescopes to have a realistic estimate of slewing times. An example of this will be reported in section 3.2.2.2.

3.1.1 Orbit Determination

Scheduling the best observation is also matter of correct timing for tracking the object. Ideally, the best observation should be able to cover all the visible window of the object, since it rises from the horizon till the time it sets or enters inside the Earth shadow. The typical scenario of CM is however much more complicated, and not all the visibility window of an object can be allocated to a single task. For this reason it is important to choose the correct timing to perform the observation. In order to obtain the most of information after an observation there are usually some instances of the visibility passage that are more suitable for the observation, that means, the best of the information can be extracted. Different methods can be considered in this case to assess the quantity of information obtained after an observation, but more generally speaking, the best observation is the one that gives the best OD results.

Performing OD with the measurements obtained after an observation means to upgrade the information that is already available for an object and reduce its uncertainty. The typical objects in a CM system are defined with their state vectors, the $3D$ position and velocity of the object in space and their associated uncertainty. The uncertainty of a state vector $\boldsymbol{x}$ can be easily defined with the covariance matrix $\boldsymbol{K}$:

$$\boldsymbol{K}_{x_i,x_j} = cov\,[x_i,x_j] = E\left[(x_i - E[x_i])\,(x_j - E[x_j])\right] \tag{3.1}$$

where $E[x_i]$ is the expected or mean value. The gain of information, result of the OD, can be expressed as the difference between the covariance before and after the OD update.

Given the covariance before the OD update $\boldsymbol{K}_-$ and after $\boldsymbol{K}_+$, the information gain can be evaluated with different methods. One example is the *Shannon Information Content* (SIC):

$$SIC = \frac{1}{2}\ln\left(\boldsymbol{K}_-\boldsymbol{K}_+^{-1}\right) \tag{3.2}$$

An example of SIC trend for a satellite in orbit has been presented in [35]. This trend, visible for convenience in Fig.3.1, shows that there are optimal instant of time to perform an observation in the case the allowed time for the observation is constrained. The upper graph represents the hypothetical SIC obtainable for an object during its orbit around the Earth if observed at that specific time. As visible, the overall growing graph has the typical sinusoidal shape with period the orbit itself. It appears straightforward that some time instance are more optimal for an observation than others. The lower graph represents instead the along-track error of the object. The time corresponding to a local minimum of the along-track error and a local maximum of the SIC can be considered to be the optimal observation time for that object.
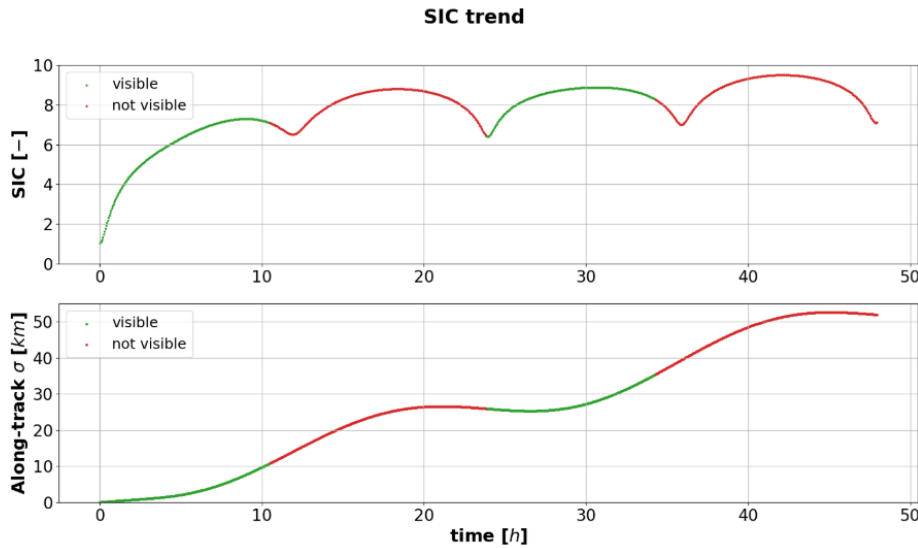
FIGURE 3.1: Evolution of the SIC for a GPS object in the time span of two days. Credits: [35].

3.2 Development of Autonomous Cataloguing Strategies

This chapter is going to explore the new development in the CM framework that has been realized in the scope of this Thesis. The typical scheduling techniques that have been investigated within this projects are of two main types: offline scheduling strategies and real-time (or dynamic) tasking. The first type of techniques is the most classical scheduling method analysed by the literature.

3.2.1 Heuristic Optimization

To the class of offline scheduling methods belongs the so-called heuristic optimization strategies. The optimization in this case is performed via heuristic methods such as genetic algorithm or *Particle Swarm Optimization* (PSO). The performance of these methods, in terms of quality of the collected information and coverage of the objects, is quite constrained by the success of the optimizer and the offline constraint itself. Addressing to the first issue involved in this generalization, the optimization method is based on a specific objective function that needs to be optimized. The solution space of this objective function is usually heavily irregular and not always convex.

3.2.1.1 Genetic Algorithm

the genetic algorithm presented in this framework analyses the usage of an encoding procedure specifically designed for the scheduling problem. This method has been presented for the first time by the author in [35]. The SPOOK implementation, specifically, makes use of a dedicated binary encoding logic where each individual, inside a population of possible scheduling solutions, correspond to a possible obser-
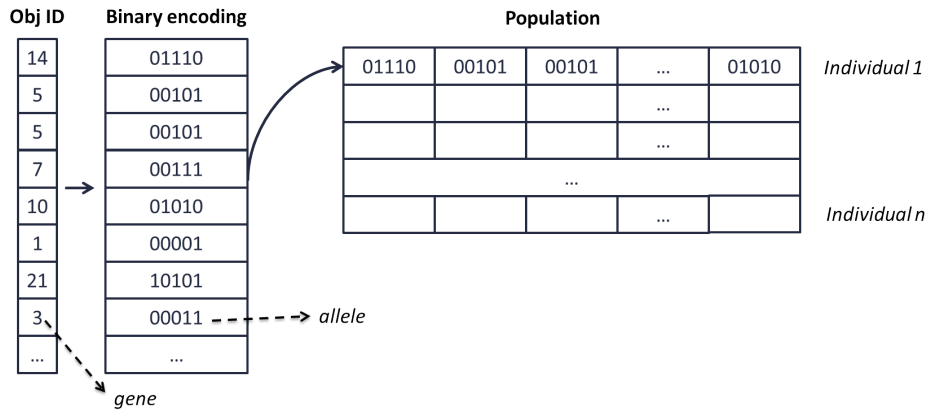
FIGURE 3.2: Encoding logic for the genetic algorithm as implemented in SPOOK.

vation plan made of pointing requests for each specific time step, see Fig. 3.2. A possible observation plan is called individual and is represented by a *chromosome.* The length of the *chromosome* corresponds to the number of time windows available in the plan. The scheduled object at each time step is called *gene.* The algorithm is encoding in binary formulation each gene to form an *allele.* As classical rules of for genetic algorithm both *allele* and *chromosome* are going through modification processes passing from a generation to another. A modification in the *chromosome* sequence is called crossover, while for the single allele is called mutation. At each generation, with a proper user-selected percentage (called elitism percentage), individuals close to the maximum fitness will remain unmodified. As shown in Fig. 3.2, the size of an individual corresponds to the number of observing tasks (the number of time steps during an observation night) and the number of genes is the total number of accessible objects.

The method evaluates the overall benefit of an observation plan (fitness of a population) with the following objective function:

$$fitness value = \sum_{i=1}^{n_w} SIC_i \qquad (3.3)$$

Where SIC has been defined in Eq. 3.2.

3.2.2 Local Optimization

Local optimization methods are a class of simplified offline scheduling problems that perform a local grid optimization to find the best observation plan.

3.2.2.1 Greedy Method

The greedy-method is a type of local optimization method for simplified scheduling problem. usually involving few observers and a small population of objects to be observed. The performance of this method are a good trade-off between low computational resources and objective function optimization. Such a method, in
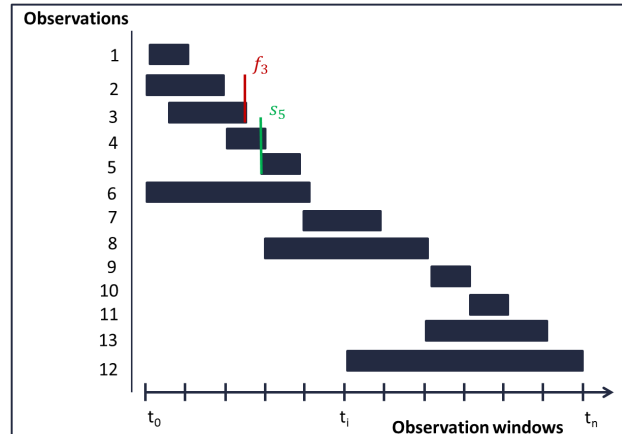
FIGURE 3.3: Visual representation of the sorting technique for the greedy-method.

fact, has been selected as main scheduling core for the single-observer system of the first Airbus Catalogue deployed within this Thesis. It has also been presented for the first time by the author in [35].

The greedy-method, as introduced by Tamassia in [20], is a sub-class of dynamic programming problems that aims to reduce considerably the computational time of the scheduling problem. The algorithm itself involves the partition of a big problem into smaller sub problems, reducing the computational time of a n-dimension problem into an $O(n)$ of time. The algorithm is composed into two steps: sorting the requests and the main optimization loop. In Fig. 3.3, it is represented a simplified visualization of the sorting algorithm. The observations tasks, the dark boxes, are sorted accordingly to the final observation time f_i of each task $i = 1, N_{tasks}$. The starting times s_i, may be in conflict with previous and next tasks. This conflict will introduce the prioritization of the algorithm when discriminating from performing one task or another. To start, the list of requests is initially sorted, involving recursive functions like in-place quick-partition algorithms [20, 35], accordingly to increasing final time f_i of the request. Then, inside the main loop, for each sorted requested is evaluated the observation predecessor. The predecessor of an observation task i is the closest previous observation e whose final time is before the start of the current task $f_e < s_i$.

For each sorted request is so evaluated the benefit of the observation, accordingly to the following rules:

- Maximum coverage: observe as many objects as possible.

- Follow-up service: maintain track of the objects with re-observations.

- Close passages: observe more objects inside the same FOV.

- Proximity with the previous observation: minimize the slewing time, or angular distance, with the previous observation.

Finally, the optimal observation is evaluated thanks to the greedy rule:

$$B(i) = max\left(B(i-1), b_i + B(P(i))\right) \tag{3.4}$$

Where $B(i)$ is the total benefit associated with the i-th scheduled observation, b_i is the benefit of the current observation requested analysed inside the loop and $P(i)$ is the index of the request predecessor. The intuitive greedy rule can be explained as follow: it is better to perform the previous observation request, or the current one and its predecessor? After this main loop is completed, the observation schedule is automatically generated.

3.2.2.2 Constrained Optimization

The real-world performance of a scheduling plan depends also on different observation constraints that need to be analysed in detail for the perfect implementation of an optimization algorithm. Despite the quite classical visibility and geometrical constraints an observation can occur, there is a set of quite important mechanical constraints that depends strongly on the type of platform that hosts the sensor. One of the main mechanical constraint depends on the dynamical model that steers the observer during the observation. Depending on how fast a sensor can update its pointing direction different observation possibilities can be taken into account starting from a certain pointing direction. If the re-pointing angle is too far to be reached in the necessary time, some observation possibilities need to be excluded. To absolve this task, for a standard off-the-shelves equatorial-mounted telescope ART, it is required a dedicated scheduler. This is the case for the Airbus cataloguer, where a dynamic model of the telescope platform has been integrated in SPOOK. A possible example of dynamical model for an equatorial-mounted telescope is described in Fig.s 3.4 and 3.5. Such a model takes into account the moving and settling time. Fig.s 3.4 and 3.5, refers to a local reference frame based on the local hour angle and declination coordinates. The mount of the telescope in those examples is German equatorial. In Fig. 3.4 it is considered the starting position of the telescope's mount to be always in parking position: 0° elevation and the local South meridian, the slewing time represented in this graph is the time in seconds necessary to move to the desired value of right ascension and elevation. Due to geometrical constraints of a realistic observatory room, only values of declination greater than 15° has been considered. The graph highlights also the change of pier-side of the mount. In Fig. 3.5 is showed the slewing time in seconds of the telescope that is necessary to move from a parking position to a higher value of elevation and for different ranges of hour angle. The considered parking position is the same as in fig. 3.4. As general reference for medium-sized telescopes ($\approx 40\,\mathrm{cm}$) in equatorial mount (classical type of mounting to achieve high tracking accuracy $< 2''$), this dynamic model has been also applied for generic simulations of similar sensors, during the work of this Thesis.

3.2.3 Real-time Approach: myopic approach with CPHD filter

The next class of problem is considering a real-time dynamic tasking. Real-time tasking aims to solve the problem of unpredictability of observation conditions and gives more robustness to a plan completely scheduled offline. Additionally, such a class methods offer the possibility of wider development to absolve different tasks - e.g. dealing with unpredicted passages objects, specific tracking request for targets of interests. In Fig. 3.6, it is schematized the basic approach behind a real-time
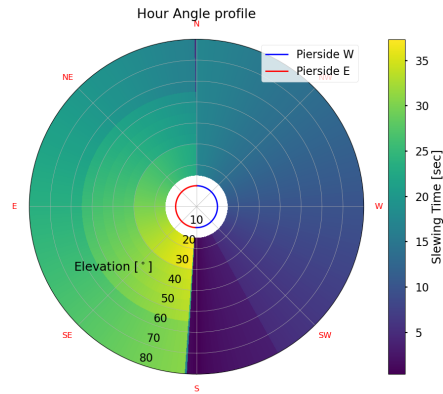
FIGURE 3.4: Example of an equatorial-mounted telescope dynamical model. The color expresses the magnitude of the slewing time needed to move from parking position to a certain local hour angle at fixed elevation.
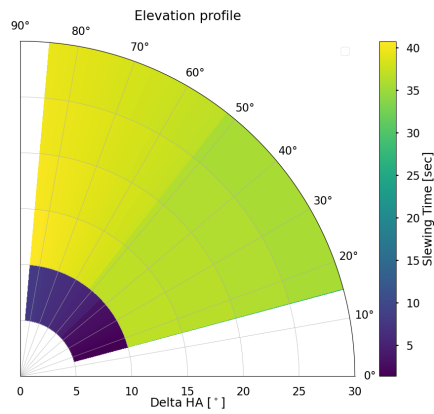
FIGURE 3.5: Slewing times in function of right ascension and elevation angles. The color expresses the magnitude of the slewing time needed to move from parking position to a certain elevation at fixed local hour angle.
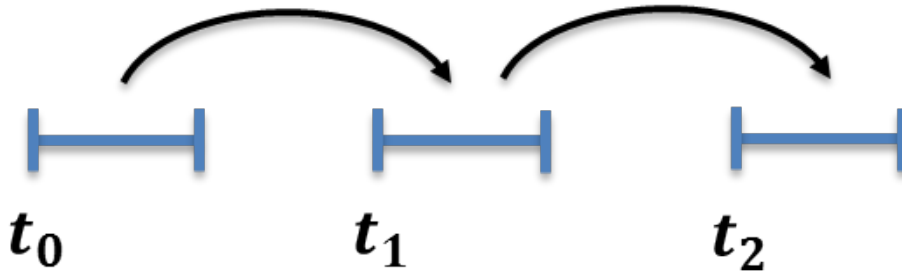
FIGURE 3.6: Sequential steps scheduling approach.

scheduling system. The idea behind a real-time scheduling is to create a myopic optimization problem that schedule just the imminent observation task, making use only of the information collected at the current and previous time steps. The method presented within this thesis aims to realize a baseline for future real-time methods. It is based on the realization of an optimization method for observation that schedules just the next observation task considering only the information obtained at the current and previous time steps.

3.3 Multi-sensors Multi-targets filtering

The content of the upcoming sections has previously been presented by the author in [37]. To maintain the continuity of this thesis, some definitions and mathematical analyses will be reiterated and further integrated. Multi-target tracking theories originally emerged to address air traffic management issues, primarily for radar systems. Over time, as discussed in [19] and [7], they have also been considered as potential avenues for the development of SSA.

A general definition of the problem is given by Ronald Mahler in [34] (Chapter 12), as follow:

1. Formulate the complete set of all observers and targets as single joint dynamically evolving stochastic system using point process theory (e.g. *Random Finite Sets* (RFS) theory).

2. Propagate the unknown *probability density function* (pdf) of the system using a recursive joint multi-sensors multi-targets Bayesian estimation.

3. Define and apply suitable reward functions that express global probabilistic goals for sensor tasking.

4. Use a valid optimization strategy to cope with the intrinsic unknowability of future observations.

5. Apply appropriate simplifications of this general (but usually intractable) formulation.

On the next sub-sections will be given a presentation of the problem for single state (or target) problem, and for analogy will be explained the definition of multi-targets

and multi-sensors spaces and how the CPHD finds a suitable trade-off between the analytical solution of the problem and its tractability.

3.3.1 Gaussian Mixtures

A common practice in space surveillance literature is to assume the results of IOD and OD methodologies as a Gaussian pdf [41]. This assumption allows to describe the full orbital uncertainty of the objects with the first two moments of a single Gaussian pdf: the mean and the covariance. In this framework, the linear Gaussian assumption is extended to the whole catalogue of objects. In the FISST framework, the first moment of the multi-target pdf is called intensity (or *Probability Hypotesis Density* (PHD)). It can be shown, that under the aforementioned Gaussian assumptions on the single target dynamics, also the posterior intensity will be a Gaussian mixture[49]. The linear Gaussian assumptions are so extended for the multi-target model.

An example of Gaussian mixture can be represented by the following equation:

$$\hat{f}_t(x|z_k) = \sum_{i=1}^{N} \omega_i \mathcal{N}(x_i, m_i, P_i) \tag{3.5}$$

where $\hat{f}_t$ indicates the pdf estimate at time t given the z_k measurement set, N is the number of objects (or kernels) in the mixture, and ω_i denotes the weight of the i-th object. $\mathcal{N}(x_i, m_i, P_i)$ expresses the normal distribution evaluated in x_i, conditioned by the mean m_i and covariance P_i.

3.3.2 Weights propagation

In the context of *Gaussian Mixtures Models* (GMM), two are the possible philosophies to be considered for weight propagation. One is to incorporate the propagation of the weights values together with object means and covariances propagation. Despite this method offers a good understanding of how weights and covariances are related, this procedure also leads to fast expiration of not-observed objects during the time, that is not a good behaviour inside a CM framework. The second method for weight propagation is to consider the weights as fixed properties of the objects, keeping their relative weight inside the mixture constant during only-propagation phases. The weights are so only governed by CPHD filter updates after each observation (or missed observation, e.g. detection probability very low) and by two other refinement procedure for GMM: splitting and merging of mixture components.

The propagation of the weights within the autonomous cataloguer has been realized as simplified in Fig. 3.7. As it is possible to note on that block diagram, and explained in Sec. 3.4.2.1, the weights are maintained constant during pure propagation phases, and updated only by splitting and merging routines to maintain valid the Gaussian assumptions and during the CPHD filtering. At the beginning of the scheduling scenario, supposed that the starting level of information is equal for all the objects, every object of the catalogue will initialize a single component inside the *Gaussian Mixtures* (GM). During the propagation of the GM, some of the components will experience high non-linearity index [41], that expresses how the uncertainty level
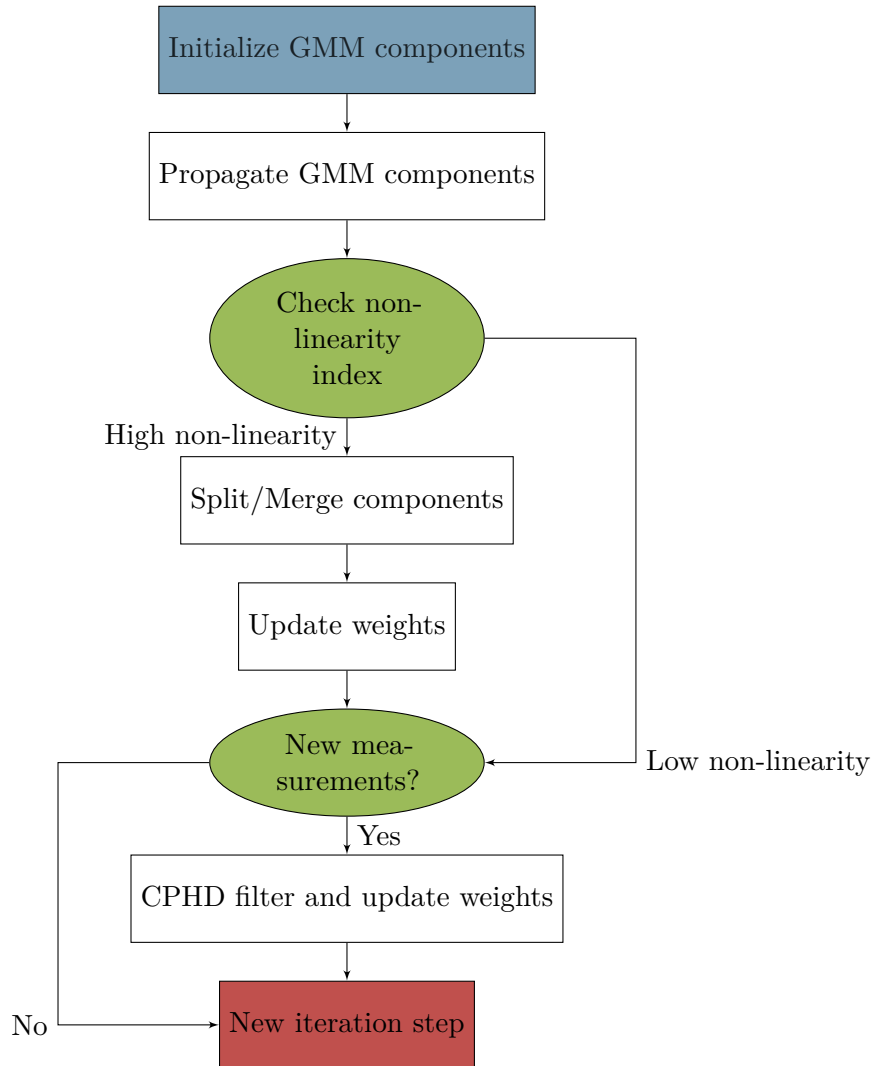
FIGURE 3.7: Weights propagation implementation inside the autonomous cataloguer.

of the object prediction is border-line with the Gaussian assumptions. That state is a clear signal that new measurements are needed, and its priority during the scheduling recursion will be increased. In case of no measurements are present, if the non-linearity index exceeds a certain level the object information is no more enough to express all the possible evolution of the objects and new components are needed. Those new components will be created thanks to splitting (and merging for the inverse process) techniques.

3.3.3 CPHD Filter

In the FISST framework for multi-targets filters one of the simplest estimator is the PHD filter, that predicts, updates and corrects the first moment of the multi-target pdf, known also as intensity function $\nu(\cdot)$ or PHD. The CPHD filter propagates and updates also the cardinality distribution together to the first moment estimate

[50]. The cardinality function is a discrete probability distribution on the number of components inside a mixture [19].

Inside this filter framework, for each component of the mixture is associated a weight ω, that corresponds to its "intensity" inside the mixture. When the uncertainties around the state are increasing, that is, the covariance is increasing, the relative weight of the component will be low, since the relative Gaussian uncertainty will be spread on more space. Vice-versa, when there is a good estimate of the state (for example after an observation), the weight of the component will be higher.

3.3.3.1 Problem formulation

A good introduction to the single-target filtering can be found in [49]. The first assumption that is going to be done for such formulation is to consider the space object dynamic as a partially observed Markov decision problem[1]. It is assumed, additionally, that both the predicted and updated state can be represented by *Independent Identically Distributed* (IID) clusters of RFS.

Further assumptions for the CPHD formulation will be presented later.

The proposed description of the method will follow the one presented in [49, 50, 19]. Space objects state propagation problems can be easily considered to follow a Markov process. Inside this process, the transition from state space at time $k-1$ to the current time step k can be seen thanks to a transition function:

$$f_{k|k-1}(x_k|x_{k-1}) \;\to\; prior\ density \tag{3.6}$$

that represents the orbital dynamic propagation. This prior density is partially observed in the observation space through the likelihood function:

$$g_k(z_k|x_k) \;\to\; likelihood\ function \tag{3.7}$$

that represents the function related to measurement generation given an orbital state.

Given the measurements set, it is possible to evaluate the probability of a state after an observation:

$$p_k(x_k|z_k) \;\to\; posterior\ density \tag{3.8}$$

that gives us the posterior density. The posterior density p_k can be computed using the Bayes recursion:

$$
\begin{aligned}
p_{k|k-1}(x_k|z_{1:k-1}) &= \\
&\int f_{k|k-1}(x_k|x)p_{k-1}(x|z_{1:k-1})dx \\
p_k(x_k|z_{1:k-1}) &= \\
&\frac{g_k(z_k|x_k)p_{k|k-1}(x_k|z_{1:k-1})}{\int g_k(z_k|x)p_{k|k-1}(x|z_{1:k-1})dx}
\end{aligned}
\tag{3.9}
$$

different numerical methods can be used to solve this recursion, as explained in [49].

---

[1]The current state of a target depends only on the state of the last time step.

This formulation can be easily extended to a multi-state scenario: let $M(k)$ be the number of components inside a mixture at time k and $N(k)$ the number of measurements at time k. In such framework are not considered any specific ordering rules for the states and measurements collections:

$$
\begin{aligned}
\boldsymbol{X}_k &= \{x_{k,1}, ..., x_{k,M(k)}\} \\
\boldsymbol{Z}_k &= \{z_{k,1}, ..., z_{k,N(k)}\}.
\end{aligned}
\tag{3.10}
$$

Analogously to single-state formulation, in multi-targets formulation the state of each target or component (x_k, y_k) can be modelled as random vectors, hence, also $\boldsymbol{X}_k$ and $\boldsymbol{Z}_k$ are RFS. An equal recursion formulation as above can be formulated. However, the recursion formulation in multi-targets space is computationally intractable, but adding the GMM approximation to the problem it is possible to yield a closed-form solution. This approximation assumes that targets evolve and generate measurements independently one from the other.

3.3.3.2 CPHD algorithm

The complete CPHD recursion derivation is out of the scope of this Thesis, and just the main results and routines utilized during this work, are going to be explained. In this framework two simplifications have been adopted to yield the tractability of this tool: the mixture is approximated to a GMM and the number of components, as this is the case, of objects that originates the mixture (the catalogue of space objects) is considered to be known a priory. The latter simplification, as will be showed during the report, allows to a special formulation of the filter that integrates the *Unscented Kalman Filter* (UKF) prediction and updates procedures.
The Algorithm of the implemented filter is partially presented in [50] and [19], with some extensions regarding the splitting and merging generations of new components during targets propagation phase to assess the non-linearity of Gaussian assumptions needed for precise processing of orbit propagation.
Suppose the posterior intensity, at time $k-1$, is a GM:

$$
\nu_{k-1}(x) = \sum_{i=1}^{J_{k-1}} \omega_{k-1}^i \mathcal{N}\left(x; m_{k-1}^i, P_{k-1}^i\right)
\tag{3.11}
$$

where ω_k^i is the relative weight inside the mixture of the i-component at time k, J_{k-1} is the estimated number of components of the GM at the previous time step $k-1$. As in eq. 3.5, $\mathcal{N}(x; m, P)$ indicates the pdf of an estimate x, given a Gaussian component with mean value m and covariance P.
The predicted intensity will be itself a GM:

$$
\nu_{k|k-1}(x) = \nu_{S,k|k-1}(x) + \gamma_k(x)
\tag{3.12}
$$

As well the cardinality will be given by:

$$
\begin{aligned}
& p_{k|k-1}(n) = \\
& \sum_{j=0}^{n} p_{\Gamma,k}(n-j) \sum_{l=j}^{\inf} C_j^l p_{k-1}(l) p_{S,k}^j (1-p_{S,k})^{l-j}
\end{aligned}
\tag{3.13}
$$

where $\nu_{S,k}(\cdot)$ is the intensity of the survived targets at time k and $\gamma_k(\cdot)$ the intensity of the new target births at time k. The survival intensity, corresponds to the intensity of the propagated targets present in the mixture at the previous time step:

$$
\begin{aligned}
&\nu_{S,k|k-1}(x) \\
&= p_{S,k} \sum_{j=1}^{J_{k-1}} \omega_{k-1}^j \mathcal{N}\left(x; m_{S,k|k-1}^j, P_{S,k|k-1}^j\right) \\
&m_{S,k|k-1}^j = F_{k-1} m_{k-1}^j \\
&P_{S,k|k-1}^j = Q_{k-1} + F_{k-1} P_{k-1}^j F_{k-1}^t
\end{aligned}
\tag{3.14}
$$

where F_{k-1} is the *state transition matrix* (stm) of time step $k-1$ and Q_{k-1} the process noise. As will be presented later, in the actual implementation of the filter the orbital dynamic is represented by a proper transition function for the propagation and any stm is really utilized. For the covariance, as well, the Unscented Transformation theory is exploited and the covariance is propagated through the propagation of the so-called sigma-cloud [51].

Supposed the predicted intensity $\nu_{k|k-1}$ is a Gaussian distribution, the CPHD update simply to:

$$
p_k(n) = \frac{\Psi_k^0\left[\omega_{k|k-1}, Z_k\right](n) p_{k|k-1}(n)}{\left\langle \Psi_k^0\left[\omega_{k|k-1}, Z_k\right], p_{k|k-1}\right\rangle}
\tag{3.15}
$$

$$
\begin{aligned}
&\nu_k(x) = \\
&\frac{\left\langle \Psi_k^1\left[\omega_{k|k-1}, Z_k\right], p_{k|k-1}\right\rangle}{\left\langle \Psi_k^0\left[\omega_{k|k-1}, Z_k\right], p_{k|k-1}\right\rangle}\left(1 - p_{D,k}\right)\nu_{k|k-1}(x) \\
&+ \sum_{z \in Z_k}\sum_{j=1}^{J_{k-1} J_{k|k-1}} \omega_k^j \mathcal{N}\left(x; m_k^j(z), P_k^j\right)
\end{aligned}
\tag{3.16}
$$

Where the auxiliary vectorial functions Ψ_k^1 and Ψ_k^0 are widely explained in [50], and $\langle \cdot, \cdot \rangle$ is the internal product operator.

However, some further simplifications are possible if the number of objects is supposed to be known a priori during the propagation.

In this particular case, in fact, the cardinality distribution at any time will be equal to a Dirac delta centered on the current number of objects $\delta_N(\cdot)$ with $N \in \mathbb{N}$. In this special case, a closed form solution for the filter update is possible [50], and with the form:

$$
\begin{aligned}
&\nu_k(x) = \\
&\frac{\Psi_k^1\left[\omega_{k|k-1}, Z_k\right](N)}{\Psi_k^0\left[\omega_{k|k-1}, Z_k\right](N)}\left(1 - p_{D,k}\right)\nu_{k|k-1}(x) + \\
&\sum_{z \in Z_k}\sum_{j=1}^{J_{k-1} J_{k|k-1}} \omega_k^j \mathcal{N}\left(x; m_k^j(z), P_k^j\right)
\end{aligned}
\tag{3.17}
$$

Where:

$$\omega_k^{(j)} =$$

$$p_{D,k}\omega_{k|k-1}^{(j)}q_k^{(j)}(z)\frac{\Psi_k^1\left[\omega_{k|k-1}, Z_k \setminus z\right](N)}{\Psi_k^0\left[\omega_{k|k-1}, Z_k\right](N)}\frac{\langle 1, K_k\rangle}{K_k(z)} \tag{3.18}$$

Where $q_k^{(j)}(z)$ is the likelihood function of the measurement set z and $K_k(z)$ are the number of clutters (noise level) of the current measurement set.

In the current work, the GM CPHD recursion is based on Unscented Transformation. The idea is to propagate through Unscented Transformation the first and second moments of each GM through the non-linear transformation as follows[51]:

1. each j component of the GM, defined by a mean $\mu_k^{(j)}$ and a covariance $C_k^{(j)}$, generates a set of L sigma points x and weights u.

2. each sigma point is then propagated to next time step according to the transition function $x_{k|k-1}^{(l)} = \phi_k\left(x_{k-1}^{(l)}, \nu_{k-1}^{(l)}\right)$ for $l = 0 \to L$, and with $\nu_{k-1}^{(l)}$ process noise.

3. the prediction step is so computed:

$$m_{k|k-1}^{(j)} = \sum_{l=0}^{L} u^l x_{k|k-1}^{(l)}$$

$$P_{k|k-1}^{(j)} = \tag{3.19}$$

$$\sum_{l=0}^{L} u^l \left(x_{k|k-1}^{(l)} - m_{k|k-1}^{(j)}\right)\left(x_{k|k-1}^{(l)} - m_{k|k-1}^{(j)}\right)^T$$

4. for the update, the sigma points are propagated through the likelihood function into measurements $z = h_k\left(x_{k-1}^{(l)}, \epsilon_{k-1}^{(l)}\right)$, with $\epsilon_{k-1}^{(l)}$ sensor noise, for $l = 0 \to L$.

5. the update step can be so computed:

$$\eta_{k|k-1}^{(i)} = \sum_{l=0}^{L} u^l z_{k|k-1}^{(l)}$$

$$P_k^{(i)} = P_{k|k-1}^{(i)} - G_k^{(i)}\left[S_k^{(i)}\right]^{-1}\left[G_k^{(i)}\right]^T$$

$$K_k^{(i)} = G_k^{(i)}\left[S_k^{(i)}\right]^{-1} \tag{3.20}$$

$$G_k^{(i)} =$$

$$\sum_{l=0}^{L} u^l \left(x_{k|k-1}^{(l)} - m_{k|k-1}^{(j)}\right)\left(z_{k|k-1}^{(l)} - m_{k|k-1}^{(j)}\right)^T$$

Where the $S_k^{(i)}$ formulation will be presented in Eq. 3.23, and corresponds to the uncertainty related with the measurement set Z_k with mean $\eta_{k|k-1}^{(i)}$.

3.4 Algorithm implementation

This section is going to present the integration of the scheduler inside the SPOOK software tool as will be presented in chapter 5. This section will present the main building blocks of the scheduler referring to fig. 3.8.

3.4.1 Architecture of the scheduler

The baseline architecture for the automatic scheduler consists in all the loop necessary to: define a pool of objects from a catalogue, initialize a GM with the properties of the catalogues objects, propagate the objects from one time step to the next one, move the FOV, simulate/estimate measurements, perform OD on data, evaluate the reward function and choose the best pointing.

As visible from Fig. 3.8, the GM is defined at the beginning of the main integration loop with the a priori knowledge that we have of the objects inside the catalogue. Each integration step is made of the following phases: propagate all the objects to the next time step and evaluate the accessibility[2], select all the possible observation possibilities and evaluate for all of them the reward function associated with the observation. The observation possibility with the highest associated reward function value will be selected as next pointing for the FOV.

When a pointing position is selected, the observed objects information inside the catalogue is updated accordingly to the previously presented UKF-CPHD filter.

3.4.2 Mixture propagation

The propagation of the mixture applies the UT theories, where the covariances (or uncertainties) of the objects inside the GM are updated propagating a user defined cloud of sigma points.

The propagation of the mixture relies on the already-present Airbus software called *Special Perturbations Orbit Propagator* (SPOP) [13]. The options for propagation can be selected by the user to different levels of accuracy. Inside the results sections, the selected options are going to be thoroughly defined.

3.4.2.1 Splitting and Merging routines

As introduced above, inside the GMM framework different theories for weights and components propagations can be adopted, that could be incorporated into two categories. The first idea is to not change the value of component weights during the simple propagation but only follow the splitting and merging rule when the covariance related with the states reach certain characteristics, the second idea, instead, is to have a direct influence of the uncertainty level on the weights propagation. The first method allows to safe the Gaussian hypothesis, and for this reason is to be considered the most suitable when dealing with GM. In fact, the first method allows to never exceed certain value on the uncertainty or covariance by means of the so-called non-linearity index. On the other side, this method can lead to a huge

---

[2]With accessibility is meant the crossing of the object with the observable celestial sphere of the sensor, see fig. 2.5.
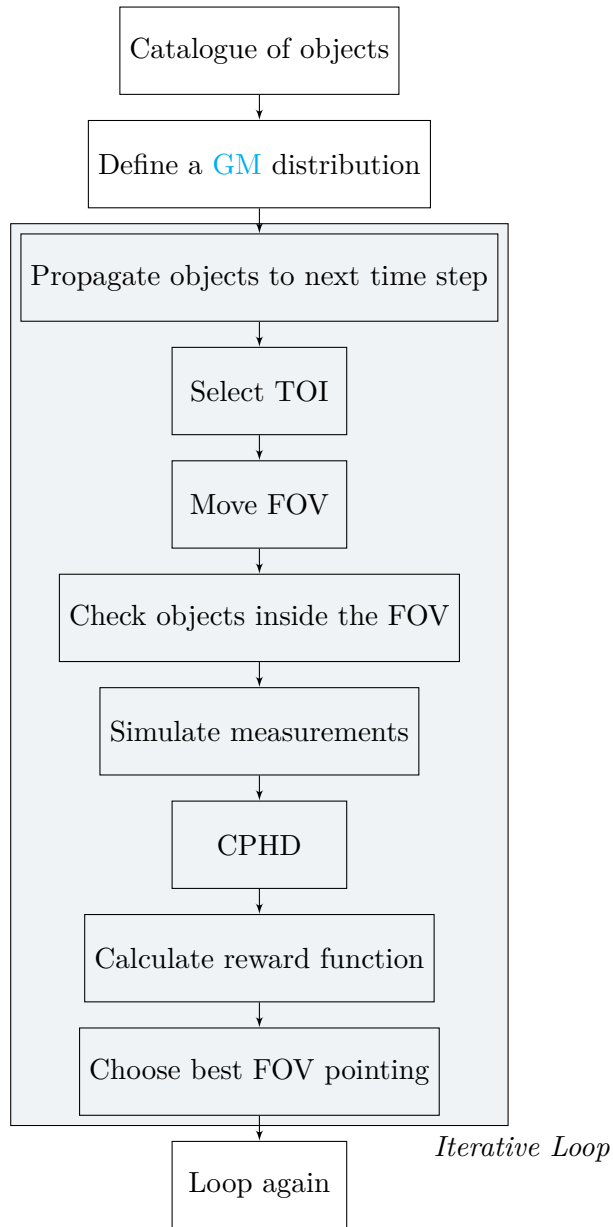
FIGURE 3.8: Baseline implementation of the automatic scheduler inside SPOOK.
Credits: [37]

number of components very easily and in order to maintain a proper computational tractability, a proper components pruning routines should be applied. The second method is, the other side, very suitable for big dimension problems as SST, since is not affecting in a valuable way the number of components inside a mixture.

The approach used in this work is a combination of the previous two: for each component at each time step the non-linearity index is evaluated and used as input for the splitting and merging routines. Every time a splitting routine is triggered, the component is *virtually* split, that means, the mean value of the component state remains the same while its weight inside the mixture is reduced accordingly to the number of splitting kernels that have been evaluated. This procedure is adopted for this special case of observation scheduling, since the mean values of the object state has no sense to be modified being, in fact, a simulation and no real observations/measurements are really performed.

3.4.3 Measurements generation

The measurements generation routine works into two levels: estimated measurements and simulated measurements. Besides the differences in the evaluation, the first are used as reference for the CPHD filter update and are evaluated for each objects for all the sigma points and the second are the results of the scheduler simulation, containing all the noise and false detection according to the simulation options.

3.4.3.1 Predicted Ideal Measurement Set: PIMS

In the framework of measurements simulation, a great problem is how to evaluate all the possible observation combinations given a set of catalogued objects and a network of observers. The idea at the basis of this work is to generate at each time step a *Predicted Ideal Measurement Set* (PIMS) taking into account the position information of the objects and their weights.

The PIMS is generated starting from the real position of the objects inside the GM and no false detections or clutters, are considered at this step, see [34] chapter 12, pag. 269.

An additional filtering has been performed on the possible combinations of observations, to obtain a feasible computational time and tractability. In fact, if considering two observers and being m and n the numbers of visible objects for the first and second sensors respectively, the total number of possible combinations is $n \cdot m$. Considering cases of ≈ 400 objects visible for each observer, the number of possible observation combinations for a big network of observers can be huge. To overcome this issue a maximum number of possible combinations per each time step has been selected, accordingly to the lowest weights inside the mixture.

3.4.4 Detection prediction

The detection probability is to be evaluated as the potential position of an object to the FOV. In Fig. 3.9 it is show the meaning of the intersection between an observer FOV and the object pdf. In Fig. 3.9, on the left the mean object position fell inside the rectangular FOV a standard detection algorithm will consider the object as observable. Opposite is the case on the right, where the mean of the normal pdf is
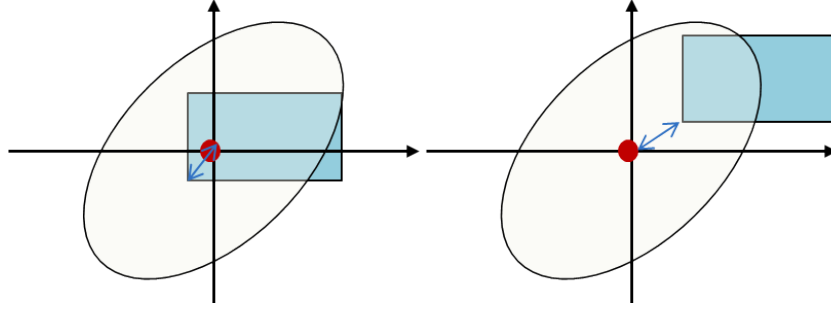
FIGURE 3.9: Intersection examples of a possible sensor's rectangular FOV and normal uncertainty ellipsoid corresponding to the object position.

outside the rectangular FOV.

The probability of detection can be seen as product of two terms:

$$P_D = P_{D,sensor} \cdot P_{D,FOV} \tag{3.21}$$

The first term is a state-independent quantity, that represents the properties of the observer (and the images processing pipeline that is connected). This term takes into account all the instrumental errors connected with sensor performances. The exploitation of all these characteristics is out of the scope of this report. On the other hand, the second term is a state-dependent quantity, that accounts for the relative position of the mean state of the object, the FOV and its covariance.

A component of the GM is considered to be perfectly observable (ideally $P_{D,FOV} = 1$) when its estimate measurement is completely inside the FOV and the uncertainty "cloud" around that measurement is completely contained inside the FOV too.

An object is considered to be partially observable when the cumulative probability density of its pdf (integrated inside the FOV) is constrained by the following values:

$$0.05 \leq \int_{FOV} p_g\left(z; z_k^j, P_{zz}^j\right) dz \leq 0.95 \tag{3.22}$$

A good measure of the uncertainty ($\boldsymbol{S}_k^i$) around the mean measurement can be easily given thanks to the Unscented Transformation theory:

$$\boldsymbol{S}_k^i = \sum_{l=0}^{L} u^l \left(z_{k|k-1}^l - \eta_{k|k-1}^i\right)\left(z_{k|k-1}^l - \eta_{k|k-1}^i\right)^T \tag{3.23}$$

where the k index indicates the time step, the indices from l to L corresponds to the components of the sigma cloud[3], η is the mean estimated measurement generated with the mean position of the object and z are the estimated measurements for all the sigma points.

An expression for the detection probability calculation is given assuming a bi-variate normal distribution of the uncertainty in the FOV space, and it is presented in appendix 3.5.

---

[3]In this case the sigma cloud refers to the set of sigma components created accordingly to the Unscented Transformation theory.

3.4.5 Reward function

The proposed reward function in this work is though to be completely based on the weights information of the GM. Suitable for this case is the Renyi function, that express the gain in information after a possible measurements evaluating the improvements of the gain values after the filter update. A wide dissertation on the Renyi reward function can be found in [40].

The general formulation of the information gain is:

$$R(\boldsymbol{u}) = \frac{1}{\alpha - 1} \log \int f_1(X; \boldsymbol{u})^\alpha f_0(X)^{1-\alpha} dX \qquad (3.24)$$

where $\boldsymbol{u}$ is the FOV control vector and $f_0(\cdot)$ and $f_1(\cdot)$ are the prior and posterior pdfs of the GM.

This formulation could be quite simplified, with the assumptions described in the previous sections, and related completely to the weights information [40]:

$$\begin{aligned} R(\boldsymbol{u}) \approx \\ \sum_{i=1}^{N} w_{k|k-1}^i + \frac{\alpha}{1-\alpha} \sum_{i=1}^{N} w_k^i - \\ \frac{1}{1-\alpha} \sum_{i=1}^{N} \left(w_{k|k}^i \right)^\alpha \left(w_{k|k-1}^i \right)^{1-\alpha} \end{aligned} \qquad (3.25)$$

In both Eq.s 3.24 3.25, the parameter α is to be selected by the user to optimize the performances. According to the literature, and in this work, the value selected is 0.5.

3.5 Bi-variate normal distribution

The bi-variate normal or Gaussian distribution is a generalization of the one-dimensional probability density function to two dimensions fields [27]. In this case the formula for the pdf evaluation is the following:

$$\begin{aligned} f(\alpha, \delta) = \\ \frac{1}{2\pi\sigma_\alpha\sigma_\delta\sqrt{1-p^2}} \exp^{-\Theta} \\ \Theta = \frac{1}{1-p^2} \left[\frac{(\alpha-\mu_\alpha)^2}{\sigma_\alpha^2} + \frac{(\delta-\mu_\delta)^2}{\sigma_\delta^2} - \frac{2p(\alpha-\mu_\alpha)(\delta-\mu_\delta)}{\sigma_\alpha\sigma_\delta} \right] \end{aligned} \qquad (3.26)$$

Where α and δ are the coordinates, σ_α and σ_δ the relatives uncertainties and p is the correlation parameter. As the coordinates indicates the dimension of the observables is due to the observation measurements type.

In fact, considering for simplicity an optical observer the usual reference system for measurements are expressed by means of two angles, that for consistency with standards are right ascension and declination angles. To find the cumulative probability, that is, the integral of the bi-variate pdf inside the FOV of the sensor:

$$\int\int_{FOV} f(\alpha, \delta) dFOV = \int_\alpha \int_\delta f(\alpha, \delta) d\alpha d\delta \qquad (3.27)$$

an integration step is required.

Different formulas can be found in literature for bi-variate cumulative probability, see [27]. In this framework three different strategies for probability integration have been implemented. A first strategy consider the equations for bi-variate normal cumulative density presented in the aforementioned paper, the second is an approach consisting in the evaluation of the Mahalanobis distance between the target and the edges of the FOV and from that evaluating the probability of falling inside the FOV thanks to the formula:

$$p_D = 1 - \exp^{\frac{-r^2}{2}} \tag{3.28}$$

Despite this method is not very precise is very fast in computation.

The third method consists in the full integration of the bi-variate normal density presented in Eq. 3.26. The integration has been realized first integrating analytically the expression on the right ascension dimension:

$$
\begin{aligned}
I = \\
G \int_{\delta} \exp^{C(\delta - \mu_\delta)^2} \left[erf(F(D(\delta - \mu_\delta) + Eb)) \right. \\
\left. - erf(F(D(\delta - \mu_\delta) + Ea)) \right] d\delta
\end{aligned}
\tag{3.29}
$$

with:

$$
\begin{aligned}
A &= \frac{1}{2\pi\sigma_\alpha\sigma_\delta\sqrt{1-p^2}} \\
B &= \frac{1}{2(1-p^2)} \\
C &= -\frac{B}{\sigma_\delta^2}(1+p^2) \\
D &= p\sigma_\alpha \\
E|_b^a &= \sigma_\delta(\eta(1) - \alpha)|_b^a \\
F &= \frac{\sqrt{B}}{\sigma_\alpha\sigma_\delta} \\
G &= \frac{\sqrt{\pi}\sigma_\alpha A}{2\sqrt{B}}
\end{aligned}
\tag{3.30}
$$

and then integrating numerically, via Simpson's method, long the declination dimension according to Eq. 3.30.

3.5.1 Possible Extensions

The strength of this method for observation planning relies in its high versatility. As shown in Fig. 3.10, the inner algorithm of the scheduler allows a set (the blue box on the bottom right) of possible extensions. Depending on the degree of realism the scheduler should acquire to simulate at best the real observation scenario the following source of noise on the measurements can be considered:

- the optical performance model;

- the astrometric performance in the image processing routines;

- the detection probability due to camera and image processing processes;

- possible data association uncertainty due to the correlation models.

Inside the planning routine, can be additionally considered the definition of *Targets of Interest* (ToI). It has been shown that the scheduling tool can be biased to specific targets simply increasing the relative value of the weights in the mixture [19]. Priority of some targets can be increased for scientific reasons or military intelligence. Automatically the algorithm will recognize the objects with increased weight for observation and allocate more observation tasks to them.
Additionally, thanks to the scheduler formulation, different observation scenarios can be considered. This is the case highlighted in Fig. 3.10 next to *Success of observation*. In the graph are visible the possible extensions to highlight the versatility of the real-time algorithm. Communication channel drop-out, obscuration period, can be simulated as well for space-based observers in order to consider possible lack of measurements from one of the sensor in the network.
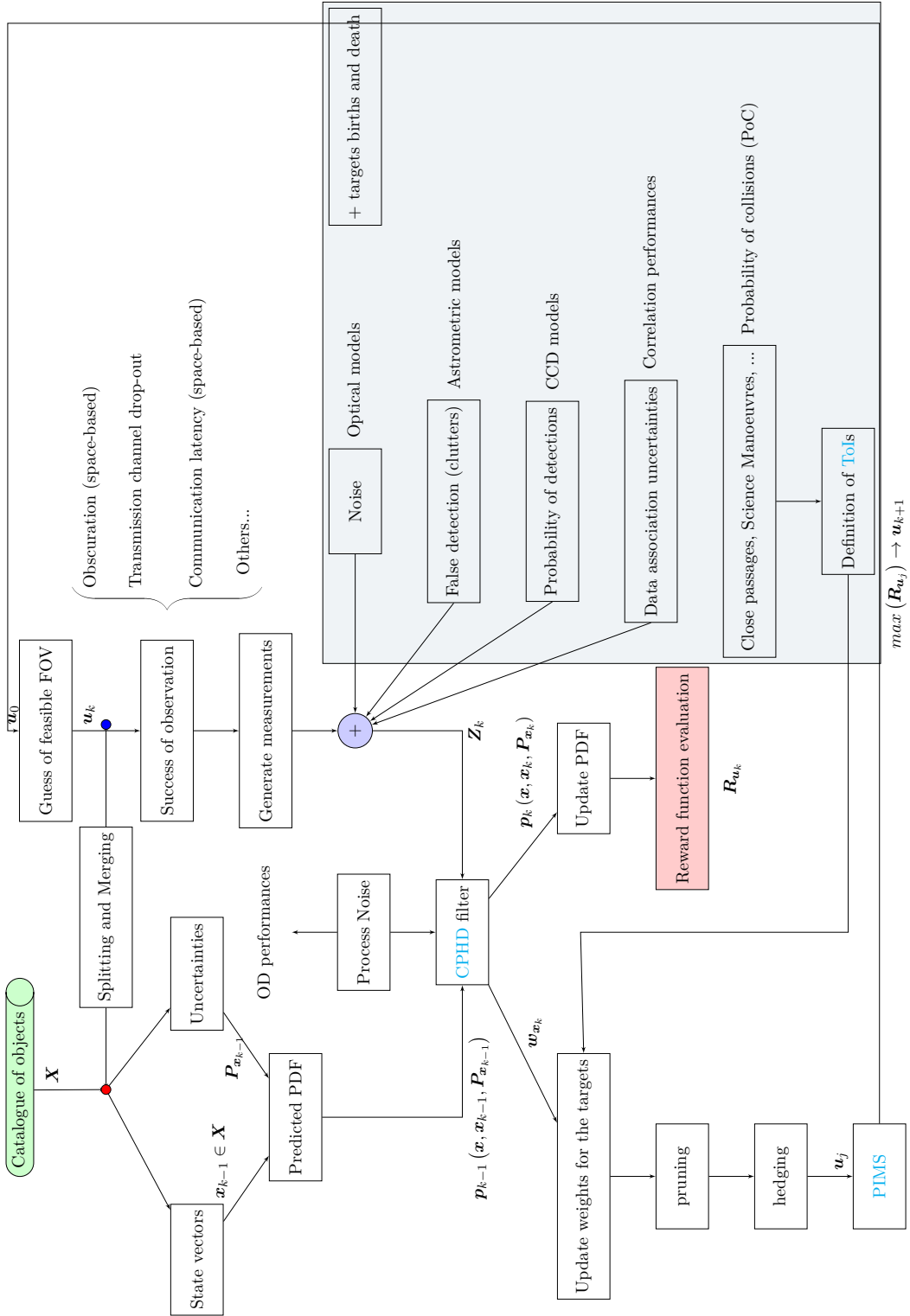
FIGURE 3.10: Functional breakdown of the autonomous cataloguing observation strategy algorithm.

3.5.2 Real Catalogue Maintenance for orbital classes

In [37], has been presented a simulation of the new CPHD applied to catalogue maintenance of objects in the GEO region.

This section will present the results of some simulations conducted to test the performances of CM with the new real-time method and the comparison of these results with classical optimization strategies. The latter rely on the assumption that the CM problem can have a convex-shape representation. They aim to find the optimal solution (understood as possible combinations of observer-target in the time) that maximizes a certain objective function. The objective function can vary according to the method used and will be presented later on.

The first part of this section will describe the background of the simulation: how the catalogue of object has been generated and which sensor network has been considered. The second part of this simulation section will describe the principal results obtained with the CPHD filter implementation for both single optical observers and a network of 2 optical sensors. Additionally, both cases of space-based observers and ground-based facilities will be considered.

3.5.2.1 Creation of the Simulation Catalogue

For this simulations the selected objects for generating the catalogue belong to the geosynchronous class, one of the most crowded orbital region. The initial catalogue of object has been built-up using the online available TLEs for all the objects that respect the following criteria:

- for the same object there are at least 20 instances in the 30 days before the start of the simulation;

- the mean motion of the object is between 0.99 and $1.01 \, \mathrm{revolution \, d^{-1}}$;

- the eccentricity of the orbit is less than 0.001;

- and finally, the object type is one of the following two classes: Payload or debris.

The epoch of the simulation start is the 12th of February 2021 at $19 : 00$ UTC.

As for that date, the objects that respected the previously mentioned constraints were 1076. Starting from the TLEs instances a catalogue of objects has been created, with a mean position and covariance initialization obtained with the same method described in chapter 2.

3.5.2.2 Sensors network

During these simulations four different optical sensors have been considered to highlight the performances for different selections of observer location, accuracy and FOV size. The sensor characteristics are specified in table 3.1. Location of the sensors have been chosen starting from existing facilities, but in order to maintain the generality of this formulation, names and characteristics have been randomly selected. Referring again to table 3.1, the Space-Based Optical Observer (SBOB) is

Table 3.1: Characteristics of the sensors used during the simulations:

Name	Coordinates	FOV dimension	Sensor accuracy
ART	$-6.63°$W $38.22°$N	$\varnothing = 2\,\text{deg}, 2\,\text{deg}$	$\sigma_\alpha = 1'', \sigma_\delta = 1''$
AT1	$150.0°$W $-31.0°$N	$\varnothing = 3.4\,\text{deg}, 3.4\,\text{deg}$	$\sigma_\alpha = 2'', \sigma_\delta = 2''$
AT2	$133.87°$W $-23.70°$N	$\varnothing = 2\,\text{deg}, 2\,\text{deg}$	$\sigma_\alpha = 0.5'', \sigma_\delta = 0.5''$
SBOB	Sun-synchronous orbit at 715 km altitude	$\varnothing = 3.0\,\text{deg}, 3.0\,\text{deg}$	$\sigma_\alpha = 0.5'', \sigma_\delta = 0.5''$

a fictitious LEO object with the following mean orbital elements:

- semi-major axis, $a = 7093\,\text{km}$;

- eccentricity, $e = 0.0014265$;

- inclination, $i = 98.2283°$;

- right-ascension of the ascending node, $\Omega = 150.8478°$;

- argument of the pericenter, $\omega = 129.1774°$.

The Australian Telescopes 1 and 2 (AT1 and AT2, respectively), have been chosen to test different accuracy and FOV size conditions.

3.5.2.3 Accessibility Analysis

For each sensor the following constraints have been applied to check the accessibility of the targets inside the initial complete catalogue presented in subsection 3.5.2.1. As visible in fig. 2.5, with accessibility of an object is meant the observability of the target by a certain observer during all the simulation time. The constraints applied in this framework are:

- that the object must be illuminated by the Sun or being in the penumbra;

- for ground sensors: the Sun shall be below the nautical night elevation of $-9°$;

- for ground sensors: the target shall be between $20°$ and $85°$ of elevation;

- finally, for space sensors: the target shall not be obstructed by the Earth with a limb of 150 km over the surface.

Fig.s 3.11 and 3.13, highlight the visibility constraints for the ground-based observers in a specific instant of time.

3.6 Results

This subsection presents the main results of the simulations conducted within this project. The start of the simulation is the same specified in subsection 3.5.2.1, and the duration of the simulation is 7 days.
The objects propagation is the most time consuming step of the all the simulation. In particular, considering that starting from an initial catalogue of 1076 objects, during the propagation phase $2n_{states} + 1 = 13$[4] times the objects are propagated

---

[4]with n_{states} the number of states inside the state vector

Table 3.2: Coverage performances of the CPHD scheduler for different sensors and SN configurations:

observer or SN	total objects	visible objects	detected objects
ART	1076	342	342 (100.0%)
SBOB	1076	1076	1075 (99.9%)
SN: ART + AT1	1076	674	674 (100.0%)
SN: ART + AT1 + AT2	1076	761	759 (99.7%)

according to the UT theory.

For the propagation has been used 2-body model for gravity perturbations and solar radiation pressure for disturbances.

Before the overall observation-scheduling simulation, a simple accessibility analysis has been conducted for all the observers and all the targets inside the initial catalogue of 1076 objects, to see how many objects are really observable by the specific sensor or SN. The results of this investigation are present in tab. 3.2, together with the detection results obtained with the CPHD scheduler. In this case, with *detected objects* is meant that the object has been maintained inside the catalogue. The first two simulations have been done with a single observer configuration, to test the different coverage conditions for two sensor configurations: in-space and on-ground. The fig.s 3.11 and 3.12, represent the coverage conditions for the sensor ART and SBOB respectively. In fig. 3.11 the represented object positions refer to a small propagation of their orbits for few hours starting from the 12th of February at midnight. The cyan spot represents the position of the ART telescope in Extremadura, Spain. The red dashed line indicates the limit of accessibility of the ART observer, in particular, for the 20° elevation constraint. The objects represented in blue describe the full GEO catalogue used for the simulation, while the green objects correspond to the actually detected targets during the 7 days of simulation. Fig. 3.12, in the same way, represent the detected objects considering the *Space-Based Optical OBserver* (SBOB) observer, and the red objects are the objects that the algorithm did not manage to maintain inside the catalogue. Table 3.2, shows that the ratio of coverage[5] for the ART case is 100.0%. However, not all of these objects are directly tracked or scheduled to be tracked, by the scheduler. In fact, due to the high density of objects, especially in the 0° declination area, some objects will fall inside the FOV of the sensor even when not tracked, that is, the telescope is not pointing directly to them but to an object next to them. Fig. 3.13 shows, on the other hand, the coverage results of the network of sensors composed by ART, AT1 and AT2 sensors. The yellow spot corresponds to the AT2 sensor in Australia. The purple spot, instead, corresponds to the AT1 observer. The dashed lines indicate the limit of accessibility for the three observers, in particular, for the 20° elevation constraint. Each line has the same colour as the sensor to which it refers. The objects represented in blue describe the full GEO catalogue used for the simulation, while the green objects correspond to the actually detected targets during the 7 days of simulation. In

---

[5]The coverage ratio is the number of observed objects over the total number of visible objects during all the propagation $coverage = N_{observed}/N_{visible}$.
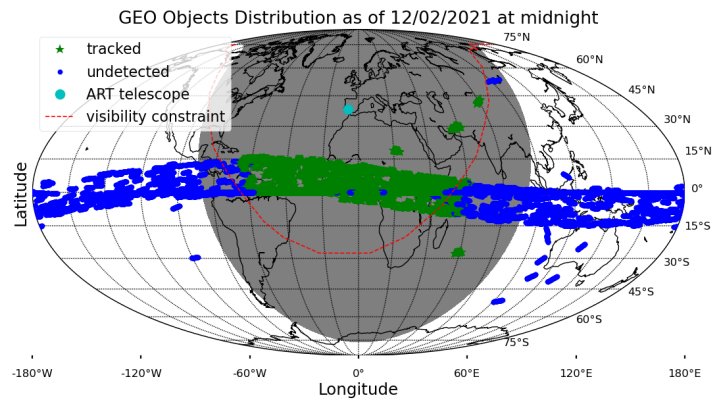
FIGURE 3.11: This figure shows the positions of all the objects inside the catalogue used for the space-based observer simulation of the CPHD filter. Credits: [37].
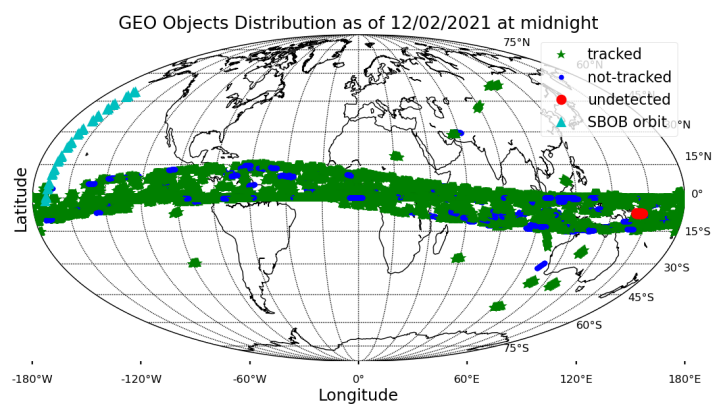
FIGURE 3.12: This figure shows the positions of all the objects inside the catalogue used for the single ground-based observer simulation of the CPHD filter. Credits: [37].
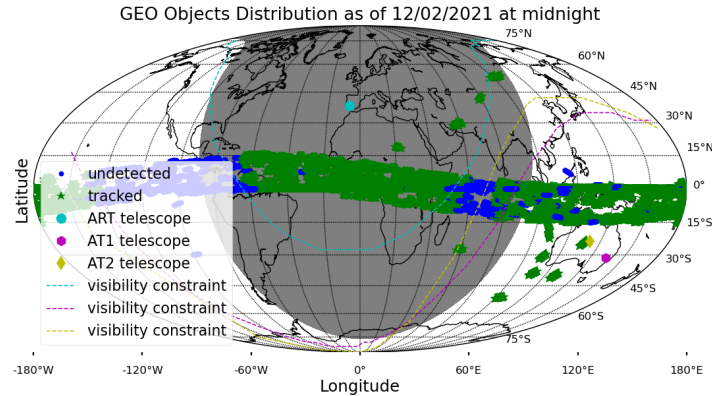
FIGURE 3.13: This figure shows the positions of all the objects inside the catalogue used for the multiple ground-based observers simulation of the CPHD filter. Credits: [37].

fig. 3.14 is presented the covariance trend of the ART sensor scheduling simulation for 7 days. This figure shows the uncertainty trends of all the GM of objects during the 7 nights of propagation. Each plot corresponds to a direction in position and velocity of the *Radial, Tangential, Normal* (RTN)[6] frame: the radial, the tangential and the normal directions. The smaller and dashed lines are for all the objects propagated by the filter, while the ticker red line is the mean value line at each time step for all the objects. Similar results can be shown for other two simulations with AT1, AT2 and SBOB. In particular in fig. 3.15, it is visible the trend of the mean position and velocity errors for all the observation configurations in tab. 3.2. The mean trend corresponds to the average value of all the norm of the diagonal elements of all the covariances of the accessible objects relative to the observer configuration. The mean trend depends on several factors, as the scheduler configuration or the sensor properties. SN configurations, e.g. ART and the Australian observers, can have huge number of observation combinations as specified in subsection 3.4.3.1. The selection of pointing directions at each time step is so reduced for every observer inside the network. This setting explains the peaks $\approx 60\,\mathrm{km}$ of the SN configuration at the beginning of the simulation. A better sensor resolution, instead, leads to a smaller covariance envelope at the end of the simulation.

Simulations have been conducted for single-observer configurations for both cases. Figure 3.16 shows the results of two single-observer simulations performed with ART and SBOB observers. In green the genetic algorithm, in red the CPHD filter presented in this chapter and in blue the greedy method. The upper figure shows the results for the ART telescope case for three days of propagation, while the figure

---

[6]See Appendix 7.1.
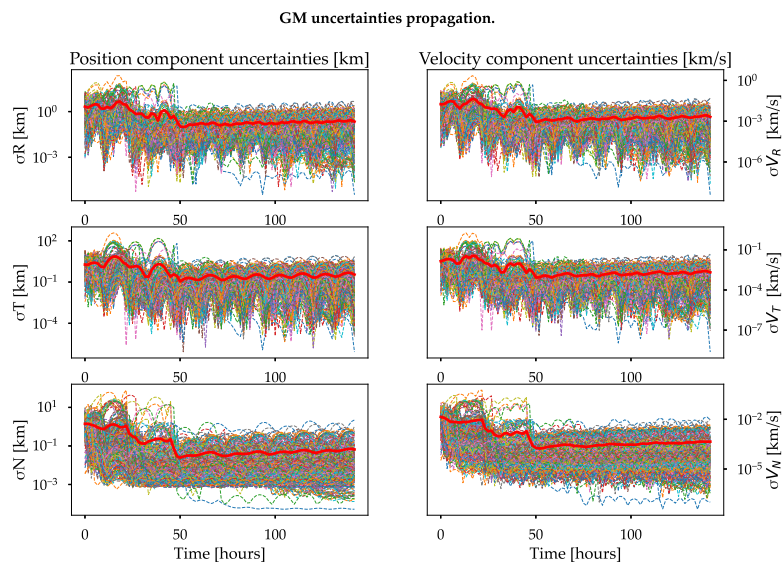
FIGURE 3.14: Uncertainty trends of all the GM of objects during the 7 nights of propagation. Credits: [37].
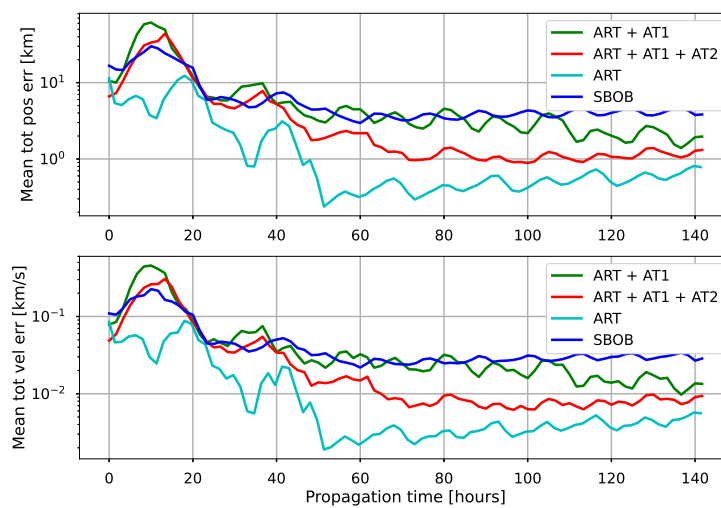
FIGURE 3.15: The mean covariance trends for the four observation configurations presented in tab. 3.2. Credits: [37].

Table 3.3: Coverage performances for the three scheduling methods presented in this Chapter 3, for the ground-observer ART:

		3 nights simulation		
observer	$N_{objects}$	CPHD	ga	greedy
ART	342	98.2%	97.1%	80.4%

Table 3.4: Coverage performances for the three scheduling methods presented in Chapter 3, for the space-observer SBOB:

		1 night simulation		
observer	$N_{objects}$	CPHD	ga	greedy
SBOB	1076	65.5%	82.4%	27.5%

below shows the results for one day of propagation for the SBOB observer. As visible, the CPHD method grants in both cases better performances in averaged accuracy of the object mixture. The greedy-method instead, is very conditioned by the high number of not-observed objects, which covariance trend tends to be dominant. Additionally, due to a fast saturation of the available memory, the simulations have been performed for three days for the ART observer and one single day for SBOB. Tables 3.3 and 3.4, show the coverage performances of the three methods. However, the coverage is not the only parameter that should be taken into account in CM, since also the correct timing to perform a certain observation should be considered. The dimension of the scheduling problem can be defined as number of observation windows $N_{windows}$ times the number of objects $N_{objects}$. Considering that the simulations have been set to perform each observation every 3 minutes, the scheduling dimension of three days simulations for ART and one day for SBOB is around half million. Computationally speaking, the greedy method is the best method for observation scheduling. The dimension of the problem, which can be defined as number of observation windows times the number of objects, is not completely exploited with the greedy method where only the number of actually observable requests is taken into account. Despite the intuitiveness of this method, the main drawback is the extreme simplification of the cost function which does not take into account information gain of an observation. The genetic algorithm, on its side, can be very efficient for small-sized problems (e.g. one night telescope scheduling), but it requires high memory resources when the number of objects to maintain is high. In fact, as said, it makes use of a dedicated binary encoding where the number of bits n_{bits} (also referred as alleles in genetics) is directly related by the number of objects $n_{objects}$ and is given by: $n_{bits} = floor\left(\log(n_{objects})\right) + 1$.
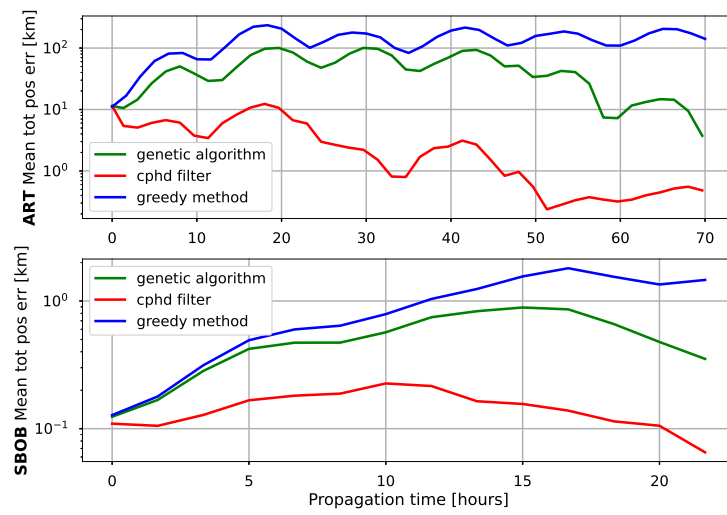
FIGURE 3.16: Mean total position error trends for the three methods analysed. Credits: [37].

Autonomous Observation Strategies for Catalogue Creation 4

The rise of new satellite constellations, especially in the LEO region, together with an increasing number of new launches and wider participation in space-related activities from various entities is pushing Earth's orbits toward maximum capacity. Together with the necessity of a worldwide set of regulations for the *Space Traffic Management* (STM), there is the need to provide proper surveillance support for the cataloguing of the increasing number of uncooperative space objects, e.g. launchers bodies, dismissed satellites and fragmentation events. Differently from radar facilities, in-space and on-ground optical observers can offer additional data (with respect to the canonical observables like coordinates, range and relative rates) and cover higher orbital regions with reduced energy consumptions. Optical sensors offer the possibility to deal with illuminance information of the objects, the albedo information and the change of measured magnitude with time. This information can be combined to perform initial object characterization (e.g. shape and attitude information). However, a certain number of constraints come together with optical sensors: mechanical-constrained slewing capabilities, narrow FOVs, illumination constraints such as the objects need to be in direct sunlight and local darkness (night) in case of ground station observer. When any particular observation strategy is adopted, unpredicted passages or new object detections are generally constituted by short arcs, produced by objects crossing the FOV of an observer at high relative velocities. These short arcs are generally insufficient to trigger properly a weighted least squares reduction of the orbit. Since any initial orbit guess can be correctly established for short detections, the features that possibly generated those detections need to be re-observed in order to be correlated with each other. Despite the wide literature available in the field of short arcs correlation, the sensor scheduling strategies that are necessary to re-observe the same object after a short crossing of the FOV are difficult to be realized by common telescopes and often involve a great number of world-distributed observers to create feasible object coverage. Currently, the biggest challenge for a network of observers is to not be overloaded by redundant tasks and to be optimized in their operations. This chapter will open with a state-

of-the-art review of the common sensor scheduling strategies for re-observation of short arcs, followed by the description of some new methods. The state-of-the-art review will summarize the requirements coming from the correlation and initial orbit determination cataloguing tools necessary for the creation of a catalogue of space objects. The new methods will consider both real-time scheduling strategies to auto-track fast features that are suddenly crossing the FOV of a sensor and post processing strategies to keep track of new detections using CAR to triangulate possible objects that may have generated the measurements. A proper triangulation of the CAR generated by a short arc, together with some refinement filtering techniques in case of more measurements, will allow the generation of a family of VD. Eventually, a proper covariance matrix can be associated with each family of VD and their future observability studied. Additionally, results of the new strategies are going to be present both for simulated scenarios and also for real observation of short arcs campaigns done with ART. The observation strategies will be presented as the completion of a wider cataloguing system that can be fed by different sources, i.e. space-track online catalogue and SMARTnet participation. However, special attention will be given to the catalogue creation chain that is the first essential part of a cataloguing system.

4.1 State of the Art

Collecting measurements for new or undiscovered objects has always been one of the trickiest task for a surveillance system. The aim of surveillance is indeed to build-up a catalogue, even starting from an empty one. Different methods have been presented to support at best the processing chain of measurements coming from newly discovered objects.

Are examples of this the study for an innovative surveillance system presented by Farnocchia in [11], that is considering the studies of Milani on CAR OD methods [30],[29] and [28], and by DeMars [8]. Despite answering well to the necessity of making best use of the collected measurements, especially in the case of very fast observations (or short arcs), lack on the aspects related with the first place observation of the targets themselves.

The literature presents also several studies connected with survey of the sky, strategies to map efficiently the *Field Of Regard* (FoR) of an observer, with the specific scope of collecting measurements of unknown objects. Depending on the orbital region of interest for the survey, some scenarios apply more efficiently than others. It is the case of the geosynchronous area, that has been well studied due to its peculiarity: highly crowded area of objects where most of them are concentrated on the zero declination belt and close to each other and for their relative angular velocity fixed with the Earth's. Scanning strategies for the GEO belt involve heuristic and machine learning methods [17] [25] and applied also to space-based scenario [21].

Ad-hoc methods for real-time tracking are also under the attention of LEO object building catalogues.

4.2 Development of new Observation Strategies

This section collects the new developments that have been introduced in the context of CG during this Thesis. In particular, this new development, is going to be presented divided into three main blocks:

- real-time survey strategies: this is the case of *stare-and-chase* survey strategies, where a sensor is autonomously scheduled to follow an object as soon it crosses its FOV.

- Sky-scanning strategies: that correspond to passive scheduling strategies, where a sensor or network of sensor is performing an offline computed observation plan.

- Post-processing techniques: where survey observation plans are generated after fast or partial observation of objects for which initialization inside a catalogue has been unsuccessful.

This section will analyse the new development and the ideas on the base of these different techniques. Results and analyses are going to be provided for the most relevant cases and example of application scenarios or validation experiments are going to be presented instead on the next chapters, see chapter 6.

4.2.1 Real-time Strategies

One of the most innovative solutions to absolve the task of CG is to respond in real-time to unexpected observations. This type of active scheduling method is supposed to work in a closed-loop framework within the sensor itself, to enhance its autonomy. Despite the great advantages that are related to such a capability, several constraints are challenging to be fulfilled. First of all, there are mechanical constraints, for which not all the platforms supporting the mount of the sensor are able to track within a determined level of accuracy fast objects like LEO satellites. There are computational constraints, like the real-time processing of images and feature detection, which impose strong delays for the sensor tasking. As of last, there can be also sensing constraints. In the case of optical detection, in fact, such a scenario should require at the same time a wide FOV, to cover the biggest portion of the sky as possible, and good accuracy to detect objects that are not in focus and even very faint features. In the context of this Thesis, and as supervision of a student Master's Thesis [26], a new baseline for real-time sensor scheduling, called auto-tracker has been developed and tested. A short presentation of the innovation of this method and its characteristics is explained in the next section, sec. 4.2.1.1. The implementation and characteristics are going to be explained instead in sec. 6.4 on chapter 6.

4.2.1.1 Stare-and-chase scenario

The innovation of the method is based on a different type of image processing that has been implemented specifically for this observation scenario. The idea is to avoid performing a detailed photometric and astrometric reduction of the image but to

use, instead, a coarse processing tool that is simply comparing two sidereal images between each other to detect anomalous features. The limitations of this system are that only a sidereal survey is allowed as the first detection method to check new features crossing the instrument's FOV. Additionally, no proper orbital estimation is performed but a simple first-order approximation of the observables is done.

Due to limitations to the facilities of ART, to perform real-time commanded observations, a first simulation as a baseline for the method has been developed. Later on, real-world observation has been also performed, to detect and track GPS objects. The overall algorithm is composed of a first survey phase, in which the telescope is supposed to point to a fixed position in the sky, compensating for the relative angular velocity of the Earth, in such a way that the stars appear as fixed points in the image. As soon as a non-star object crosses the FOV, and at least three consecutive measurements are collected, the algorithm enters into the auto-tracking phase in which the telescope assumes new pointing positions in order to maintain that feature at the centre of the FOV itself.

The two main components of this auto-tracker are so:

- The pattern-matching routine to compare two consecutive images;

- the closed-loop control system to predict, correct and update the pointing position of the telescope.

A detailed presentation of the method is presented by Lopera in [26].

In Fig. 4.1 is presented an example of the pattern-matching routine applied to a sequence of two images (the first two images starting from the left). The first two images on the left are two consecutive sidereal images, in which a streak feature is visible. On the right, there is the image result of the pattern-matching routine that subtract the two previous images. The algorithm first applies a masking filter to both images in order to transform all the pixel values to either 0 or 1 accordingly if they are over or below the average noise level plus 3σ. Finally, the two images are subtracted from one to the other. Eventually, all the fixed stars will be eliminated one by one and only the object features will remain (with values 1 or -1).

4.2.2 Sky scanning

Sky scanning, or mapping, techniques have a long history in SST field. The idea of Sky scanning is to design an observation grid in the FoR of an observer. That consists in subdividing the accessible sky over an observer in a grid of rectangles, where each element has dimension equal to or smaller than the sensor's FOV. During the observation, the sensor then points the instrument iteratively on those grid elements and performs surveillance. In Fig. 4.2, it is visible a schematization of this approach. The Sky scanning is performed by observing each rectangle element of the sky grid in order to eventually observe objects crossing the FOV. The FoR of the observer is subdiveded in grids, where each rectangular element corresponds to the FOV size of the sensor. During the observation, the sensor points iteratively to each element of the sky-grid to perform surveillance. This approach can be optimized in order to make the best use of the allocated resources inside a sensor network. Indeed, depending on the orbital area of interest of the object research the scanning
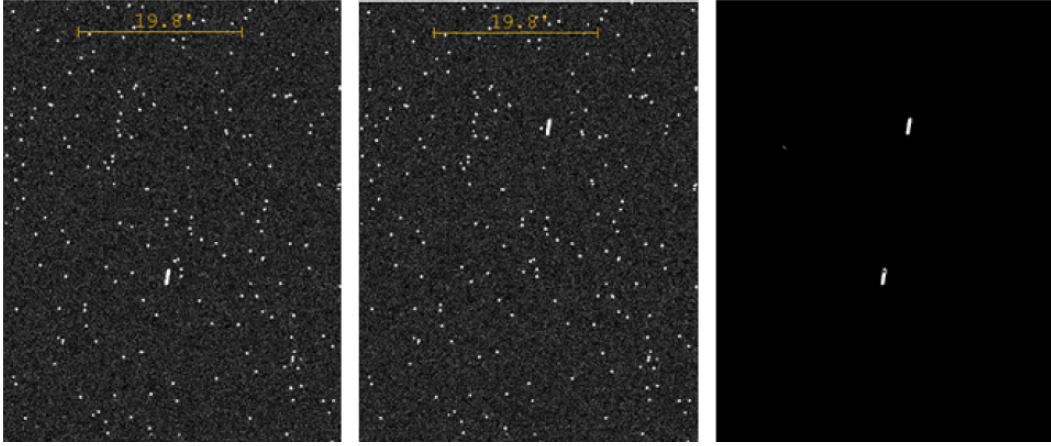
FIGURE 4.1: Example of *pattern-matching* as implemented in the auto-tracker feature of SPOOK. Credits: [26].
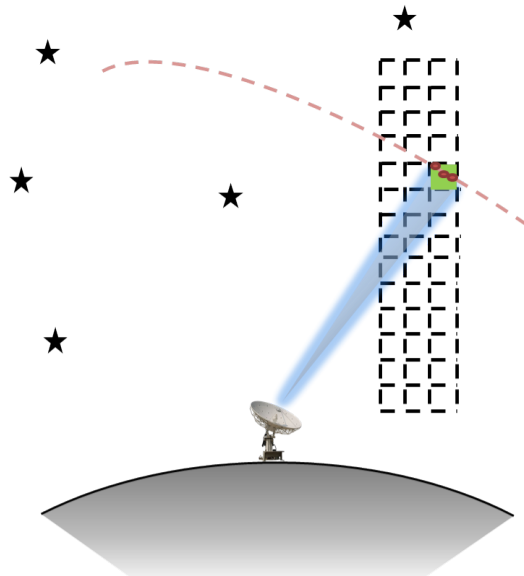
FIGURE 4.2: Example of a ground-based observer Sky scanning.
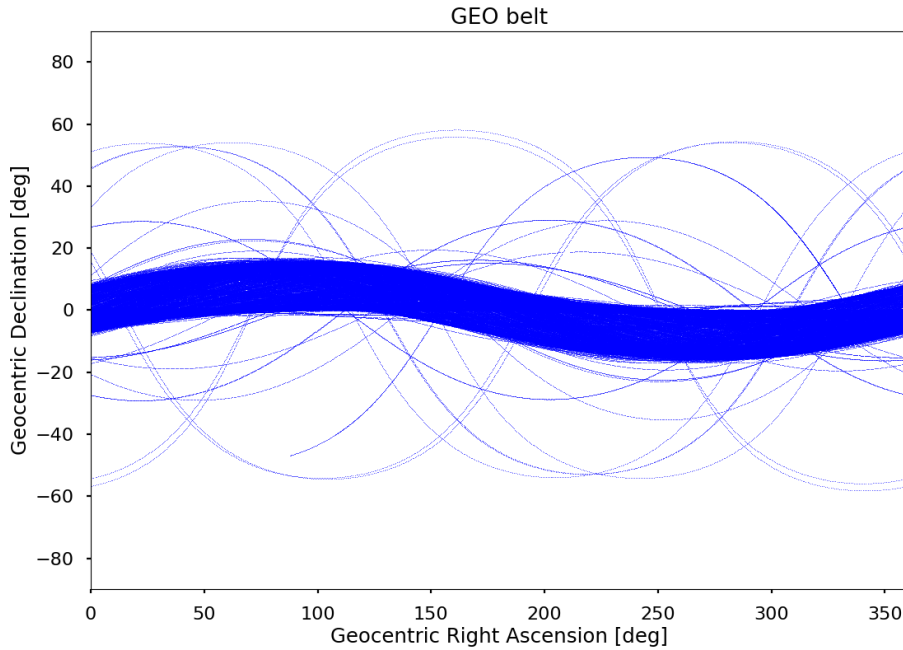
Figure 4.3: Distribution of geostationary objects (retrieved from space-track) in the celestial right ascension and declination plane.

techniques may be optimized in order to avoid redundancies and allow the best observation conditions. The following sections will describe in detail two examples of this optimization for GEO and LEO orbit regions respectively.

4.2.2.1 GEO fence

The GEO fence strategy is based on the observation of the objects that belong to the Geostationary belt around the Earth, at an altitude between $35\,000\,\text{km}$ and $36\,000\,\text{km}$. Due to the peculiar shape of the GEO belt region, some particular observation strategies can be adopted. The scenario has been already presented by the author as a SPOOK's feature in [36].

As visible in Fig. 4.3, the objects on the GEO belt are located around the 0° horizontal line in the geocentric celestial right-ascension and declination plane. Although the objects follow a sinusoidal distribution around the 0°, the effect of the lunisolar orbital perturbation, most of the active satellites are concentrated on the 0° line. This high concentration is even more visible with a look-up on that area, as shown in Fig. 4.4. Properly-placed scanning grids can be placed over the GEO belt in order to maximize observations and revisit times. The most classical observation methods for the GEO belt involve declination-wise scanning. That is, the observer is pointing at a constant right-ascension value (where eventually all the objects will pass during their 1-day revolution) and swiping vertically to higher and lower declination positions in order to catch also more inclined objects.
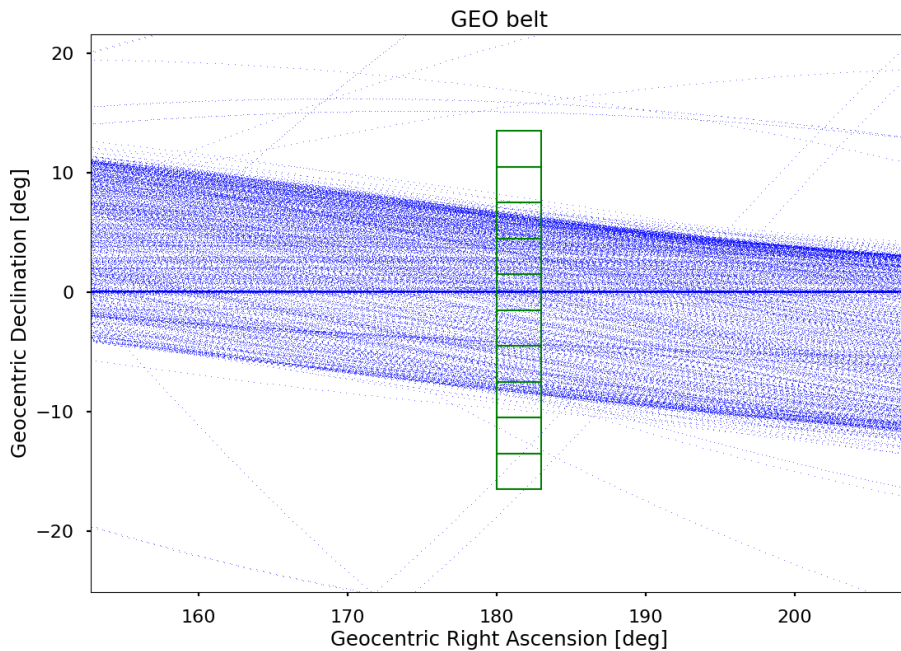
FIGURE 4.4: Zoom-in of the geostationary object distribution from Fig. 4.3.

A property that is important to take into consideration for the GEO belt strategies is the cycle or revisit time. The cycle time is the time that takes to the observer to perform a cycle of observations before coming back to the initial position. When the cycle time is lower than the time the objects need to cross horizontally the FOV, then all the objects that are at that declination will be observed. If an observation plan respects this property, the plan can be considered *leak-proof*. For this purpose, Fig. 4.4 presents an example of a single fence observation strategy for a random observer. In this figure it is also highlighted in green the scanning fence profile of a certain sensor. The main aim of the GEO fence strategy is to fix an observation fence at a precise right-ascension value, where all the objects eventually will pass through, and swap vertically to different declination values in order to increase the coverage. In green are highlighted the rectangular profiles of the FOV positions during the observation. Such a plan is theoretically able to observe all the objects crossing in that declination interval during the whole night, with the condition of being *leak-proof*. An observer on the ground, of course, may have additional constraints, e.g. the Sun elevation, and will have accessibility only to a smaller portion of the GEO belt during a single night. Usually, a typical optical observer with a FOV around 3° has accessibility to a 100° arc of the GEO belt (27% of the total objects). A plan that involves a single fence, however, allows as said a maximum of one observation per object per night. In order to increase the number of observed passages for each object, more vertical fences are necessary. This can be achieved using more sensors or by decreasing the vertical coverage of a single fence and splitting it into more fences.

As described by the author in [36], a dedicated GEO fence method has been integrated inside SPOOK for the generation of plans for ART.

4.2.2.2   LEO mapping

One of the trickiest regions of objects to perform a survey is the LEO region. The LEO region considers all the objects with perigee within 2000 km of altitude from the Earth's surface. It is a highly crowded area of space around Earth (in space-track at least 19 thousand LEO objects are listed).

A survey method to map that region, via a network of optical sensors, has been integrated into SPOOK. A presentation of this new development is going to be presented also in Chapter 6.

The mapping method, suitable for a machine learning application, is based on mapping techniques as presented by Früh in [17]. Differently from that GEO application, in this case, the optimization method is based on LEO observations. The starting point of the algorithm is a dummy catalogue of LEO TLE, as retrieved from space-track. From the catalogue, the position of the objects is propagated at each observation time step and stored properly on some temporary variables.

The algorithm aims to first produce a grid of the spherical observable sky of a given sensor. The dimension of the grid corresponds to the size of the FOV. Afterwards, a specific reward function is associated to each element of this grid in order to estimate the best pointing position (accordingly to the highest reward value). This strategy is performed at each observation step and a mapping observation plan is produced. The overall optimization is based on three main cost functions:

- The observation geometry: it is evaluated in this case the elevation of the pointing element, the phase angle (or distance from the Sun) and other observation constraints relevant for the type of sensor.

- The IOD factor: that means to increase the reward of a possible observation that allows to observe for three times the same object. This reward will be strictly increasing till the third re-observation and then set to a static low value in case of additional observations.

- the *urgency* factor: corresponds to an increased priority to objects that are going to disappear sooner (low elevation and setting velocity).

The second two cost functions, require an initial catalogue of objects to be taken into account as reference system. As explained before, a GP-generated catalogue is used to this scope.

The geometrical constraints can be visualized in Fig. 4.5. This graphics shows the mapping grid generated for a ground-based optical observer at a specific time step. The pointing directions below 20° have not been considered due to observer ground limitations (the walls of the room). The grid colour represent the elevation value, the contour lines represent the angle with respect to the Sun (Sun-observer-pointing direction). In red are visualized the selected pointing direction of the plan up to that instant of time. As visible, the performed pointing directions are concentrated in an area below 100° of angle with the Sun.
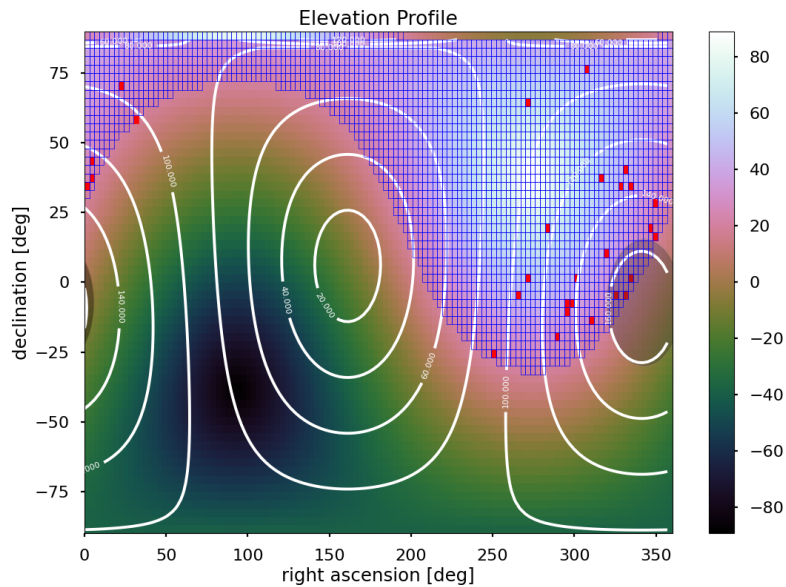
FIGURE 4.5: Observation mapping grid generated for a ground-based optical observer at a specific time step.

4.2.2.3 Space-based Solutions

Similarly to the example of LEO observations from ground-based optical observer, the mapping method can be easily extended to space-based platforms. This is the case of the use case presented in Sec. 6.1.

4.2.2.4 Conjunctions screening

The conjunctions screening is a survey-based technique to monitor the status of close passages of objects as predicted by the conjunction assessment tool. This technique, presented in [36], consists in the following steps:

1. Fetching the last updated LEO catalogue.

2. Perform raw (30 s of time step) accessibility screening to filter only the visible objects.

3. Perform $n \times n$ conjunction assessment on the filtered list.

4. Filter out the conjunctions that are not within the visibility windows of the objects.

5. Perform precise (1 s of time step) accessibility screening of the filtered objects (choosing only one of the object involved in the conjunction) and compute scheduling of the observations.

The information connected with the altitude of the objects and their relative angular velocity is used to assess the integration time of the images and the binning or windowing of the survey. It is estimated that one optical telescope, at an average latitude of 38°, has access to $5 - 10$ conjunctions per night, for an average time of a few minutes per night. Such a plan is not removing too many resources to a sensor involved in SST and can be easily added to each observation plan. In SPOOK and ART operations, this plan has been added as an autonomous service in a separate server with respect to the one where the *Autonomous Cataloguer* is running and added automatically to the ART plan in the morning when it is generated.

4.2.3   Post-processing Strategies

This section presents a new scheduling method as proposed by the author in [38]. The VD method takes its name from the *Admissible Region* (AR) theory developed by Milani [29] [30] [28]. The VD are so-called because they are not real solutions of the orbit but correspond to the classical under-determined problem of the IOD. In fact, a single space object measurement hardly contains enough information to efficiently close the Gauss's problem of IOD.

The main problem that wants to be addressed in this framework is how to deal with short arc observations. As will be explained later in this section, a short arc observation does not contain, typically, enough information to identify precisely the orbit of the object that generated it. And when the orbit of the object that generated the observation cannot be estimated, the object cannot be catalogued, and eventually, it will be lost.

The main question that will be answered in this section is:

- **How to observe again an object which orbit has not been successfully catalogued yet?**

To answer this will be analysed the canonical cataloguing pipeline, as presented in Fig. 4.6, with the addition of a new method for observation planning. The main goal of this new method is to skip the classic cataloguing tools of correlation and orbit determination, in favour of heuristic methods.

4.2.3.1   Virtual Debris algorithm

The new development, related with the VD algorithm, has been presented for the first time by the author in [38]. For the sake of continuity, however, some of the definitions and explanations, are going to be again presented in this section.

The VD algorithm analyses the feasibility of not directly using the measurements of an object to estimate its orbit, but to consider a family of possible orbital solutions for planning observations. If the network of sensors is well optimized for the following up of these objects and the number of these virtual objects is limited, the real object that generated the measurements can be eventually tracked and its orbit finally estimated with enough accuracy.

Fig. 4.6 shows a classical example of concept diagram related to the problem of CG. In Fig. 4.6, inside the two decision blocks: *T2O* stands for Tracklet-to-Object and *T2T* for Tracklet-to-Tracklet. A short arc observation, corresponds to a list

of measurements belonging to an object that crosses the FOV of an observer at a certain time. Those measurements are meant to belong to a single passage of this object. The standard cataloguing processing pipeline can be initialized as usual, and the short arc observation is tried to be correlated to a known object that is already inside an available object catalogue. When the correlation succeeds, OD is
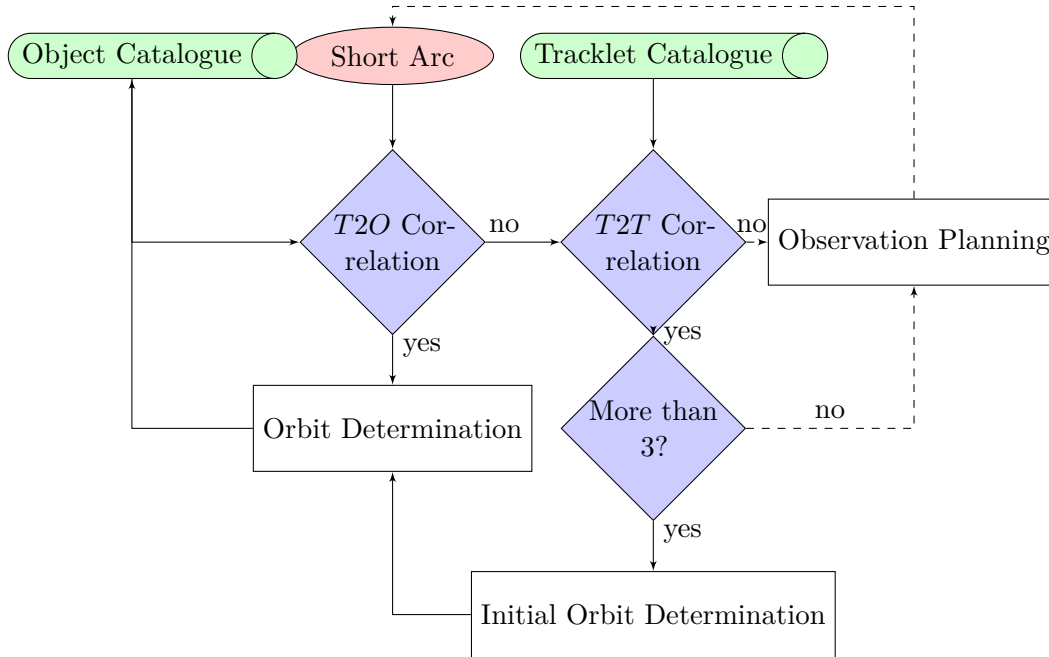
FIGURE 4.6: Standard Catalogue Generation flow chart, plus observation planning block as closing ring of the chain.

applied and the information of that object are updated inside the catalogue. If no correlation is possible, the same measurements are then tried to be correlated with others measurements that are still uncorrelated. If more short arcs are correlated between each other, the literature suggests at least three different passages, the precise orbit of the object can be reduced through classical IOD methods.

In the case all these cataloguing tools are failing, i.e. the object is unknown and cannot be correlated or the measurements are not enough to close the orbit, a new strategy can be adopted to follow up those objects and eventually insert a new object inside the catalogue.

Fig. 4.7, the main block diagram of the VD algorithm is presented. All the short arc observations that have been collected during the observation time, for example a collision survey or a LEO mapping scenario, are processed together to generate a family of possible orbital solutions. Those virtual debris are generated via CAR method.

The process of VD generation will be now presented in details. The main algorithm structure is composed by the four blocks in Fig. 4.7: CAR evaluation, optimal sampling, attribution penalty filter and proximity filter. While the first three blocks are specific to each single short arc observation (or tracklet), the latter is applied to the whole set of VD iteratively.
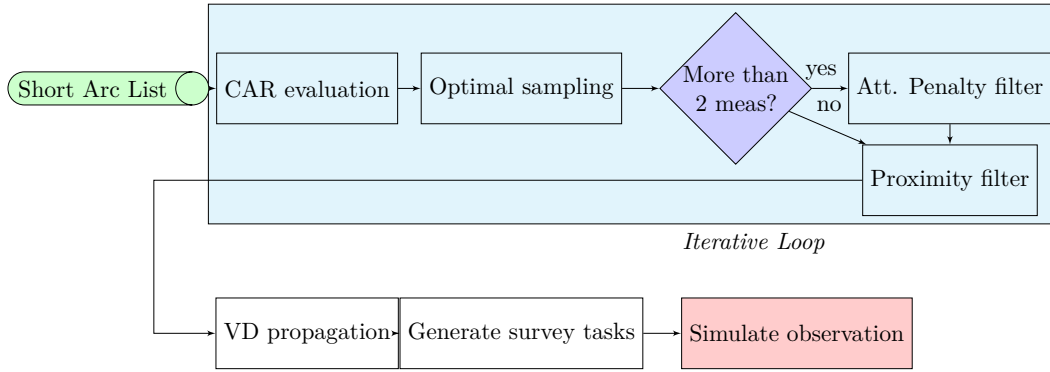
Figure 4.7: Catalogue Generation after short arc measurement flow chart.
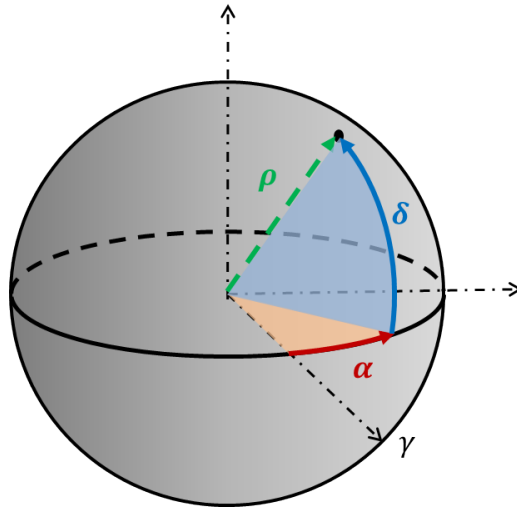
Figure 4.8: Geometrical representation of a point in space expressed with spherical coordinates.

4.2.3.2   CAR evaluation

To familiarize with the concept of CAR, some definition will be proposed in this section. However, the full theory behind this method, as proposed for the first time by Milani [30], will not be topic of this dissertation. Additionally, the author has already provided in [38] a description of how the optimal sampling of the CAR is performed, by means of Delaunay triangulation.

A short arc observation, that can be called also short tracklet, is a list of measurements belonging to a certain object. The measurements, depending from which sources are coming from -i.e. radar, optical telescope, etc., may contain different type of observables. The observables are the quantities that can be directly extracted from the measurements without need to perform any time of estimation filter.

To understand better this nomenclature, it will be useful to express the state vector $\boldsymbol{x}$ of an object through a spherical coordinates representation. Eq. 4.1 express the

spherical coordinates representation of a state vector:

$$\boldsymbol{x} = \left(\alpha, \delta, \rho, \dot{\alpha}, \dot{\delta}, \dot{\rho}\right) \tag{4.1}$$

Where α is the right ascension, δ is the declination and ρ is the range. In Fig. 4.8 those angles can be better understood with an easy geometrical representation. The horizontal angle starting from the γ point is called the right ascension: α. The vertical angle, that starts from the *celestial equator* to the point, is the declination angle: δ. The radial vector to the point, is instead the range: ρ.

With the spherical coordinates representation, it becomes straightforward the passage from observables to state; being the observables themselves part of the state.

The idea of Milani, is so to subdivide the state vector of the object in two parts. The first part collects what can be directly extracted from the measurements and it is called *attributable*: $\boldsymbol{A} = \left[\alpha, \delta, \dot{\alpha}, \dot{\delta}\right]$. The second part represents what can only be estimated (or guessed): $\boldsymbol{B} = [\rho, \dot{\rho}]$. Considering an optical observation, but by analogy can be easily extended to radar measurements, the observable is given by the right ascension and declination α, δ couple. Assuming to initialize the attributable using three optical measurements, a simple *Weighted Least Squares* (WLS) method can be used to extract the attributable:

$$\begin{aligned} \boldsymbol{m}_1 &= \left(\alpha_1, \delta_1\right), t = t_1 \\ \boldsymbol{m}_2 &= \left(\alpha_2, \delta_2\right), t = t_2 \\ \boldsymbol{m}_3 &= \left(\alpha_3, \delta_3\right), t = t_3 \end{aligned} \tag{4.2}$$

Where each measurement is been considered to be taken at a specific time: t_1, t_2 and t_3. The measurement observables can be redistributed in two separated vectors:

$$\begin{aligned} \boldsymbol{\alpha} &= \left[\alpha_1, \alpha_2, \alpha_3\right] \\ \boldsymbol{\delta} &= \left[\delta_1, \delta_2, \delta_3\right] \end{aligned} \tag{4.3}$$

The vectors can be used in a matrix formulation of a WLS linear regression method as in:

$$\begin{aligned} SSE &= \sum_{i=1}^{3} \omega_i \left(\alpha_i - \hat{\alpha} - \hat{\dot{\alpha}}\Delta t_i\right)^2 \\ \omega_i &= 1/\sigma_i \end{aligned} \tag{4.4}$$

Where σ_i is the sensor accuracy, or precision of the measurements. It depends on the telescope system itself and the image processing routine applied. The *hat* variables: $\hat{\alpha}$ and $\hat{\dot{\alpha}}$ are the result of the minimization of the residuals of the Sum of Squares SSE. They correspond to the averaged position of the object at the averaged time:

$$\hat{t} = \left(\sum_{i=1}^{3} t_i\right)/3, \Delta t_i = \hat{t} - t_i \quad i = 1, 3 \tag{4.5}$$

Now we can collect the main coefficients of Eq. 4.4 into the weights $\boldsymbol{W}$ and linear regression $\boldsymbol{X}$ matrices:

$$\boldsymbol{W} = \begin{bmatrix} \sigma_1{}^2 & 0 & 0 \\ 0 & \sigma_2{}^2 & 0 \\ 0 & 0 & \sigma_3{}^2 \end{bmatrix} \quad (4.6) \qquad \boldsymbol{X} = \begin{bmatrix} 1 & \Delta t_1 \\ 1 & \Delta t_2 \\ 1 & \Delta t_3 \end{bmatrix} \quad (4.7)$$

Finally the innovation matrix can be evaluated and os the respective angular coordinate:

$$\boldsymbol{I} = \boldsymbol{X}^T \boldsymbol{W} \boldsymbol{X} \rightarrow \begin{cases} \boldsymbol{P} = & \boldsymbol{I}^{-1} \\ \boldsymbol{d}_\alpha = & \boldsymbol{P} \boldsymbol{X}^T \boldsymbol{W} \boldsymbol{\alpha} \\ \boldsymbol{d}_\delta = & \boldsymbol{P} \boldsymbol{X}^T \boldsymbol{W} \boldsymbol{\delta} \end{cases} \quad (4.8)$$

The attributable $\boldsymbol{A}$ and its accuracy $\boldsymbol{\Gamma}_A$ can be so evaluated:

$$\boldsymbol{A} = \left[\alpha, \delta, \dot{\alpha}, \dot{\delta} \right], \boldsymbol{\Gamma}_A = \begin{bmatrix} \sigma_\alpha & 0 & 0 & 0 \\ 0 & \sigma_\delta & 0 & 0 \\ 0 & 0 & \sigma_{\dot{\alpha}} & 0 \\ 0 & 0 & 0 & \sigma_{\dot{\delta}} \end{bmatrix} \quad (4.9)$$

where:

$$\begin{cases} \alpha = \boldsymbol{d}_\alpha[1]; \dot{\alpha} = \boldsymbol{d}_\alpha[2] \\ \delta = \boldsymbol{d}_\delta[1]; \dot{\delta} = \boldsymbol{d}_\delta[2] \\ \sigma_\alpha = \sigma_\delta = \boldsymbol{P}[1, 1] \\ \sigma_{\dot{\alpha}} = \sigma_{\dot{\delta}} = \boldsymbol{P}[2, 2] \end{cases} \quad (4.10)$$

For this framework two strong assumptions have been considered:

- The accuracies in declination and right ascension directions are uncorrelated: $\sigma_{\alpha\delta} = 0$.

- The accuracy of angular coordinates are the same: $\sigma_\alpha = \sigma_\delta$

Once the attributable has been found, the CAR can be defined, based on some a-priori assumptions. The classical methods to extract the admissible region have been proposed by Milani in [30] and [29]. The principal constraints that have been adopted in this framework are:

- Zero-energy condition: closed orbit assumption.

- Minimum and maximum range.

- Minimum and maximum semi-major axis.

- Maximum eccentricity.

In Fig. 4.9 it is presented an example of CAR typical of optical observations. The constrained region has been on the right ascension and declination plane. In fact, in the case of optical observation the observables are the angular quantities and the unknown set of variables is the range and range rate. In Fig. 4.9 the measurements belong to a GPS satellite, and as typical for that orbital class, the constraints have been chosen accordingly. As visible, the CAR can be quite a wide area, where more orbital regions may be present. The next step will be correct selection of samples to represent this region.
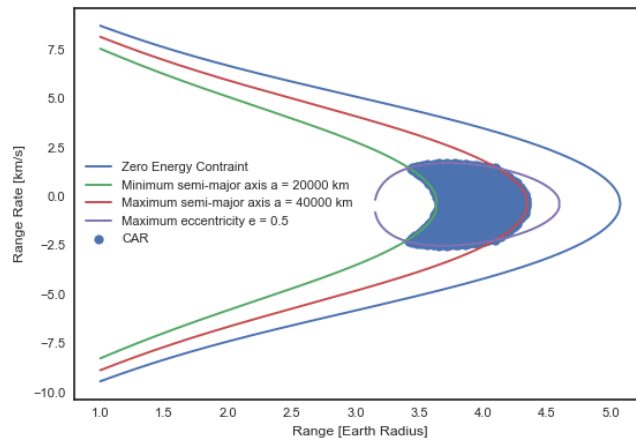
FIGURE 4.9: Example of CAR obtained for a tracklet of optical measurements belonging to a GPS satellite.

4.2.3.3 Optimal Sampling

The definition of the attributable gives a precise idea of the *Observable* state of the object at a precise time. However, the quantities that are not directly observed may assume any value within the CAR. In order to deal in a computational sustainable way with this region, a finite number of samples must be extracted by that region. The sampling can be performed by an easy grid subdivision of the CAR by selecting a minimum interval for the range and range-rate. Another possible solution to perform this task is through the generation of iso-energetic lines to "cut" vertically the CAR and an equally spaced grid division in the range-rate domain.

Anyway, for this algorithm has been selected an optimal sampling method via Delaunay Triangulation [29, 45]. The sampling method has been slightly readapted by the method presented in Milani [29] to include different end-of-iterations routines and border-sampling methods. The sampling algorithm is so composed by a first border-sampling routine, to correct sample the corder of the CAR area, and finally by an iterative Delaunay triangulation-based loop to sample points inside the region.

4.2.3.4 Attribution Penalty Filter

As seen during the attributable generation, only few measurements (3 in the example) are necessary up to this step. However it might be common the case in which the short passage of the object over the observer's FOV have been registered in even more measurements. Even in the case one or two more measurements have been collected, their information can still be used to filter better the area inside the CAR. This passage can be done through the so called attribution penalty filter. A description of how the attribution penalty value is calculated is provided by the author in [38].
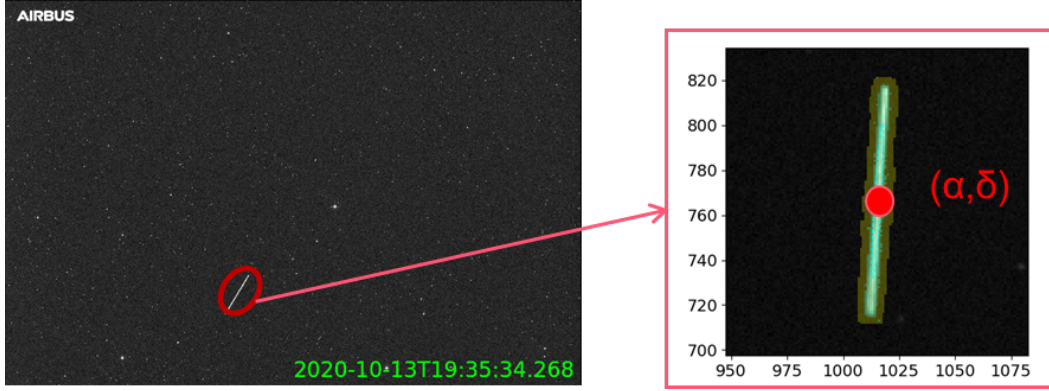
FIGURE 4.10: Example of streak feature that can be extracted by an image.

4.2.3.5 Proximity Filter

When more short arcs observation are processed in batch, it can be possible that more VD superimpose. In this case it is necessary to filter out all the generated CAR points that are sufficiently close to each other. This passage needs to compare the object positions at the same time and for all the objects. To reduce the computational demand of this task a proper Breadth First Search algorithm has been adopted.

4.2.3.6 VD extension

This section concerns a possible extension for the VD algorithm to filter further the number of VD inside the processing loop. The reason behind this choice is to improve the computational tractability of the overall algorithm.

The proposed method makes use of a re-designed version of the *heuristic Initial Orbit Determination* (hIOD) approach made by Wishnek in [53]. Such a method, has been shown to have a great applicability with short-arc streak survey observations. Differently from point-like measurements, where only the central right ascension and declination of the feature is provided, a streak measurement is combined with the value of the streak length. Knowing the length of the streak in *arcseconds* and the integration time of the image, the relative angular velocity of the object can be deduced.

Fig. 4.10 shows an example of streak feature, as can be obtained from a telescope's image. The image has been realized by ART during a sidereal survey scenario. The streak corresponds to an object crossing the FOV of the telescope. Knowing the exposure time of the image t_e and the length of the streak in pixels $\boldsymbol{s} = (\Delta x_{px}, \ \Delta y_{px})$, a first idea of relative angular velocity of the feature can be estimated:

$$v = \begin{cases} \Delta x_{px} * p_{scale}/t_e \\ \Delta y_{px} * p_{scale}/t_e \end{cases} \tag{4.11}$$

Where, in Eq. 4.11, Δx_{px} and Δy_{px} are the horizontal and vertical components of the streak in the image plane measured in pixels and p_{scale} is the *pixel scale*[1].

---

[1]The *pixel scale* of an optical image is the averaged conversion factor between pixel and arcseconds.

The streak angular velocity, together with the coordinates of the centre of the streak, gives the 4 observables of the measurements. As introduced in the previous sections, 6 elements (plus the time) are necessary to completely identify the orbit of an object. For such a reason, only two measurements are theoretically necessary to build-up an overdetermined system for the target state estimation. This allow for a more efficient use of the collected data, and allows to save as many measurement as possible for the next steps of the algorithm, i.e. the attribution penalty filter. The algorithm implementation, with this new integration of the hIOD is presented in Fig. 4.11. In this diagram has been added the extension for the hIOD filter. A system for
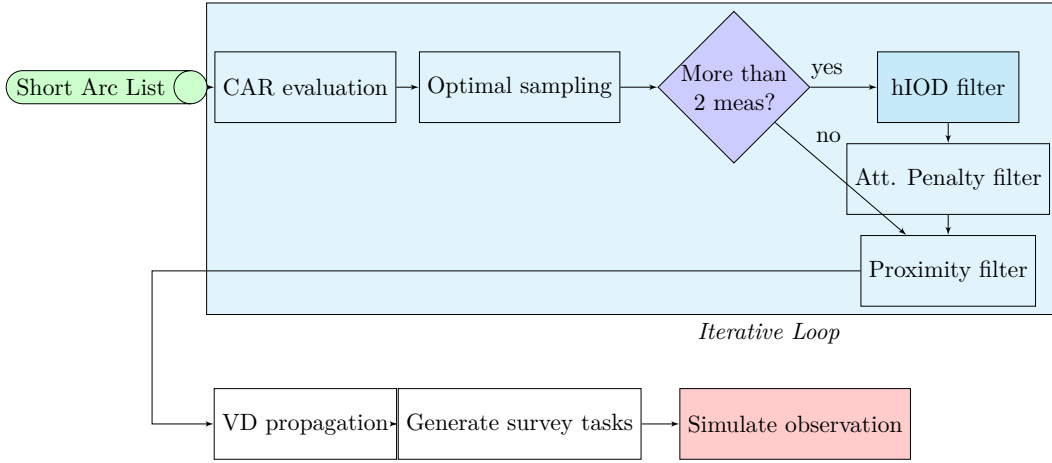
FIGURE 4.11: Catalogue Generation after short arc measurement flow chart.

the estimation of the target state, can be established considering the observation geometry. Indicating with $\boldsymbol{r}_{obj|k}$ the position of the target at time t_k, with $\boldsymbol{r}_{obs|k}$ the position of the observer, ρ the range or distance between the observer and the target and $\boldsymbol{u}_k$ the pointing direction to the target, the following relation is valid:

$$\boldsymbol{r}_{obj|k} = \boldsymbol{r}_{obs|k} + \rho_k \boldsymbol{u}_k \tag{4.12}$$

As support for vectors visualization the reader can refer to Fig. 6.11 in Chapter 6. The first derivative of Eq. 4.12 can be expressed:

$$\dot{\boldsymbol{r}}_{obj|k} = \dot{\boldsymbol{r}}_{obs|k} + \dot{\rho}_k \boldsymbol{u}_k + \rho \dot{\boldsymbol{u}}_k \tag{4.13}$$

The following relations involving the Lagrange coefficients, can be now considered:

$$\begin{aligned}
\boldsymbol{r}_{obj|k+1} &= f_k \boldsymbol{r}_{obj|k} + g_k \dot{\boldsymbol{r}}_{obj|k} \\
\dot{\boldsymbol{r}}_{obj|k+1} &= \dot{f}_k \boldsymbol{r}_{obj|k} + \dot{g}_k \dot{\boldsymbol{r}}_{obj|k}
\end{aligned} \tag{4.14}$$

Where f_k and g_k are the Lagrange coefficients as defined in [6] (in Ch. 2). Just as explanatory example, it can be considered to have observed the object in two different instant of time t_1 and t_2, very close between each other. That is, there are two available measurements. let it be $\boldsymbol{r}_{obj|1}$ the position of the object at t_1 and $\boldsymbol{r}_{obj|2}$ at t_2. The Lagrange equations will become:

$$\begin{aligned}
\boldsymbol{r}_{obj|2} &= f \boldsymbol{r}_{obj|1} + g \dot{\boldsymbol{r}}_{obj|1} \\
\dot{\boldsymbol{r}}_{obj|2} &= \dot{f} \boldsymbol{r}_{obj|1} + \dot{g} \dot{\boldsymbol{r}}_{obj|1}
\end{aligned} \tag{4.15}$$

Where the Lagrange coefficients can be so expressed:

$$
\begin{aligned}
f &= 1 - \frac{\mu |\boldsymbol{r}_{obj|2}|}{h^2} \left(1 - \cos \Delta\theta\right) \\
g &= \frac{|\boldsymbol{r}_{obj|1}||\boldsymbol{r}_{obj|2}|}{h} \sin \Delta\theta \\
\dot{f} &= \frac{\mu}{h} \frac{1 - \cos \Delta\theta}{\sin \Delta\theta} \left[\frac{\mu}{h^2} \left(1 - \cos \Delta\theta\right) - \frac{1}{|\boldsymbol{r}_{obj|1}|} - \frac{1}{|\boldsymbol{r}_{obj|2}|} \right] \\
\dot{g} &= 1 - \frac{\mu |\boldsymbol{r}_{obj|1}|}{h^2} \left(1 - \cos \Delta\theta\right)
\end{aligned}
\tag{4.16}
$$

Where the following relation is also valid:

$$
\dot{f} = \frac{1}{g} \left(f\dot{g} - 1 \right)
\tag{4.17}
$$

The angle $\Delta\theta$ is the angle between the two positions $\boldsymbol{r}_{obj|1}$ and $\boldsymbol{r}_{obj|2}$, can be so defined:

$$
\Delta\theta = \arccos \left(\frac{\boldsymbol{r}_{obj|1} \cdot \boldsymbol{r}_{obj|2}}{|\boldsymbol{r}_{obj|1}||\boldsymbol{r}_{obj|2}|} \right)
\tag{4.18}
$$

And where h is the modulus of angular momentum:

$$
\boldsymbol{h} = \boldsymbol{r}_{obj} \cdot \boldsymbol{v}_{obj}
\tag{4.19}
$$

Combing together Eq.s 4.12 and 4.13 with 4.14:

$$
\begin{aligned}
\boldsymbol{r}_{obs|k+1} + \rho_{k+1}\boldsymbol{r}_{obj|k+1} &= f_k \left(\boldsymbol{r}_{obs|k} + \rho_k \boldsymbol{r}_{obj|k} \right) + \\
&\quad + g_k \left(\dot{\boldsymbol{r}}_{obs|k} + \dot{\rho}_k \boldsymbol{r}_{obj|k} + \rho_k \dot{\boldsymbol{r}}_{obj|k} \right) \\
\dot{\boldsymbol{r}}_{obs|k+1} + \dot{\rho}_{k+1}\boldsymbol{r}_{obj|k+1} + \rho_{k+1}\dot{\boldsymbol{r}}_{obj|k+1} &= \dot{f}_k \left(\boldsymbol{r}_{obs|k} + \rho_k \boldsymbol{r}_{obj|k} \right) + \\
&\quad + \dot{g}_k \left(\dot{\boldsymbol{r}}_{obs|k} + \dot{\rho}_k \boldsymbol{r}_{obj|k} + \rho_k \dot{\boldsymbol{r}}_{obj|k} \right)
\end{aligned}
\tag{4.20}
$$

As suggested by [53], from Eq. 4.20 the terms with the unknowns (ρ and $\dot{\rho}$) can be separated from the others and a systems of equations with unknown variable the range and range can be built:

$$
\begin{aligned}
\rho_{k+1}\boldsymbol{r}_{obj|k+1} - f_k\rho_k\boldsymbol{r}_{obj|k} - g_k\dot{\rho}_k\boldsymbol{r}_{obj|k} - g_k\rho_k\dot{\boldsymbol{r}}_{obj|k} &= \\
f_k\boldsymbol{r}_{obs|k} + g_k\dot{\boldsymbol{r}}_{obs|k} - \boldsymbol{r}_{obs|k+1} \\
\dot{\rho}_{k+1}\boldsymbol{r}_{obj|k+1} + \rho_{k+1}\dot{\boldsymbol{r}}_{obj|k+1} - \dot{f}_k\rho_k\boldsymbol{r}_{obj|k} - \dot{g}_k\dot{\rho}_k\boldsymbol{r}_{obj|k} + \\
- \dot{g}_k\rho_k\dot{\boldsymbol{r}}_{obj|k} &= \dot{f}_k\boldsymbol{r}_{obs|k} + \dot{g}_k\dot{\boldsymbol{r}}_{obs|k} + \\
- \dot{\boldsymbol{r}}_{obs|k+1}
\end{aligned}
\tag{4.21}
$$

From Eq. 4.21, the following system can be extracted:

$$
\boldsymbol{M}\boldsymbol{x} = \boldsymbol{\xi}
\tag{4.22}
$$

Where:

$$
\boldsymbol{M} = \begin{bmatrix} -f_k\boldsymbol{r}_{obj|k} - g_k\dot{\boldsymbol{r}}_{obj|k} & -g_k\boldsymbol{r}_{obj|k} & \boldsymbol{r}_{obj|k+1} & \boldsymbol{0} \\ -\dot{f}_k\boldsymbol{r}_{obj|k} - \dot{g}_k\dot{\boldsymbol{r}}_{obj|k} & -\dot{g}_k\boldsymbol{r}_{obj|k} & \dot{\boldsymbol{r}}_{obj|k+1} & \boldsymbol{r}_{obj|k+1} \end{bmatrix}
\tag{4.23}
$$

$$\boldsymbol{x}^{-1} = \begin{bmatrix} \rho_k & \dot{\rho}_k & \rho_{k+1} & \dot{\rho}_{k+1} \end{bmatrix} \tag{4.24}$$

$$\boldsymbol{\xi} = \begin{bmatrix} f_k \boldsymbol{r}_{obs|k} + g_k \dot{\boldsymbol{r}}_{obs|k} - \boldsymbol{r}_{obs|k+1} \\ \dot{f}_k \boldsymbol{r}_{obs|k} + \dot{g}_k \dot{\boldsymbol{r}}_{obs|k} - \dot{\boldsymbol{r}}_{obs|k+1} \end{bmatrix} \tag{4.25}$$

For this 2-measurements example, the dimension of the system is: $\boldsymbol{M} = (6 \times 4)$, $\boldsymbol{x} = (4)$ and $\boldsymbol{\xi} = (6)$.

Eventually the system may allow more than 2 measurements entry. In this case the system can be extended for more measurements steps, respecting the relation of Eq. 4.22 for each couple of consecutive measurements. The generalization of $\boldsymbol{M}$ matrix in case of n measurements and the other components of the system, $\boldsymbol{x}$ and $\boldsymbol{\xi}$ can be so represented:

$$\boldsymbol{M} = \begin{bmatrix} -f_k \boldsymbol{r}_{obj|1} - g_k \dot{\boldsymbol{r}}_{obj|1} & -g_k \boldsymbol{r}_{obj|1} & \boldsymbol{r}_{obj|2} & \boldsymbol{0} & \boldsymbol{0} & \boldsymbol{0} & \cdots \\ -\dot{f}_k \boldsymbol{r}_{obj|1} - \dot{g}_k \dot{\boldsymbol{r}}_{obj|1} & -\dot{g}_k \boldsymbol{r}_{obj|1} & \dot{\boldsymbol{r}}_{obj|2} & \boldsymbol{r}_{obj|2} & \boldsymbol{0} & \boldsymbol{0} & \cdots \\ \boldsymbol{0} & \boldsymbol{0} & -f_k \boldsymbol{r}_{obj|2} - g_k \dot{\boldsymbol{r}}_{obj|2} & -g_k \boldsymbol{r}_{obj|2} & \boldsymbol{r}_{obj|3} & \boldsymbol{0} & \cdots \\ \boldsymbol{0} & \boldsymbol{0} & -\dot{f}_k \boldsymbol{r}_{obj|2} - \dot{g}_k \dot{\boldsymbol{r}}_{obj|2} & -\dot{g}_k \boldsymbol{r}_{obj|2} & \dot{\boldsymbol{r}}_{obj|3} & \boldsymbol{r}_{obj|3} & \cdots \\ \cdots & \cdots & \cdots & \cdots & \cdots & \cdots & \cdots \\ \boldsymbol{0} & \cdots & \boldsymbol{0} & -f_k \boldsymbol{r}_{obj|n-1} - g_k \dot{\boldsymbol{r}}_{obj|n-1} & -g_k \boldsymbol{r}_{obj|n-1} & \boldsymbol{r}_{obj|n} & \boldsymbol{0} \\ \boldsymbol{0} & \cdots & \boldsymbol{0} & -\dot{f}_k \boldsymbol{r}_{obj|n-1} - \dot{g}_k \dot{\boldsymbol{r}}_{obj|n-1} & -\dot{g}_k \boldsymbol{r}_{obj|n-1} & \dot{\boldsymbol{r}}_{obj|n} & \boldsymbol{r}_{obj|n} \end{bmatrix} \tag{4.26}$$

$$\boldsymbol{x}^{-1} = \begin{bmatrix} \rho_1 & \dot{\rho}_1 & \rho_2 & \dot{\rho}_2 & \rho_3 & \dot{\rho}_3 & \cdots & \rho_n & \dot{\rho}_n \end{bmatrix} \tag{4.27}$$

$$\boldsymbol{\xi} = \begin{bmatrix} f_1 \boldsymbol{r}_{obs|1} + g_1 \dot{\boldsymbol{r}}_{obs|1} - \boldsymbol{r}_{obs|2} \\ \dot{f}_1 \boldsymbol{r}_{obs|1} + \dot{g}_1 \dot{\boldsymbol{r}}_{obs|1} - \dot{\boldsymbol{r}}_{obs|2} \\ f_2 \boldsymbol{r}_{obs|2} + g_2 \dot{\boldsymbol{r}}_{obs|2} - \boldsymbol{r}_{obs|3} \\ \dot{f}_2 \boldsymbol{r}_{obs|2} + \dot{g}_2 \dot{\boldsymbol{r}}_{obs|2} - \dot{\boldsymbol{r}}_{obs|3} \\ \cdots \\ f_{n-1} \boldsymbol{r}_{obs|n-1} + g_{n-1} \dot{\boldsymbol{r}}_{obs|n-1} - \boldsymbol{r}_{obs|n} \\ \dot{f}_{n-1} \boldsymbol{r}_{obs|n-1} + \dot{g}_{n-1} \dot{\boldsymbol{r}}_{obs|n-1} - \dot{\boldsymbol{r}}_{obs|n} \end{bmatrix} \tag{4.28}$$

In this generalized n-measurements case, the dimension of the system is: $\boldsymbol{M} = (6(n-1) \times 2n)$, $\boldsymbol{x} = (2n)$ and $\boldsymbol{\xi} = (6(n-1))$. Although the system can be used directly for a least-squares method to determine the vector of unknowns $\boldsymbol{x}$, as a common IOD method, this approach it is not well applicable to short arcs observations, where the number of measurements is very limited and the time step is very short. The idea, as suggested by [53], is to use an heuristic approach (hIOD) to find a minimum solution to the problem:

$$\boldsymbol{M}\boldsymbol{x} - \boldsymbol{\xi} = 0 \tag{4.29}$$

That can be reformulated in a cost function for a minimization problem, to find the root $\boldsymbol{x}$ which minimizes the function:

$$f(\boldsymbol{x}) = \boldsymbol{W}\left(\boldsymbol{M}\boldsymbol{x} - \boldsymbol{\xi}\right) \tag{4.30}$$

Where the weighting matrix $\boldsymbol{W}$ can express the different weights that can be considered for the variables of the problem. The typical case is in fact to increase the weights associated with the orbital range and decrease for orbital velocities which have usually less accuracy.

In the next section (sec. 4.2.3.7), the minimization problem will be explained as optimization problem through PSO.

4.2.3.7   PSO optimization

Without the need of an detailed description of the method, quite well presented in the literature, the heuristic optimization has been realized through a PSO method. The standard algorithm for hIOD is presented in Fig. 4.12, where it is visible that the initial population of particles is initialized through the canonical CAR analysis. Similarly for the hIOD filter, as the block presented in Fig. 4.11, the initial population
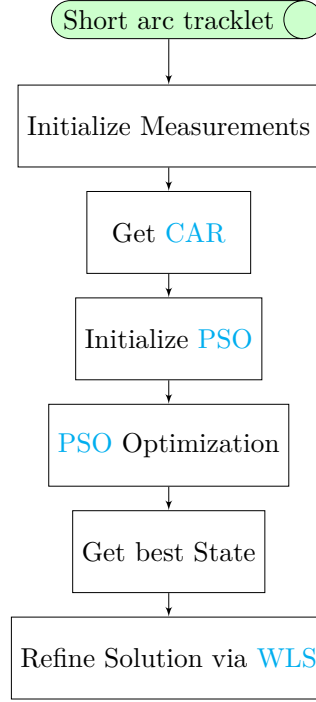
FIGURE 4.12: Generalized block diagram of a hIOD algorithm.

is the direct output of the Delaunay triangulation. This process, with particular highlight to the PSO implementation is presented in Fig. 4.13. In blue scope, it is visible the algorithm of the PSO optimization as implemented in SPOOK. In alg. 1, it is reported the algorithm internal of the PSO optimization algorithm. The canonical PSO makes use of a set of particles ($N_{particles}$) which correspond to possible solution of the system. This particles are characterized by a position, $\boldsymbol{pos}_{i,k}$ with i the iteration step and k the particle number, (with the size of the unknown variable, in this case $\boldsymbol{pos}_{i,k} = \left[\alpha, \delta\right]$) and a velocity $\boldsymbol{vel}_{i,k}$. The velocity correspond to the position the particles will reach at the next iteration. The particles will be so updated for all the iterations ($N_{iterations}$) in this way:

$$\boldsymbol{pos}_{i,k} = \boldsymbol{pos}_{i-1,k} + \boldsymbol{vel}_{i-1,k} \tag{4.31}$$

For $i = 1, N_{ierations}$ and for $k = 1, N_{particles}$.

During each iteration, for each particle it is evaluated the fitness function. The fitness function itself is the weighted combination of 5 different objective functions:

1. the Lagrangian objective function from Eq. 4.30;
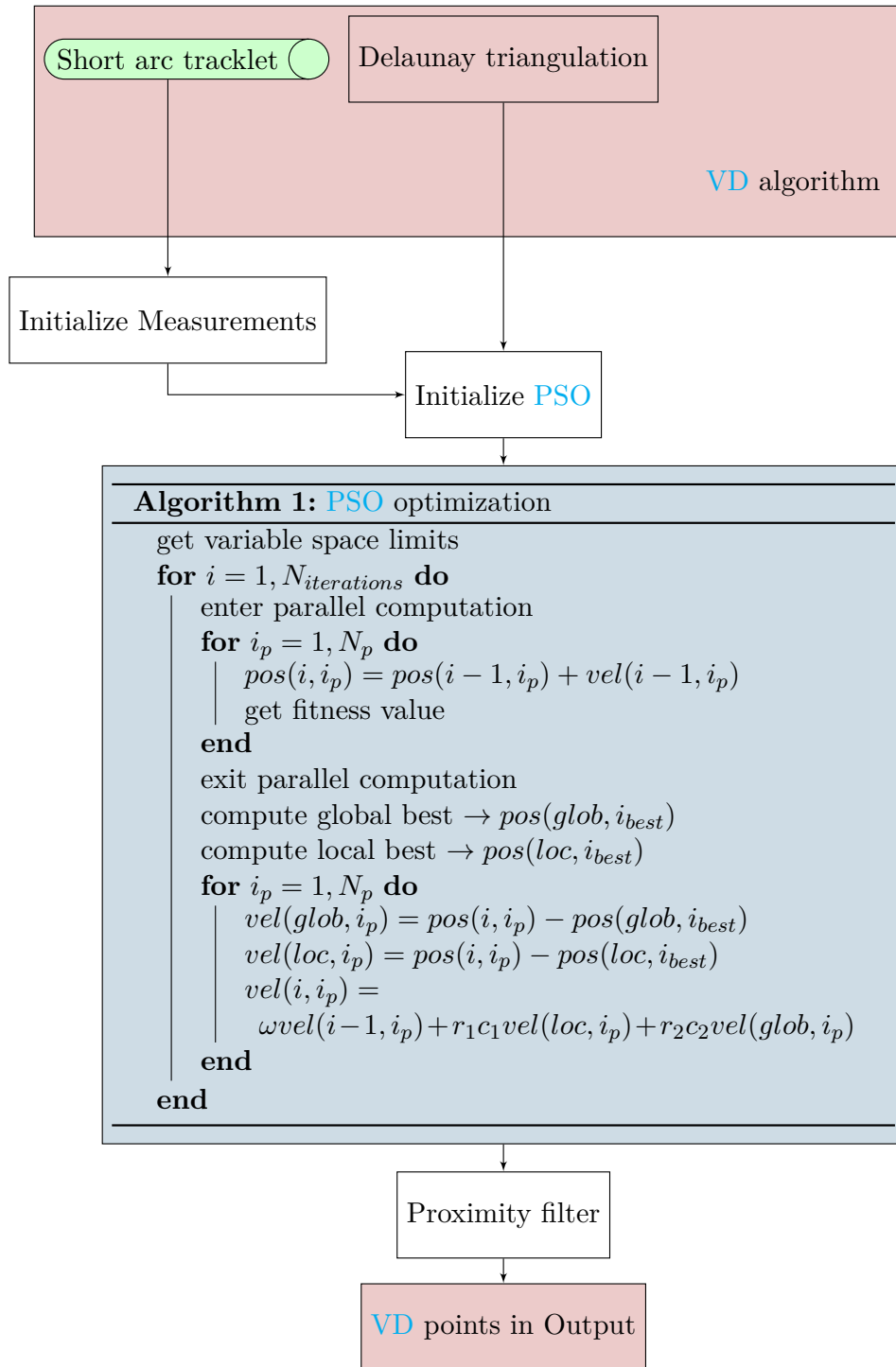
FIGURE 4.13: Detailed block diagram of the hIOD filter as extension of the VD algorithm.

2. the difference between the propagated pointing vector from the initial guess and the real pointing vector to the object from the measurement;

3. the difference between the propagated angular velocity from the initial guess and the real angular velocity of the object from the measurements;

4. the range distance from the circular IOD guess;

5. the range rate difference with respect to the circular IOD guess.

To understand the points 2 and 3 needs to be considered the hIOD optimization as described in [53]. When more than 2 measurements are available, the additional measurements will go to extend the system size as in Eq. 4.26. However, the range and range rate guess are done only for the first measurement instant of time (ρ_1, $\dot\rho_1$). The range and range rate couples for the future time steps, corresponding to the additional measurements, is obtained propagating the initial spherical state vector using SPOP. The propagation of the full state, will also update the propagated observables at the next measurement times. These quantities can be, indeed, compared with the real observed ones to obtain an additional objective function that needs to be minimized.

As for the last two points (4 and 5), it has been considered the solution to the simplified-circular IOD as explained in [2] (pp. 369-370). For the circular orbit assumption are, in fact, necessary only 2 measurements. Given the specific geometry of a perfectly circular orbit centred on Earth and the position of the observer, it is possible to determine the range $\rho_{circular}$ and range-rate $\dot\rho_{circular}$ of the object through an easy bi-section method. Specifically, the method attempts to compare the time the object required to cover the angular distance between the two measurements considering the dynamic model of a circular orbit, and the real time difference between the measurements instances.

The general expression of such a fitness function is given in Eq. 4.32.

$$
\begin{aligned}
f &= \omega_1 f_1 + \omega_2 f_2 + \omega_3 f_3 + \omega_4 f_4 + \omega_5 f_5 \\
f_1 &= \| \boldsymbol{W} \left(\boldsymbol{Mx} - \boldsymbol{\xi} \right) \| \\
f_2 &= \arccos \left(\boldsymbol{u}_{propagated} \cdot \boldsymbol{u}_{real} \right) \\
f_3 &= \sqrt{ \left(\dot\alpha_{real} - \dot\alpha_{propagated} \right)^2 + \left(\dot\delta_{real} - \dot\delta_{propagated} \right)^2 } \\
f_4 &= \rho_1 - \rho_{circular} \\
f_5 &= \dot\rho_1 - \dot\rho_{circular}
\end{aligned}
\tag{4.32}
$$

Where ω_i with $i = 1, 5$ are the weights applied to each fitness contribution. To recall the observable definition presented in 4.2.3.2, the pointing vector to the object can be obtained from the observables as follow:

$$
\boldsymbol{u} =
\begin{bmatrix}
\cos\alpha \cos\delta \\
\sin\alpha \cos\delta \\
\sin\delta
\end{bmatrix}
\tag{4.33}
$$

Inside alg. 1, it is visible that the fitness function evaluation is done in parallel computation loop. Out of the parallel loop, after all the fitness values have been calculated for all the particles, the velocities of the particles are updated:

$$
vel(i, k) = \omega_v vel(i - 1, k) + r_1 c_1 vel(loc, k) + r_2 c_2 vel(glob, k)
\tag{4.34}
$$
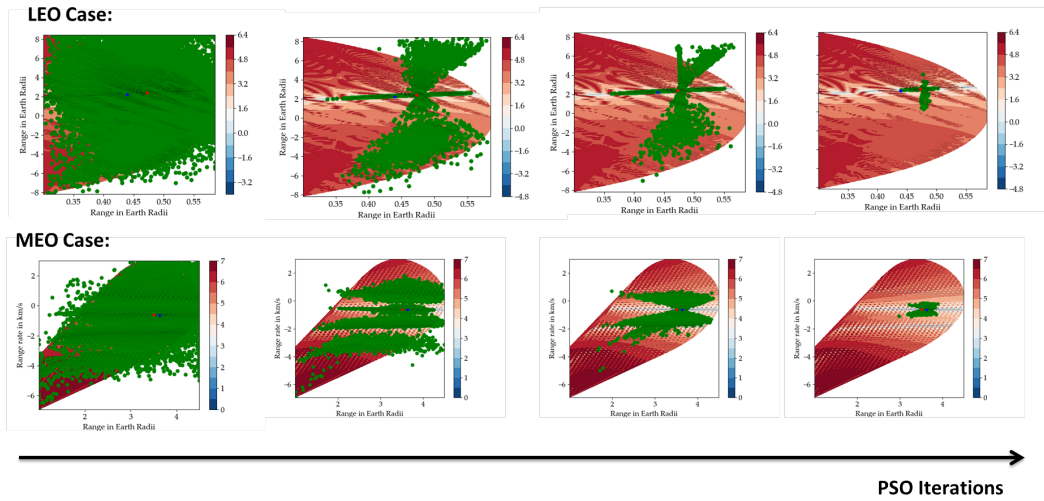
FIGURE 4.14: Evolution of the position of the particles at each new generation step, plotted against the CAR.

Where ω_v is the weight associated to the inertia of the particle, that means, how much the particle tends to maintain the same velocity. $vel(loc, k)$ and $vel(glob, k)$ are the vector pointing to the local minimum of the iteration i and the global minimum of all the iterations. r_1 and r_2 are inherent random variables that may assume any value between 0 and 1 for each different particle, and c_1 and c_2 are the corresponding weights to assure convergence to the best solution both locally and globally for all the iterations.

The weights ω_v, c_1 and c_2 have not been considered to be static, but are evolving during the iterations:

$$
\begin{aligned}
\omega_v &= 0.4 \frac{i_{iteration} - N_{iterations}}{N_{iterations}^2} + 0.5 \\
c_1 &= -1 \frac{i_{iteration}}{N_{iterations}} + 1.05 \\
c_2 &= 0.5 \frac{i_{iteration} - N_{iterations}}{N_{iterations}^2} + 0.05
\end{aligned}
\tag{4.35}
$$

Those values have been found empirically.

An example of particle position evolution during the iterations is visible in Fig. 4.14. In Fig. 4.14, the color-bar of the CAR area respects the values of the fitness function as evaluated with Eq. 4.32. The particles have been highlighted in green. On top: the case of a LEO observation. On the bottom: the case of a MEO observation. The plots evolve from left to right with the number of the iterations.

Referring again to Fig. 4.12 and the last block, it is important to highlight how the heuristic method for IOD lack of a good analysis of the uncertainty connect with the optimal orbital solution found. For such a reason the algorithm for hIOD has been integrated with a WLS refinement of the solution using the collected measurements in order to produce a scaled covariance for the state vector. In the case of the hIOD filter extension to the VD algorithm, this passage has been skipped

77

and the uncertainty has been taken into account selecting all the particles at the end of the iterations and not only the one corresponding to the best fitness. As shown in Fig. 4.13, the heuristic filter is followed by the proximity filter block, completely analogue to the proximity filter in sec. 4.2.3.5, that has the aim to prune the number of particles in the cloud of solutions, but still keeps the uncertainty information given the cloud of resulting points after filtering.

4.3 Results

Results of the first version of the VD scheduler have been presented by the author in [38]. In this case, the code have tested with a practical example of fragmentation bodies detection. For the seek of continuity and completeness of the Thesis, the example will be proposed again in the next chapters, see chapter 6, sec. 6.3.1.2. In Fig.s 4.15 and 4.16 are presented some results of hIOD applied to real short arc observations obtained with ART. In both cases has been analysed a short of 4 measurements coming from a LEO mapping survey, the tracklet has been collected over a time span of 4.2 seconds with a frame rate of 1.4 seconds. The images have been collected using a 2×2 binning and 0.5 seconds of exposure. The observed object belonged to the $M067$ satellite of the *GLOBALSTAR* constellation, NORAD: 32263. The plot in Fig. 4.15 shows the result of the hIOD algorithm as error of the orbit determination results against the ephemeris generated via TLE (General Perturbations method) over a 2.5 hours propagation after the measurements. The reference has been originated via TLE. Measurements are real-word data obtained with ART. The results show that the heuristic algorithm manages well to contain the tangential and radial errors within the uncertainty intervals, but the errors on the radial position and tangential velocity are quite underestimated. In Fig. 4.16 instead, the same hIOD results are compared against the ephemeris obtained via *Special Perturbations* (SP). The reference has been originated via SP. Measurements are real-word data obtained with ART. In this case it is visible how the OD routines manage to maintain the error within the uncertainty limits. These examples, aimed to represent a validation of the heuristic method for IOD, show how the algorithm can be good enough to already give a good estimation of the orbit, but lack of a good uncertainty estimation that will eventually make diverge whatever propagation tool can be used after the initial estimation. To assess this problem a better analysis of the results of IOD should be conducted with well known orbits in order to refine the scale factor to give to the covariance after the WLS final refinement. A possible analysis of this type can be conducted with SP data from space-track. For completeness of information, and to validate the robustness of the estimator and WLS refinement, an example of 100 MC simulation of orbit propagation after hIOD estimation is proposed in Fig. 4.17. Also in this case the reference has been originated via SP. Measurements are real-word data obtained with ART. The MC distribution of random orbital solution has been realized considering the mean value of the solution of the heuristic estimator and the covariance resulting from the WLS refinement. As shown in the figure, the possible orbital solution are well contained within the 3σ covariance envelope. Also for this cases, the errors have been considered against the SP ephemeris of that specific object. The validation of the hIOD extension to the
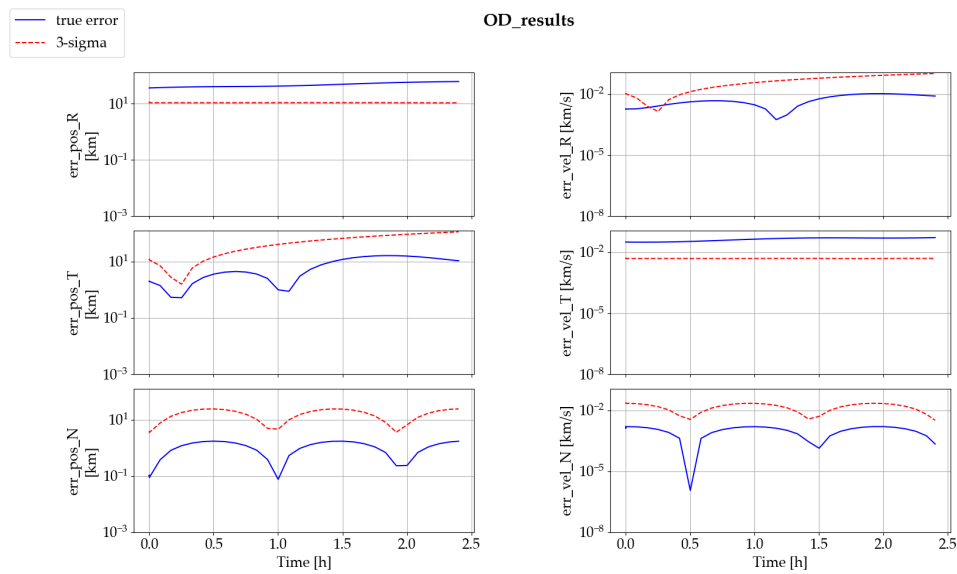
FIGURE 4.15: Estimated covariance and residuals to orbit reference after heuristic IOD for a single object propagation with initialization via TLE.
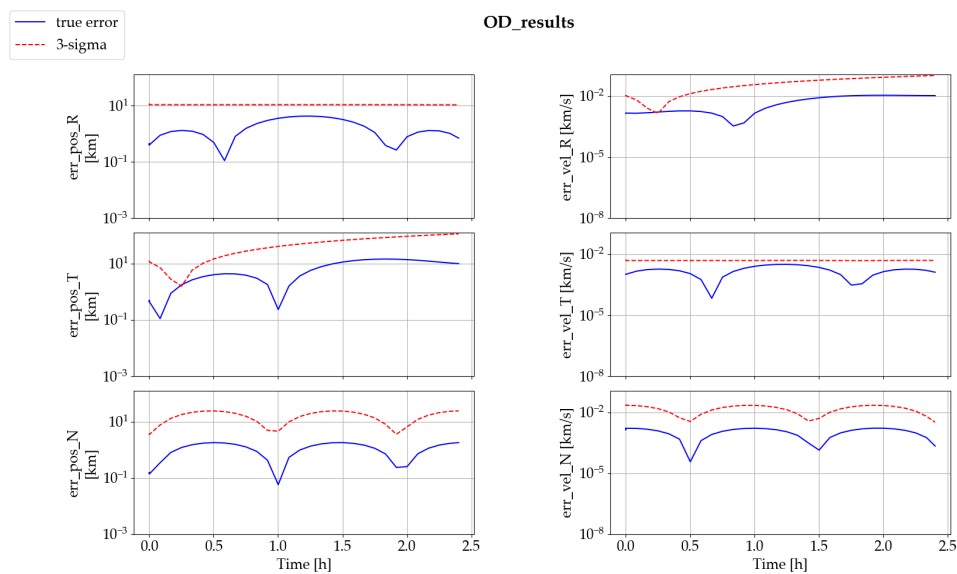
FIGURE 4.16: Estimated covariance and residuals to orbit reference after heuristic IOD for a single object propagation with initialization via SP.
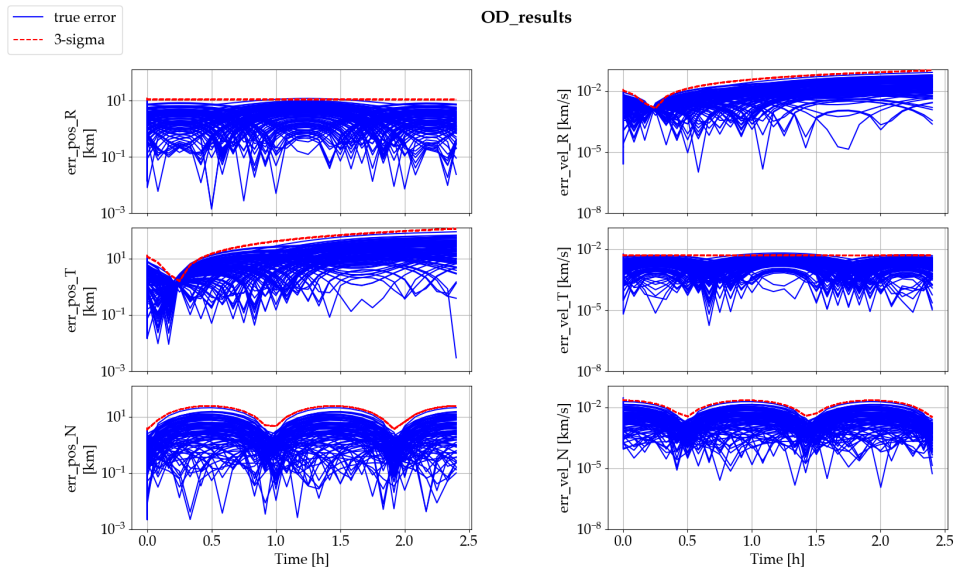
Figure 4.17: Estimated covariance and residuals to orbit reference after heuristic IOD using a 100 elements MC distribution (object: 32263).

VD scheduler is presented in Fig.s 4.18 and 4.19. In Fig. 4.18, the reference has been originated via SP. Measurements have been simulated via SPOOK tool. A green line has been added to highlight the reference error to consider the uncertainty entirely contained inside a 3° FOV. As visible from the graphs, the classical OD routines are not enough to reduce efficiently the orbit of the object, being the real error after one day of simulation higher than the 3σ covariance envelope. The real error is also higher than the FOV limit envelope. Anyway, the VD algorithm managed to observe the object again and reduce its orbital uncertainty.

As for Fig. 4.19, the reference has been originated via SP. Measurements have been simulated via SPOOK tool. A green line has been added to highlight the reference error to consider the uncertainty entirely contained inside a 3° FOV. As visible from the graphs, the classical OD routines are not enough to reduce efficiently the orbit of the object, being the real error after one day of simulation higher than the 3σ covariance envelope. The real error is also higher than the FOV limit envelope. Anyway, the VD algorithm managed to observe the object again and reduce its orbital uncertainty.

Both scenarios tries to highlight the importance of the method in terms of re-observability of objects that generated short arcs observations. In fact, an even precise IOD estimation is not enough to allow a late revisit of the target, for example the day after. This limit can be visualized on both graphs thanks to an horizontal green line on the tangential and normal position panels. This line corresponds to the pointing error envelope at which the object, with its specific distance from the observer, can be observed and remain within the FOV. On both cases, it is visible how all the 100 MC cloud of orbital solutions get outside this envelope (especially on the tangential frame), that means the object is not observable anymore due to the
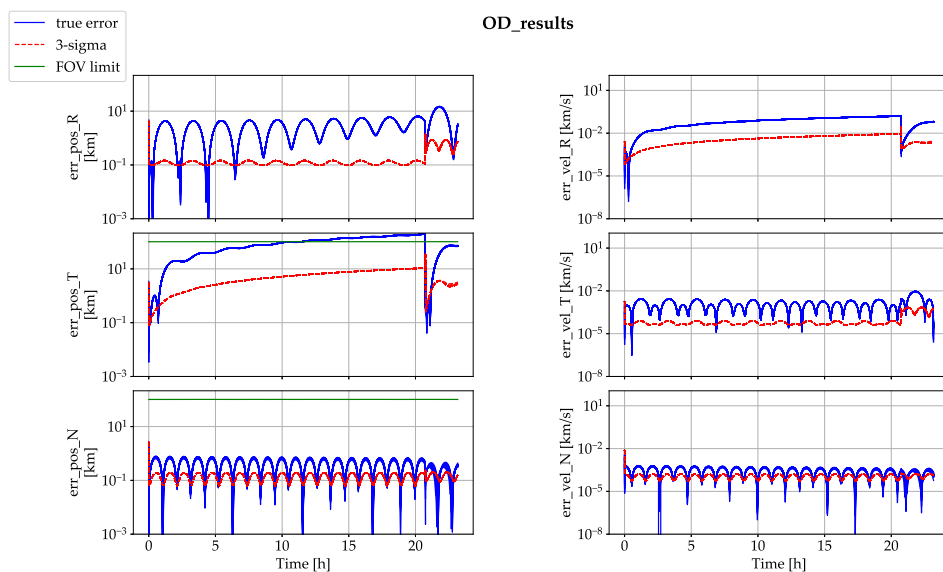
FIGURE 4.18: Estimated covariance and residuals to orbit reference after heuristic IOD using a 100 elements MC distribution (object: 25853).

unpredictability of the pointing direction. However, the VD algorithm managed to schedule an efficient observation plan and the object has been observed anyway, as visible from the covariance drops after 20 hours of propagation. A second observation of the object, and eventually more than one, may allow a better estimation of its orbit and a correct creation of an instance inside a catalogue, in order to be able to keep following and schedule the observation of that target. The VD scheduler, so implemented, has been validated to correctly follow-up an object which first estimation has been proven to be faulty. The hIOD extension to the algorithm allows an additional gain in terms of computational tractability of the overall system. In fact, the simulations show an overall 50% reduction (optimal cases showed up to 98.7%) of VD solutions that need to be propagated and followed-up. The result is a more efficient scheduling routine with less saturation of unnecessary observation tasks to be respected by the sensors. Such a good gain in terms of less VD solutions to be followed up, allowed a complete re-observation of short arcs tracklets even with one single observer configuration as the case presented in Fig.s 4.18 and 4.19 even after the following night. Additionally, a reduction of the virtual points to be propagated and scheduled allows more efficient scheduling techniques as the greedy-method, that has been also used as tasking tool for those two examples.
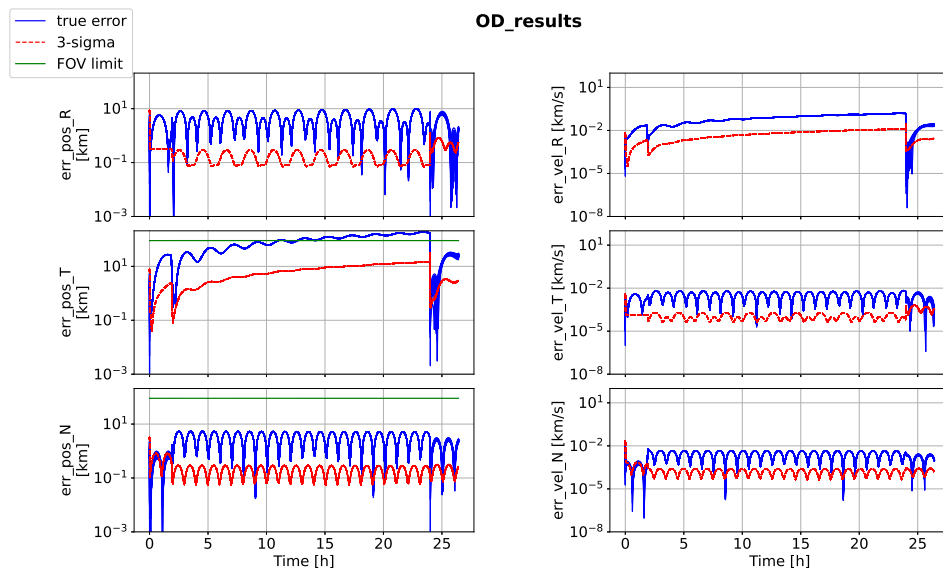
Figure 4.19: Estimated covariance and residuals to orbit reference after heuristic IOD using a 100 elements MC distribution 25678.

The context in which the Thesis took place has been reported in Appendix 7.1. This chapter will present the high-level functionalities of the SPOOK software suite and their importance for the SST pipeline, together with new developments introduced by this thesis that have not been presented so far.

5.1 Airbus SST

The SPOOK is a versatile software suite developed at Airbus, with the aim to support SST activities. The core characteristics of SPOOK were introduced on 2019 [13] and recently updated by the author in 2021 [36], to extend to the new developments. This section is going to present a short overview of the functionalities that are currently available, and that have been widely used during this Thesis work. As represented in Fig. 5.1, SPOOK provides the complete set of tools necessary for the SST cataloguing pipeline; these are tracklet linking of measurements, correlation with internal or external catalogues (e.g. Space-Track GP catalogue), IOD and OD. Additionally, SPOOK can simulate realistic radar and optical measurements and export them in several standard formats. Ideally, from the optical images on top, photometric and astrometric analysis are obtained. Those information are used inside dedicated filter to obtain object information, both in terms of object state vector and characteristics (e.g. attitude, shape, material, etc.). Those information are used inside scheduling tool to create personalized observation plans that are finally performed by ART. Furthermore, SPOOK has been upgraded with the capability to create different types of observation plan that can be used to task an arbitrary sensor. These include geostationary belt surveys, coverage-optimized tracking strategies for all classes of objects, including celestial bodies and known artificial objects (e.g. GPS), and calibration scenarios. Consequently, SPOOK is now able to create observation plans autonomously or based on specific user requests. Once observations have been performed, it can process the obtained images through external or internal tools in order to extract relevant features (astrometric and photometric quantities). Finally, other relevant SPOOK upgrades have been
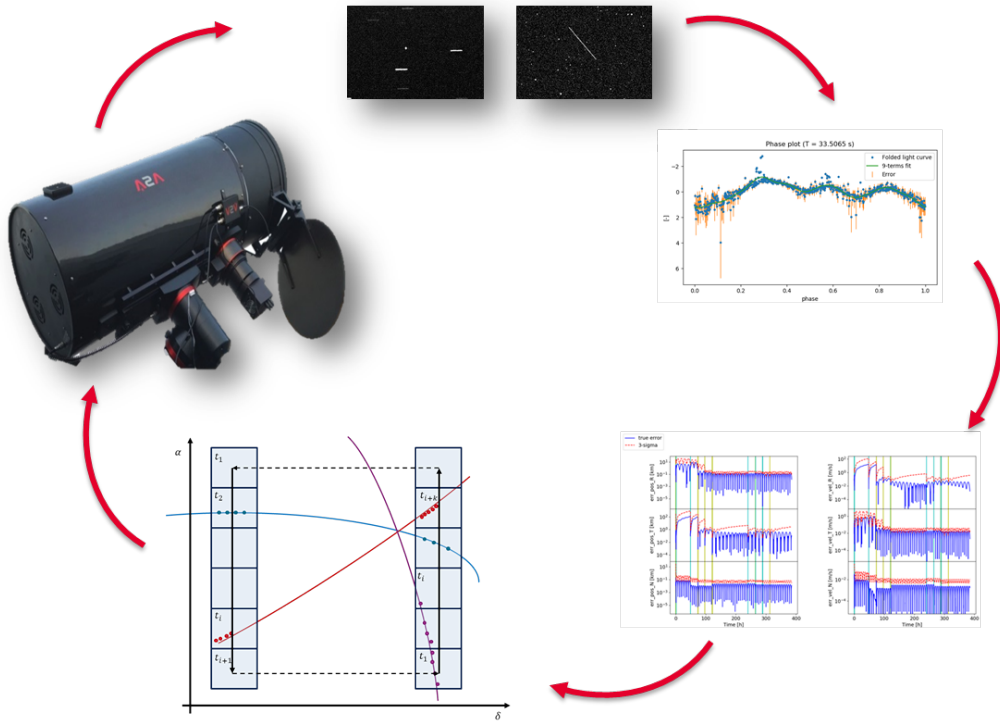
FIGURE 5.1: Representation of the E2E capabilities made possible by the activity of ART and SPOOK.

implemented; namely photometric analysis of optical measurements, manoeuvrer simulation capabilities, conjunction analysis and visualization of the results through plots, tables and animations. With the ART, which was deployed in June 2018, SPOOK has become an E2E prototype of a ground-based SST data centre.

Airbus acknowledges SSA as key to ensure Space Safety and Sustainability. Both software tool SPOOK and ART sensor aim to better understand the challenges of an increasingly congested space environment, thanks to real-world sensor's data and enhanced data processing capabilities. As presented by the author in [36], is provided a list of the possible capabilities that this framework allows:

- First, SPOOK can perform IOD/OD and state vector/covariance propagation with multiple different algorithms available (e.g. batch estimator, Kalmann's filters, augmented Gaussian Mixtures extensions, etc.).

- Moreover, it can perform sensor network simulation, including optical telescopes and radars which can be placed either in space or on ground. With this, the coverage of specific observation scenarios can be explored and simulated measurements can be generated.

- Light curves can be generated from optical observation data and analysed for object characterization tasks.

- SPOOK includes the complete pipeline to perform end-to-end space object catalogue creation and maintenance; i.e. tracklet linking, correlation and orbit determination as shown in Fig. 5.2.

- Observation planning complements the cataloguing tools; SPOOK can create sensor pointing profiles to perform both tracking of known objects and survey of specific regions.

- Above core modules of SPOOK can be used to astrometically calibrate SST sensors using GPS or ISLR objects as reference.

- Last but not least, a conjunction assessment module is available, as presented in section 4.2.2.4.

- SPOOK is used to task ART and to process its data; Airbus' own ground-based SST sensor located in Spain and contributing to SMARTnet.

SPOOK is continuously developed further via PhD and Master Theses, as well as internal research.

5.2 SPOOK tool - the Cataloguer

The software SPOOK has been developed over the years to comprehend most of the tools necessary for SST and, in particular, for space debris cataloguing. As presented by the author in [36], a catalogue has been deployed during the time of this Thesis project having as support the cookbook of tools of the aforementioned software. The cataloguer baseline, already developed by previous Phd Student in the software suite, has been deployed in July 2021, after a few rounds of tests in the previous months. The cataloguing tool can be represented by the block chart in Fig. 5.2. On the top of the image is represented the Catalogue of objects and the sensors participating in the network. Between them are visualized, inside a green scope, the Observation Planning routines that have been introduced during this thesis. Closing the chain, are visualized the main blocks of the post-processing activities of the images. This set of tools involves: the tracklet-linking techniques, the correlation of measurements, IOD and OD. These tools are necessary to extract space debris information out of measurements. On that block diagram is visualized inside a green scope the extension of the cataloguing chain introduced with this new thesis. The observation planning routines operate either in CM or CG mode, depending on the user settings. As CM techniques a greedy-method has been adopted as well suitable for small catalogues scheduling. The CG routines instead have been based on the GEO fence survey mode. The planning can be anyway customized depending on the user needs. As for ART observations, the following schedule has been respected:

1. tracking of light curve of interest;

2. GPS calibration tasks;

3. star fields for photometric calibration;

4. full light curve list for tracking;
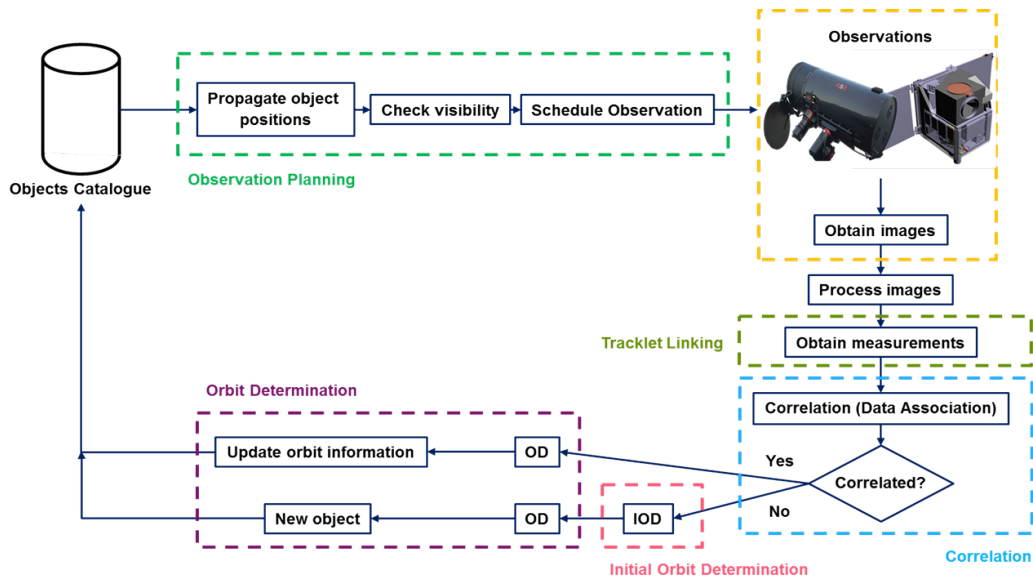
Figure 5.2: Cataloguer block diagram.

5. GEO fence plan;

6. GEO tracking.

As visible, there are additional tasks that are necessary for cataloguing purposes that are not directly covered in the previous sections. This is the case of the calibration tasks, that are important for determining the accuracy of the sensors. This accuracy is a value of high importance for the post-processing tasks of correlation and OD, since it indicates how good the new measurements can be trusted.

5.2.1   Planner GUI

To support complementary the cataloguing operations, or for general simulation of the available observation strategies, a GUI based user interface has been released inside SPOOK. Few captions of the new tool are given in Fig. 5.3 and Fig. 5.4. The GUI allows the user to set up the observation scenario in terms of observer design and catalogue of objects to be maintained. Given the observation scenario, the user is able to visualize the accessibility intervals of the selected objects and can build up a proper observation plan using different type of optimization and scheduling options, e.g. greedy method based optimization. The user is able also to visualize the observation profile as observer's FOV at a specific range from the observer.

5.2.2   Image Simulation GUI

To complete the range of simulation scenarios obtainable with SPOOK a tool for synthetic image generation is present. The tool has been developed as support for the simulations of the auto-tracker observation strategy presented in sec.4.2.1.1. The validation of the tool required, in fact, the possibility to autonomously generate
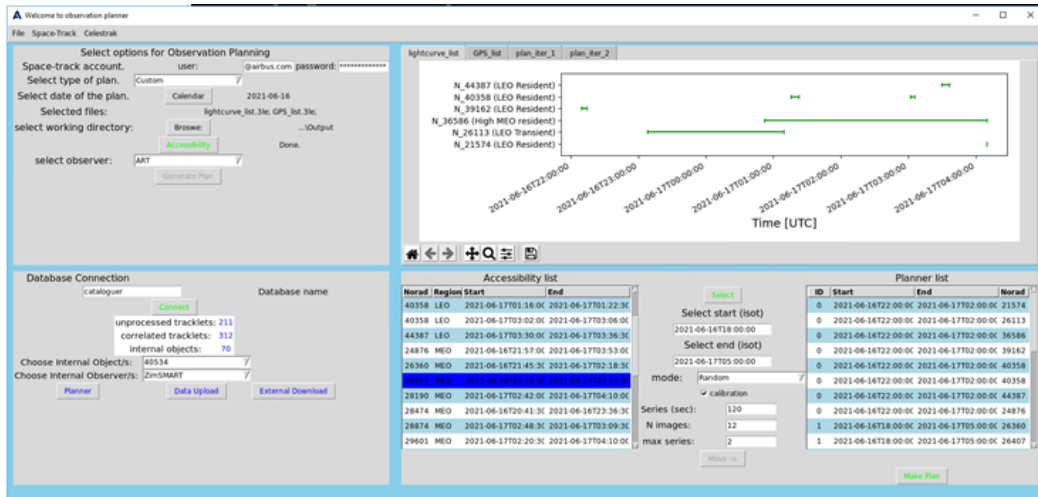
FIGURE 5.3: SPOOK GUI accessibility study.
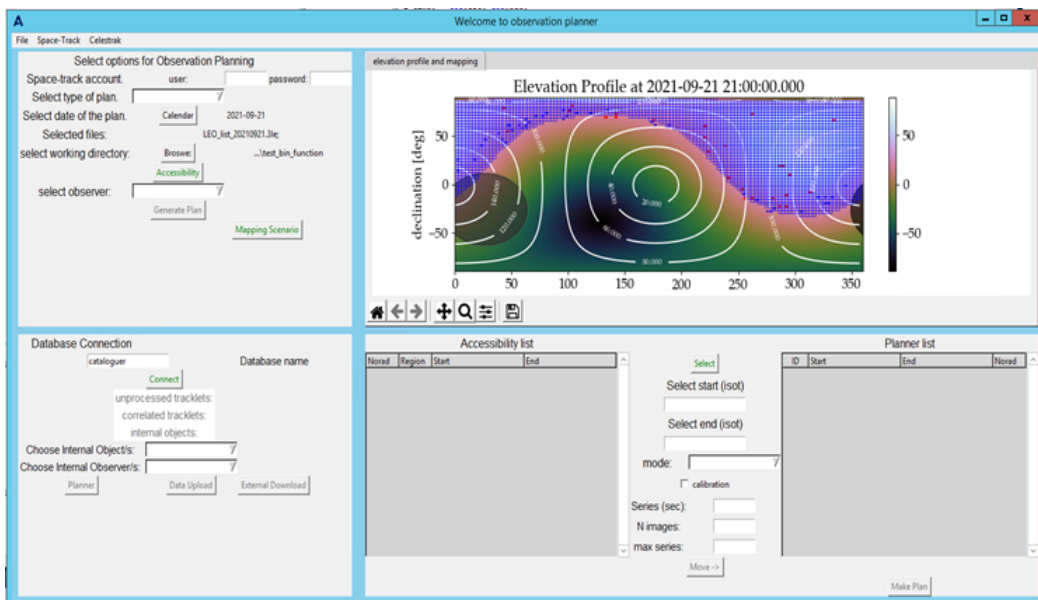
FIGURE 5.4: SPOOK GUI mapping analysis.
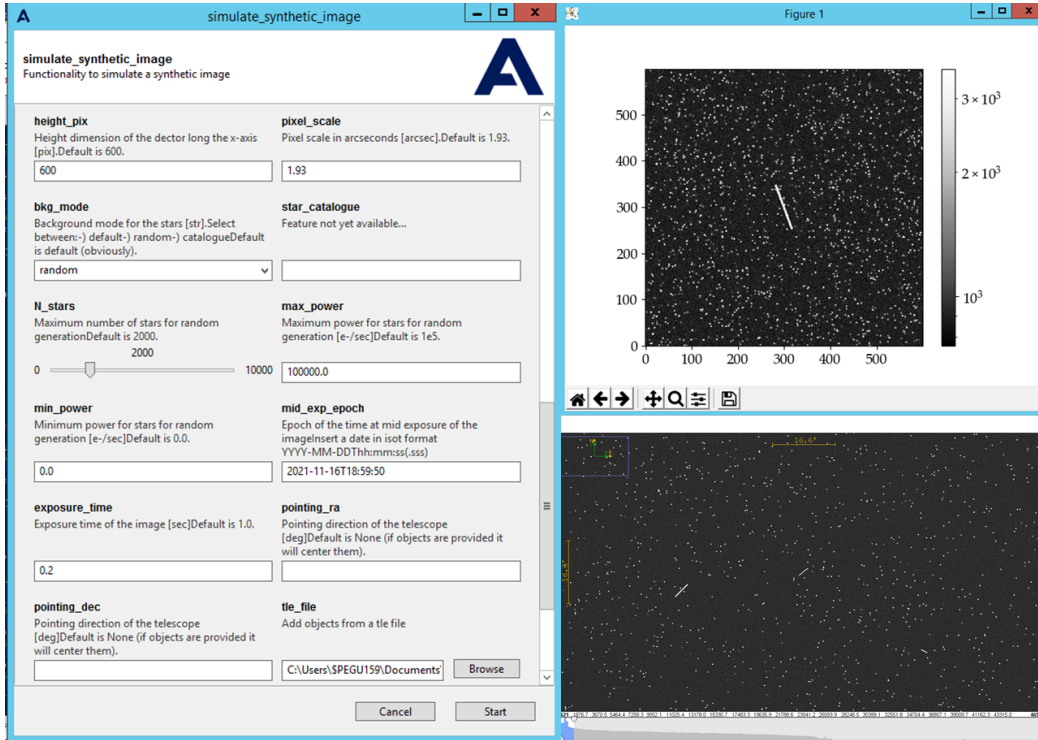
Figure 5.5: Image Simulation GUI.

images with different level of background and cluster noise, to test the patter-matching routines at best. An example of the related image simulation GUI is shown in Fig. 5.5. the image simulation tool made use of an already available instrument to generate optical synthetic images given specific value of signal electron power and noise. The instrument has been extended to simulate those input values from object propagation using the ART optical performance model and SPOOK propagator.

This final chapter comprehends the main direct operational results connected with the work presented in the previous chapters, thanks to their integration into the software suite SPOOK. The main results for each use case will be presented and discussed. Additionally, further development will be presented.

In Fig. 6.1 are visualised some examples of information and services that can eventually be obtained with the data present inside a catalogue. The Data necessary to build a catalogue are on the top of the graph. They represent the user's questions that can be directly answered with the information contained in a catalogue. On the bottom are listed the services that can be obtained processing those data. Information that can directly be extracted from the data present inside a catalogue are paramount to answer some civil and governmental user questions: where are the objects? What these objects can do? Is this object active or uncontrolled?
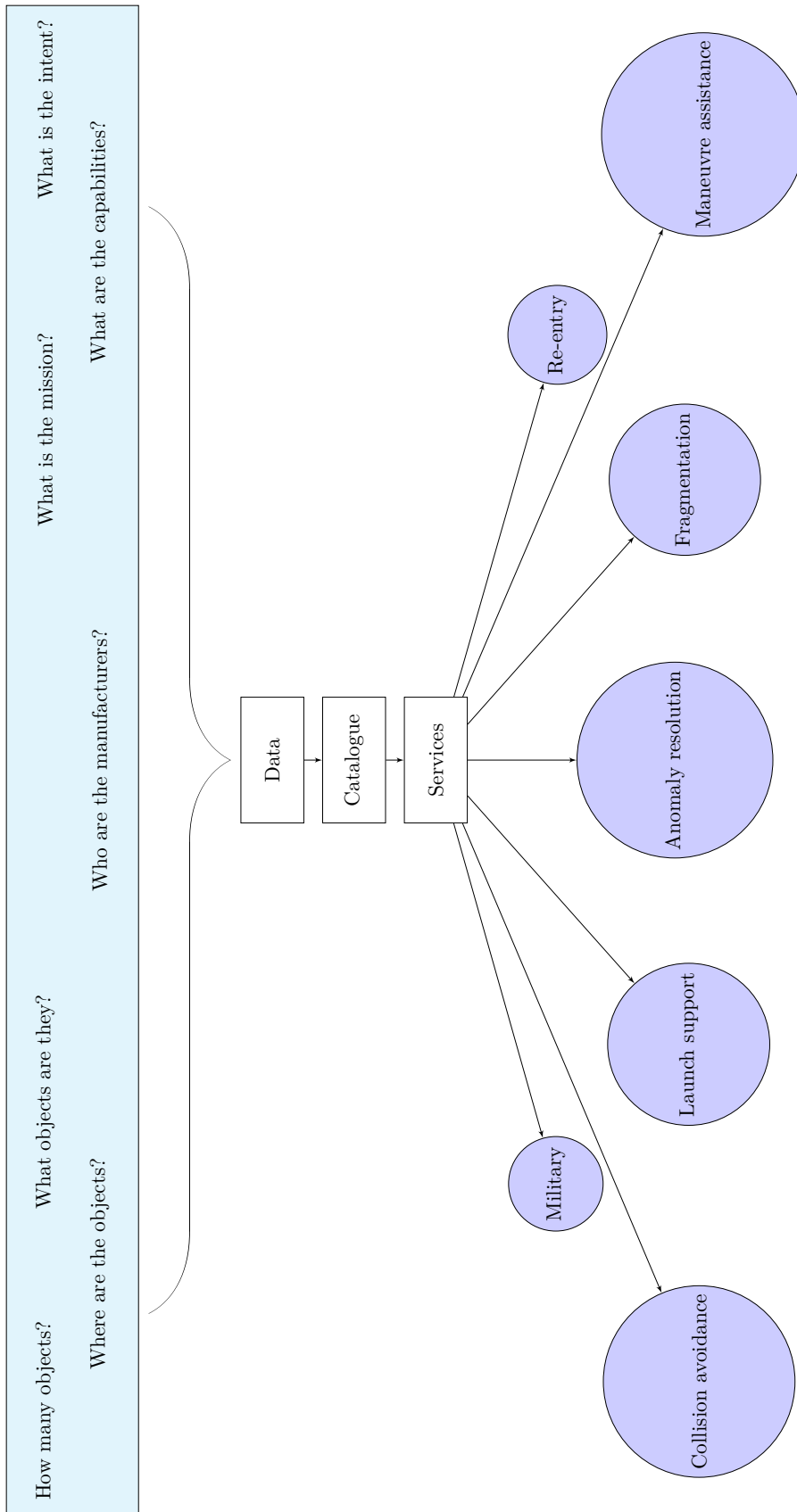
Figure 6.1: General use cases roadmap connected with the cataloguing problem.

Of higher interest, are anyway, the services that can be obtained from the data of a catalogue. Processing the orbital and attitude information of the objects collected in a catalogue it is possible to:

- perform collision avoidance: the use of special perturbations orbital propagators is the basis for a precise conjunctions assessment capability. A fast alert in providing warning for close conjunctions between objects in space, and control techniques to manoeuvre a spacecraft reducing its risk of collision is of key relevance for the space safety and sustainability.

- Support to Launch and early phases of a mission: *Launch and Early OPerations* (LEOP) and *Collision On Launch Assessment* (COLA).

- Monitor uncontrollable collision by the use of precise Fragmentation models and surveillance observation modes.

- Support during re-entry events: warning and observation support.

- Provide assistance to operations: assistance to special on-orbit operations (e.g. *Active Debris Removal* (ADR)).

This chapter will investigate into more details only few of these possible use cases. For example the fragmentation problem in sec. 6.3.1, as has been studied by the author in [38], will be reported and expanded.
Additionally this chapter will report the work done in Airbus Defence and Space for the deployment of an operative catalogue of space objects in sec. 6.3.

Differently from the above mentioned use cases, that were exploiting the functionalities of a catalogue, this chapter is also going to present some other scenarios in which an ad-hoc sensor scheduling capabilities can be used. This is the case of sec. 6.1 and 6.2, where dedicated mapping survey strategies have been used to study the detectability of population of objects (e.g. the GEO region).
Finally, sec. 6.4 will present a special observation mode, known as *stare-and-chase* scenario, that is of great interest for the live detection of unknown objects.

6.1 Space-Based Study

The strength of in-space observations is quite a hot topic for the SSA community nowadays. From space, some of the most constraining barriers for object observation (e.g. the atmosphere, the Sun light diffusion, etc.) are removed. As expected, much more objects can be observed and detected, and optical devices become even more relevant for this scope. A much bigger population of objects can be observed, expanding the catalogues also to smaller dimension debris, even below the centimetre size. Some of the tools developed within the Thesis allow to generate pointing profiles also for space-based observers and to study the object's coverage and detectability. However, space-based observations can have, on their own, observability constraints dictated by reduced slewing capabilities or attitude specifications imposed by the type of mission.

A type of orbit that may allow a continuous coverage of the objects should be able to point continuously in the anti-Sun direction. In this case, the observations may reach the optimal performance by reducing to the minimum the Sun light noise and reducing the phase angle of the observed objects. An orbit of such a type is the Sun-synchronous orbit.

A case study is going to be presented within this section exactly for this kind of mission, considering the observer on a LEO and Sun-synchronous orbit, with a plane close to the termination plane. The altitude of the orbit has been set to 750 km and the inclination to 98°. The control of the pointing vector can be considered of three main types: completely unconstrained, partially constrained by the platform, or completely fixed. The first case is to be understood as a mission in which the observing telescope is the main payload on board. In such a scenario the telescope may be capable of a totally free steering capacity. The constraints, in this case, are only dictated by the exclusion zone of the Sun, the Earth's limb, and the platform constraints.

The second case can be seen as a scenario in which the telescope is not the first payload on board the spacecraft and maybe some attitude modes need to be respected, i.e. the nadir pointing to the Earth in an Earth's observation mission for example. In this case, the observer may be allowed to steer around its roll axis to sweep more area with its field of view.

The last, and most constraining case, is the case of a telescope completely fixed to the platform, in this case, the pointing direction is fixed to a certain direction in the anti-Sun direction.

All of these scenarios are going to be analysed within this section. In Fig. 6.2 it is schematized the orbital plane of the observer in the LEO orbit. It is shown with some red arrows the possible pointing directions that lay in the plane perpendicular to the orbit. The red arrows show different pointing direction of the observer, or *Line Of Sight* (LOS), when the only allowed movement is on the roll angle (around the flight direction axis) in xy plane. The control of the pointing vector can be ideally represented by the roll angle of the spacecraft. Looking at Fig. 6.3, the LOS lays on the plane perpendicular to the flight direction. It is free to rotate around the axis described by the direction of flight $\boldsymbol{v}$. In Fig. 6.3, the $\boldsymbol{r}$ vector shows the position of the observer from the Earth centre, the $\boldsymbol{v}$ direction shows the flight direction and the $\boldsymbol{n}$ vector (out of plane of the page) is the normal direction. The plane created by the vectors $\boldsymbol{r}$ and $\boldsymbol{n}$ is the plane where the pointing vector lays. Knowing the flight direction $\boldsymbol{v}$ and the position of the observer $\boldsymbol{r}$, the perpendicular direction to the orbital plane $\boldsymbol{n}$ can be found by Eq. 6.1

$$\boldsymbol{n} = \frac{\boldsymbol{r}}{|\boldsymbol{r}|} \times \frac{\boldsymbol{v}}{|\boldsymbol{v}|} \tag{6.1}$$

The LOS can be represented by the vector $\boldsymbol{n}$ rotated around the axis $\boldsymbol{v}$ by an angle α. In case of partial control of the LOS around the roll axis, the control angle α can be represented as function of the time $\alpha = \alpha(t)$. In case of no-control, the LOS is fixed to the observer platform and the control angle is constant $\alpha = \alpha_0$. The LOS
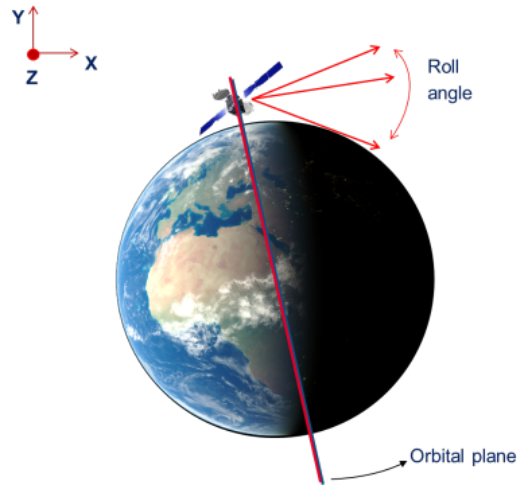
FIGURE 6.2: Example of an observer orbit on a LEO high-inclined orbit, on a plane perpendicular to the orbit itself.
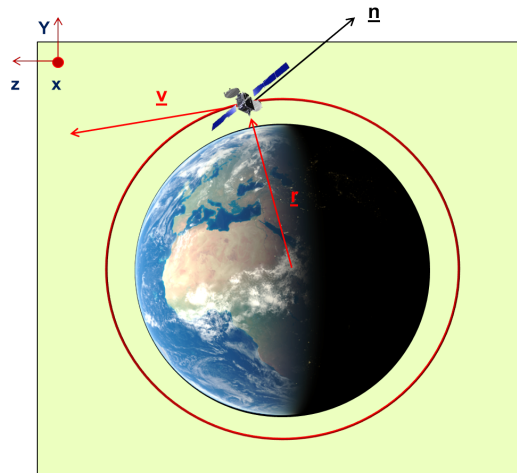
FIGURE 6.3: Example of an observer orbit on a LEO high-inclined orbit, as seen from a the orbital plane.

can be so estimated:

$$\boldsymbol{LOS} = \boldsymbol{R} \begin{bmatrix} 1 & 0 & 0 \\ 0 & \cos\alpha & -\sin\alpha \\ 0 & \sin\alpha & \cos\alpha \end{bmatrix} \boldsymbol{R} \qquad (6.2)$$

Where $\boldsymbol{R}$ is the orthonormal basis described by the vector $\boldsymbol{v}$. A visualization of the pointing profile of such an observer is schematized in the geocentric plane in Fig. 6.4. In this case can be easily identified the anti-Sun direction of the LOS, built-up thanks to a Sun-synchronous orbit at the terminator plane. The observer is efficiently pointing opposite to the Sun light and observing objects highly illuminated by the Sun itself. A representation of the pointing profile pattern is also proposed
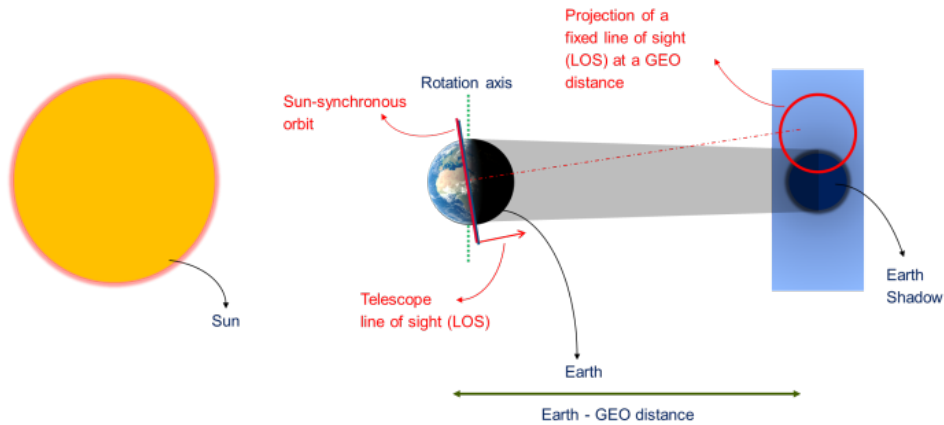
FIGURE 6.4: Visual representation of the pointing profile generated by an observer with LOS perpendicular to its orbit.

at a GEO distance from the Earth. The representation of this pointing profile directly in the right ascension and declination plane with corrected proportion is visualized in Fig. 6.5. In this case it is visible also the correct distribution of the objects in the GEO belt. It is visible in black the shadow of the Earth and in green is visualized the pattern of the LOS's FOV. In case of pure passive pointing, the telescope is fixed to the platform, the pattern of the FOV will remain always the same as presented in Fig. 6.5. In Fig. 6.5 is visible the pointing profile (in green) generated by a space-based observer, placed on a sun-synchronous orbit, with LOS direction perpendicular to its orbit. In blue is highlighted the position of the objects on the GEO belt and in Black the Earth shadow. The LOS of the observer will sweep always the same area of the right ascension and declination plane. during its motions the objects will move in their orbits following the Earth rotation and are eventually observed by the observer when falling inside the ring created by the pointing profile pattern. The case in which the pointing angle can be controlled by means of the control angle $\alpha = \alpha(t)$, different area of the right ascension and declination plane can be swept. This is the case shown in Fig. 6.6. The image shows the pointing profile (in green) generated by a space-based observer, placed on a sun-synchronous orbit, with LOS variable on its roll angle. The control low of the pointing angle is described via a sinusoidal function. The image is a capture of the animation visualization tool of SPOOK. In this case the control angle has been considered as a sinusoidal function:

$$\alpha(t) = A \sin(\omega t) + b \tag{6.3}$$

where A is the amplitude, ω the frequency and b is the mean value. In this case it is possible to see that the FOV is covering more area, observing regions at higher inclinations. In tab. 6.1 are reported the results of a simulation of a space-based observation of a representative population of the GEO belt (obtained from space-track) over 7 days. The simulation represents the case of partial active control with sinusoidal control law as in Eq. 6.3. In this simulation case the amplitude A of the angle control law has been considered equal to 20°, $b = 15°$, constraining the control
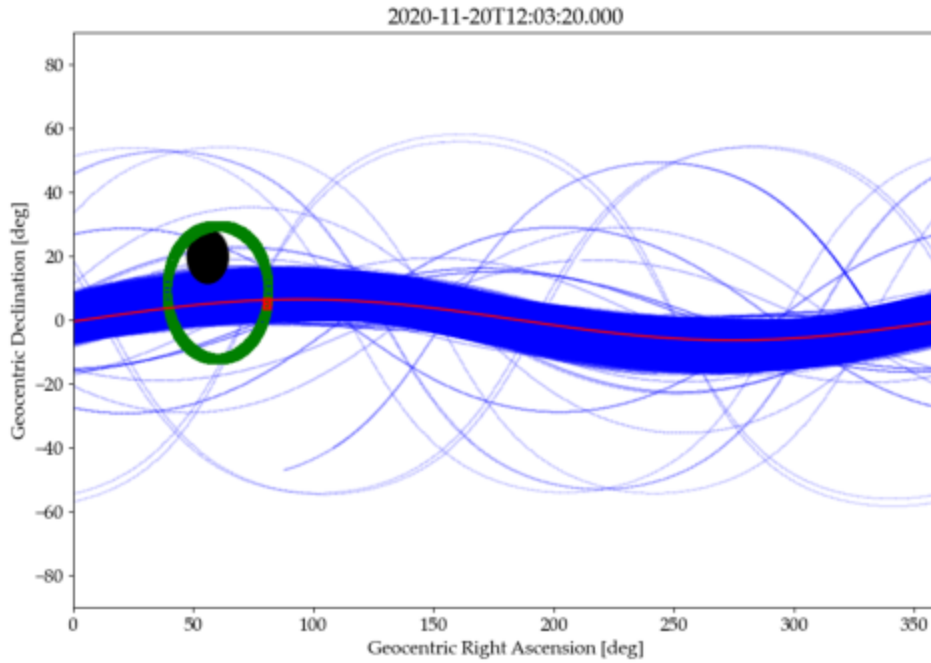
FIGURE 6.5: Pointing profile generated by a space-based observer.
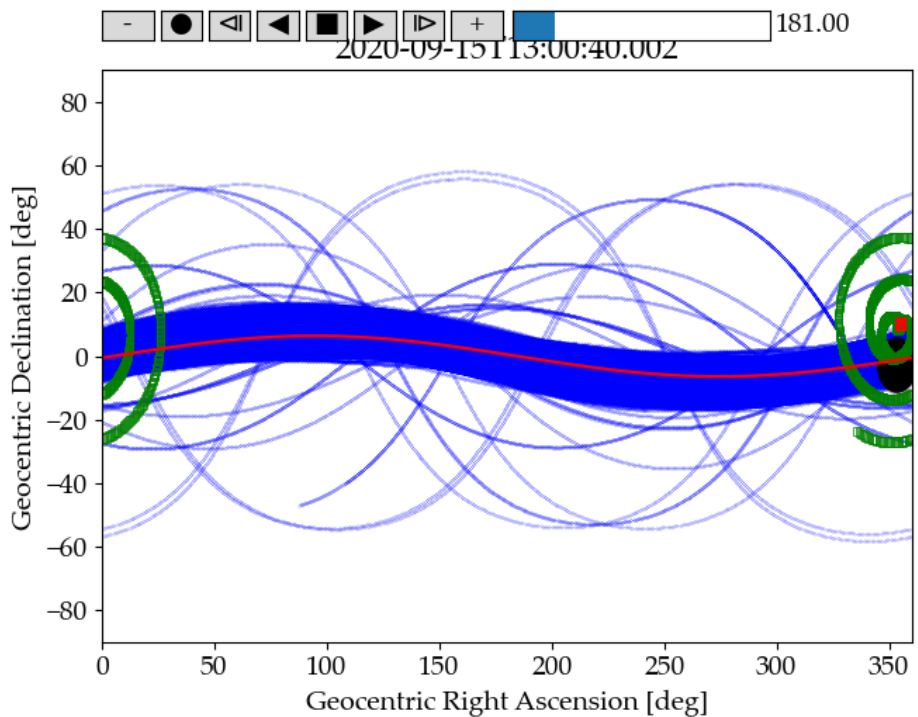
FIGURE 6.6: Pointing profile generated by a space-based observer, with LOS variable on its roll angle.

Table 6.1: Statistics summary of space-based observer in Sun-synchronous orbit with constrained sinusoidal pointing over a simulation of 7 days:

Orbital Region	Detected	Undetected	Total	mean revisit frequency [days]
High MEO transient	1 (100%)	0 (0%)	1	0.4286
GEO resident, $0° \leq i \leq 20°$	1125 (79.11%)	297 (20.89%)	1422	0.2615
GEO resident, $i > 20°$	10 (47.62%)	11 (52.38%)	21	0.2286
GEO transient	32 (96.97%)	1 (3.03%)	33	0.2634
Total	1168 (79.08%)	309 (20.92%)	1477	0.2614
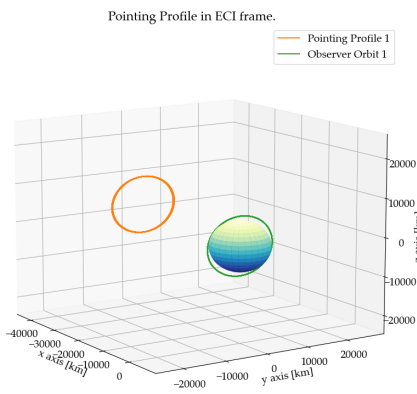
FIGURE 6.7: Visualization (in orange) of the observer pointing profile along one orbit at a GEO distance from Earth. in green is visible also the LEO orbit of the observer.
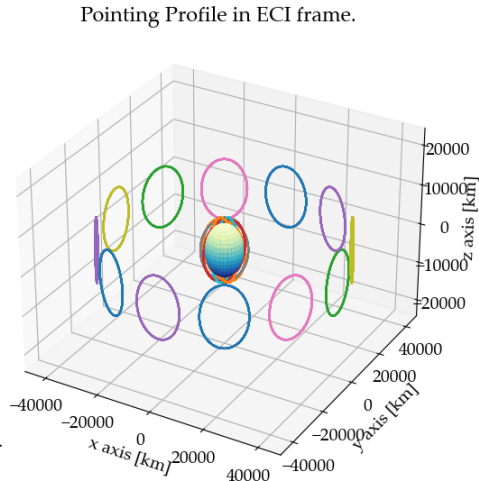
FIGURE 6.8: Visualization of the pointing profiles of a network of 12 sensors with the same characteristics described in Fig. 6.7.

angle between 35° and −5°. Even this configuration, is not optimal and the total coverage of the sample population of GEO objects is around the 75%. The revisit rate is however very high, and it can be a good requirement for cataloguing purposes. Such an observer-pointing configuration is depicted in Fig. 6.7, where it is visible the LEO orbit highly inclined and the pointing profile at a GEO distance from Earth. In Fig. 6.8 are instead presented the orbital configuration of a network of 12 sensors with the same characteristic of the previous one, to increase the pointing coverage. However, the coverage and detection performances can be analysed by a deeper level, taking into account the relative angular velocity between the sensor and the objects and the apparent brightness, or magnitude. This analysis allows to separate the simulation scenario to the optical analysis of detection. In fact, one thing are the illuminated crossing of objects inside the observer's FOV, another thing is the detection capability of the telescope. To uncouple this relation, it is interesting to visualize the crossings of the objects inside the FOV with respect to their angular velocities and brightness. Both of these quality are decoupled from the type of instrument is on-board and can be used as trade-off method for the selection of the optical system itself.
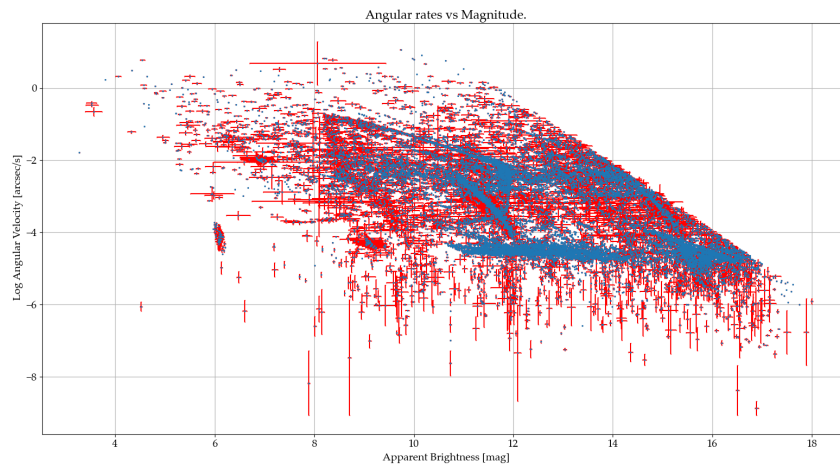
FIGURE 6.9: Visualization of the crossing statistics for a space-based observer study.
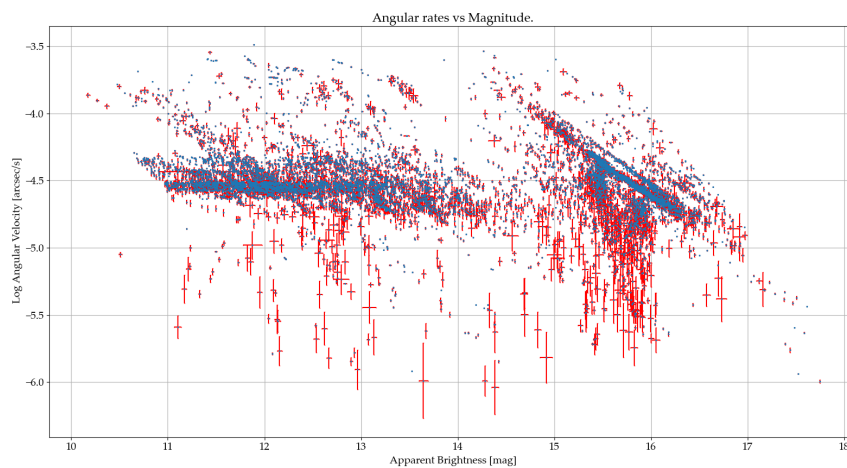
FIGURE 6.10: With reference to Fig. 6.9, this visualization shows only the sub-population of GEO objects (lower part of the first graph).
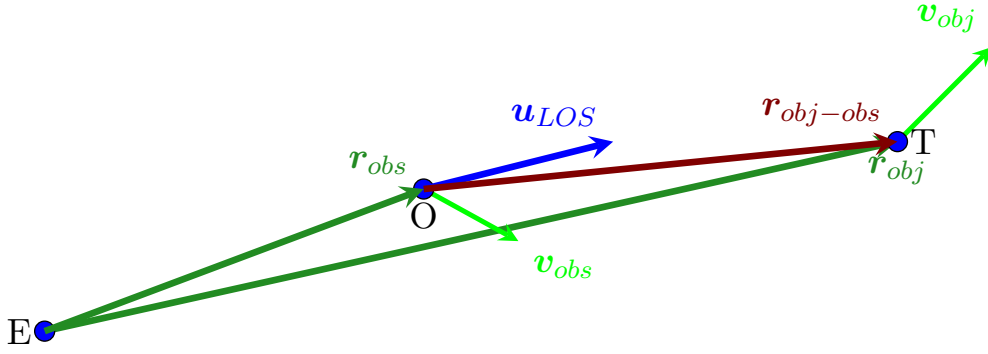
FIGURE 6.11: 2D simplification of the Earth-Observer and Target geometry in order to identify the relative velocity between the observer and the target.

The apparent magnitude depends on the amount of light scattered by the object to the observer and it is function of the observation geometry: phase angle, dimension of the object and distance to the observer. The relative angular velocity is the relative velocity of the object as it appears in the FOV. With reference to Fig. 6.11, the relative angular velocity can be evaluated starting from the object position $\boldsymbol{r}_{obj}$ and velocity $\boldsymbol{v}_{obj}$, and the observer's $\boldsymbol{r}_{obs}$ and $\boldsymbol{v}_{obs}$. In Fig. 6.11, in dark green are shown the position vectors, in light green their velocity. In blue is the pointing vector.

The LOS itself may have an angular velocity on its own, relative to the observer-fixed reference frame:

$$\boldsymbol{LOS} = \begin{bmatrix} \alpha_{LOS} & \delta_{LOS} \end{bmatrix} \; and \; \boldsymbol{\dot{LOS}} \begin{bmatrix} \dot{\alpha}_{LOS} & \dot{\delta}_{LOS} \end{bmatrix} \tag{6.4}$$

The LOS direction can be use to compute the pointing vector $\boldsymbol{u}_{LOS}$:

$$\boldsymbol{u}_{LOS} = \begin{bmatrix} \cos\delta_{LOS}\cos\alpha_{LOS} \\ \cos\delta_{LOS}\sin\alpha_{LOS} \\ \sin\delta_{LOS} \end{bmatrix} \tag{6.5}$$

And its first derivative:

$$\boldsymbol{\dot{u}}_{LOS} = \begin{bmatrix} -\sin\delta_{LOS}\cos\alpha_{LOS}\dot{\delta}_{LOS} - \cos\delta_{LOS}\sin\alpha_{LOS}\dot{\alpha}_{LOS} \\ -\sin\delta_{LOS}\sin\alpha_{LOS}\dot{\delta}_{LOS} + \cos\delta_{LOS}\cos\alpha_{LOS}\dot{\alpha}_{LOS} \\ \cos\delta_{LOS}\dot{\delta}_{LOS} \end{bmatrix} \tag{6.6}$$

At this point, it is possible to evaluate the pointing vector to the object $\boldsymbol{r}_{ptg}$, assuming the pointing and the object have a small angular distance and are very far part. The latter is quite a relaxed assumption for these kind of optical observations, where the FOV is very small and the average distance between observer and objects is above 1000 km. For first thing, the distance ρ from the observer to the object can be defined in the following way:

$$\boldsymbol{r}_{obj-obs} = \boldsymbol{r}_{obj} - \boldsymbol{r}_{obs}, \; \rho = \|\boldsymbol{r}_{obj-obs}\| \tag{6.7}$$

The pointing vector and its derivative can be so defined:

$$\boldsymbol{r}_{ptg} = \boldsymbol{u}_{LOS}\rho, \ \dot{\boldsymbol{r}}_{ptg} = \frac{\partial \boldsymbol{u}_{LOS}}{\partial t}\rho + \frac{\partial \rho}{\partial t}\boldsymbol{u}_{LOS} \tag{6.8}$$

Where:

$$\frac{\partial \boldsymbol{u}_{LOS}}{\partial t} = \dot{\boldsymbol{u}}_{LOS}, \ and \ \frac{\partial \rho}{\partial t} = \frac{\partial \|\boldsymbol{r}_{obj-obs}\|}{\partial t} \tag{6.9}$$

It can be easily shown that:

$$\frac{\partial \|\boldsymbol{r}_{obj-obs}\|}{\partial t} = \frac{\partial \left(\boldsymbol{r}_{obj-obs} \cdot \boldsymbol{r}_{obj-obs}\right)}{\partial t} = 2\left(\frac{\partial \boldsymbol{r}_{obj-obs}}{\partial t}\right) \cdot \boldsymbol{r}_{obj-obs} =$$
$$= 2\left(\boldsymbol{v}_{obj} - \boldsymbol{v}_{obs}\right) \cdot \boldsymbol{r}_{obj-obs} \tag{6.10}$$

the geocentric pointing velocity can be so evaluated:

$$\boldsymbol{v}_{ptg} = \boldsymbol{v}_{obs} + \dot{\boldsymbol{r}}_{ptg} \tag{6.11}$$

Which leads to the relative angular velocity ω, using the vectorial product:

$$\omega = \frac{\|\boldsymbol{r}_{obj-obs} \times \boldsymbol{v}_{obj} - \boldsymbol{v}_{ptg}\|}{\rho^2} \tag{6.12}$$

A graphical representation of the angular rate of the objects crossing the FOV in function of the magnitude is proposed in Fig. 6.9. The graph is in the logarithm angular rate vs brightness plane. The objects may changes sensibly their conditions during the crossing with the observer, this range of values has been represented with the vertical and horizontal bars. As visible the crossings are concentrated on some *islands* which represent some sub-populations of the objects. The upper part of the graph, with higher angular rates, are populated by LEO objects, while the lower parts by more distant objects. This example has been obtained considering a 2 days simulation in a single observation scenario. As reference population, it has been considered instead the full space-track catalogue. The observer has been considered to be free to move with respect to the platform and the only constraints considered have been of geometrical type. The optimization of the observation has been obtained via the space-based dedicated mapping method, as presented in 4.2.2.2.

The mapping method has been set to be optimized for distance from Earth's limb and geometrical distance from the Sun (angle between the Sun, the object and the pointing direction). An example of this scenario is represented in Fig. 6.12, where the white contour lines represent the angular distance from the Sun of the pointing vector. The circular darker *halo* is the Earth's shadow. The color background express the Earth's limb distance at this instant of time. The reference system is the body local *Geocentric Celestial Reference Frame* (GCRF). Fig. 6.9 shows the values of angular velocity and magnitude of the objects crossing the FOV during that simulation. The red bar reports additionally the variation of those values during the crossing period. This type of graph can be quite helpful as preliminary study before the selection of an optical device that better allows detection. It is important, in fact, to take in mind that the detection is function of the *Signal to Noise Ratio* (SNR).
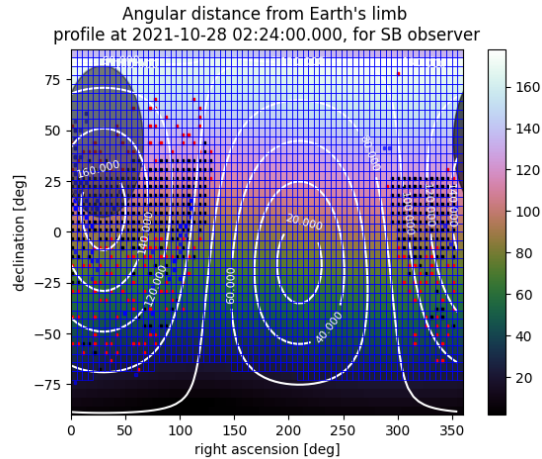
FIGURE 6.12: Capture of the SPOOK's visualization tool of the mapping optimization constraints at a specific instant of time during the simulation scenario.

The SNR itself depends on how much light radiance arrives to the detector's pixel for that specific object allowing the detection of both objects that are very fast and very bright and objects that are slower and less brighter.

This behaviour can be understood also considering the orbital region of the objects. It is easy to imagine that GEO objects will appear at slower rates in the FOV than LEO. The lower part of the objects represented in Fig. 6.9 is populated by GEO objects. A look-up of this area is also proposed in Fig. 6.10.

6.2   GEO fence Study

With respect to what has been presented in sec.4.2.2.1, the GEO fence scenario, this section is going to explore some practical uses of this method both in simulations and real-word with the ART.

When performing real observations with ART several constraints need to be taken into account:

- the slewing time of the telescope;

- the mount flip when crossing the local horizon;

- the leak proof condition;

- the minimum amount of image obtainable per field and the read-out time.

That means, passing from simulated scenario to real-word observation scheduling the constraints to be taken into account are much more strict. The first bottle neck in real world observation with ground based telescope is the general slewing capability. The slewing capabilities of most of ground based telescopes is based on type of mount configuration: equatorial or azimuthal. In the case of ART an equatorial mount is supporting the optical device. This type of mount configuration
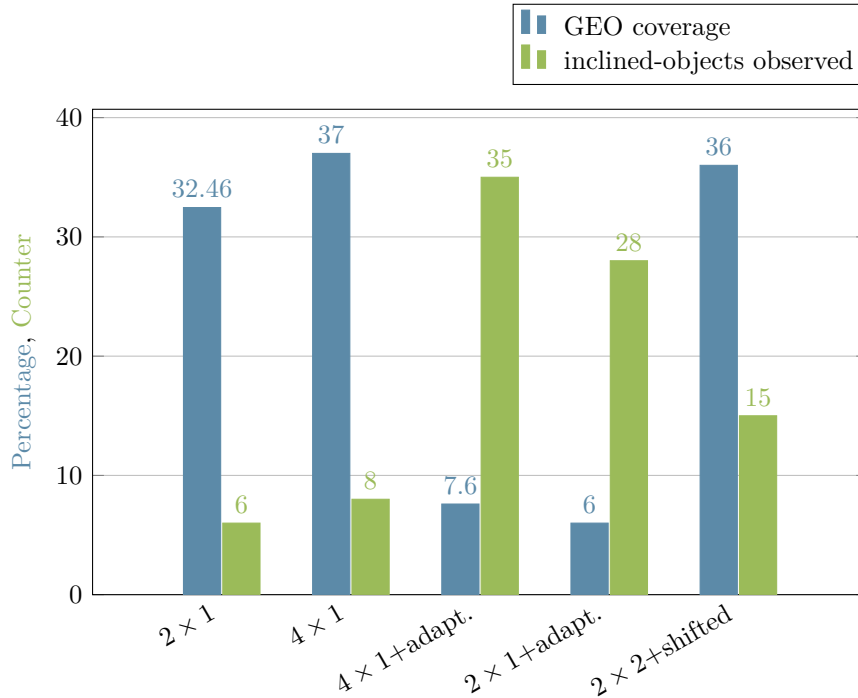
FIGURE 6.13: Visualization of the observation analysis results for the GEO fence survey mode for ART.

Table 6.2: GEO fence mode specifics:

Obs. Mode	Dec. Center	Accessibility	Stare Time	N. Images	Leak Proof	Revisit Ratio
2×1	0°	6-9 h	120 s	10	✓	60%
4×1	0°	6-9 h	96 s	8	✓	29%
4×1	adapt.	6-9 h	96 s	8	✓	0% (34%)
2×1	adapt.	6-9 h	120 s	10	✓	0%
2×2	±0.74°	6-9 h	96 s	8	✓	35%

has the generic constraint of inability to cross at high speed the local meridian of reference. Usually the south meridian at local azimuth 0°. To prevent interruption of observations during tracking the meridian should be considered as geometrical constraints, and observation cannot be performed if crossing it. In case of ART observation, a margin of 3° has been taken into account. In Fig. 6.13 are shown some of the results of observation statistics collected during the validation campaign of the GEO fence observation mode. In blue it is expressed the object coverage in relation to the total amount of objects visible in the GEO belt by a ground based sensor are ~ 462. In green it is reported the number of observed objects with inclination higher than 5°. The GEO fence configuration that seems to be best trade-off in terms of coverage and observation of inclined objects is the last one with 2 fences per 2 fields in shifted mode. The observation modes that have been taken into account are listed in Tab. 6.2. The number represented in the observation mode corresponds to the number of fences and fields: *number of fences × number of fields*. Adaptation

Table 6.3: Summary of the parameters utilized for the interpolation of the adaptation, or fitting, line of the GEO belt in GCRF:

Parameter	Value
A	$6.411\,27°$
ω	$1.001\,04\,\text{rad}^{-1}$
ϕ	$0.000\,44\,\text{rad}$
δ_0	$-4.849\,91°$
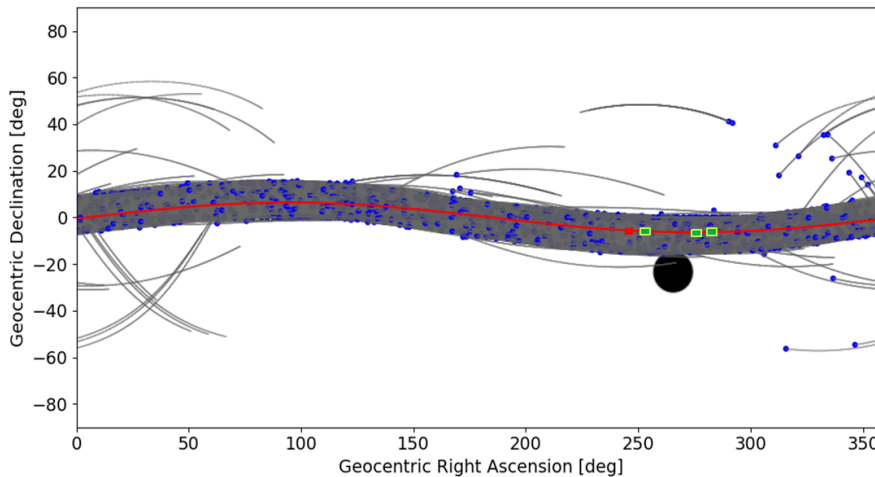
FIGURE 6.14: Visualization of the adaptation line of the GEO belt region.

means that the fences and fields are centred in the adaptation line of the GEO belt. A schematization of the GEO belt and the adaptation line in red is given in Fig. 6.14. The adaptation line has been generated fitting the averaged position of the GEO objects in one day propagation. The results of this fitting curve, in GCRF reference frame are given in Tab. 6.3.

The main goal of a GEO fence campaign is to scan the object belonging to the GEO belt. Since the objects at 0° declination, are mostly operative well-known satellite, the real interest of the survey relies in the observation of the objects with higher inclinations, where the presence of space debris is more possible. Cataloguing operations require multiple revisit of a single object during the night. Ideally, according to literature [11], a minimum of three expositions of an object in different orbital position shall be necessary to perform correctly IOD. The GEO fence mode, is based on strategic revisit of the object thanks to the symmetric disposition of the fences 30° apart. Such a configuration allows a 2 h revisit ratio with a single observer. However, a single sensor used for observation does not allow a good revisit in case of observation of the inclined objects. This can be easily visualized in Fig. 6.15, where some inclined objects have been highlighted to show their orbit (grey lines) in the time. As visible two symmetric fences does not allow the re-observation of the objects. Shifting the center of an observation fence in the direction of the center of the GEO belt, as represented in Fig.s 6.16 and 6.17, allows to have a great coverage
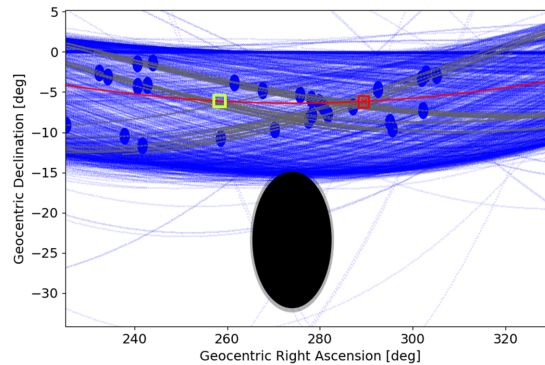
FIGURE 6.15: Close-up to the adaptation survey scenario in GEO fence mode.
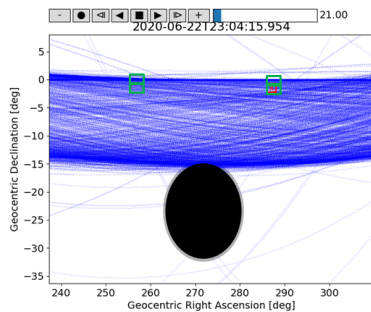
FIGURE 6.16: GEO fence survey mode in 0° declination shifted observation mode.
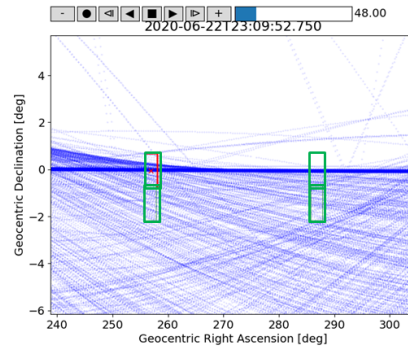
FIGURE 6.17: Close-up of the GEO fence observation mode in Fig. 6.16.

and revisit of the objects, and also detection of highly inclined objects.

6.3 Autonomous Cataloguer

In July 2021 a new version of the SPOOK Cataloguer, see sec. 5.2, has been deployed. Since then the observations performed by ART are collected and processed into objects inside the catalogue. Autonomously, every morning a new observation plan is created and add to the telescope's scheduler in the evening. This single observer configuration and the limits imposed by the mount allow a good coverage of the GEO accessible objects, daily observed in a GEO fence configuration and of the GPS objects. The latter are twice per day observed for sensor calibration purposes. A visualization of the objects collected inside the catalogue is proposed in Fig. 6.18. The four diagrams represent the full orbits calculated during the cataloguing activity, considering all together also objects that expired (because not observed further) as of the date in the title: 19th November 2021.

The automatic observation plan has been realized with a greedy-method optimization of the possible objects to be maintained. A dedicated priority has been given to different orbital classes and objects of interest (e.g. the light curves objects). The
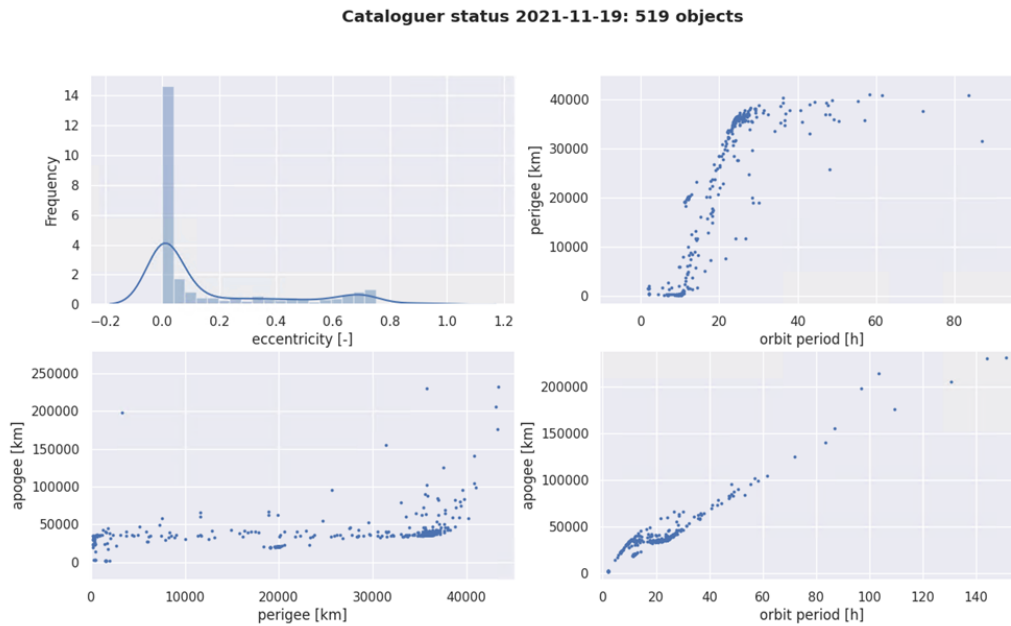
FIGURE 6.18: Visualization of the Airbus catalogue object distribution in terms of eccentricity, perigee, apogee and orbital period.

limit of the cataloguer are quite visible looking at the object growth trend in Fig. 6.19. Starting from the date of formal catalogue initialization on July 2021, are notable three distinct abrupt drops in the catalogue object counter. They corresponds to relative long (more than one week) period of time in which no observations have been performed by ART, due mainly to weather conditions and holidays. It is quite visible that a single week of missed observations corresponds to a complete drop of the objects maintained inside the catalogue.

6.3.1   Space Traffic Management

Space traffic management is of vital importance for the sustainability of the space operations and its further development. SST is key to ensure this objective, providing the necessary data to perform collision avoidance and fragmentation detection.
Since 2020 SPOOK has been integrated with a built-in conjunction assessment capability to perform conjunction screening and probability of collision computation. This system, built on top of an up-to-date catalogue of objects can provide in time warning of close conjunctions between objects and possible collisions. The observation scheduling tools presented in the previous chapters can be applied to this kind of scenario: to perform surveillance of close conjunction and cataloguing of the fragments in case of catastrophic collision. In particular in 4.2.3.1, the VD algorithm can be used to perform observation scheduling of the fragments as support for catalogue creation. To understand the amount of collision warnings that may be predicted on a singly night time span, Fig. 6.20 is the result of a screening analysis of a night in July 2021. In Fig. 6.20, the results obtained with the SPOOK's
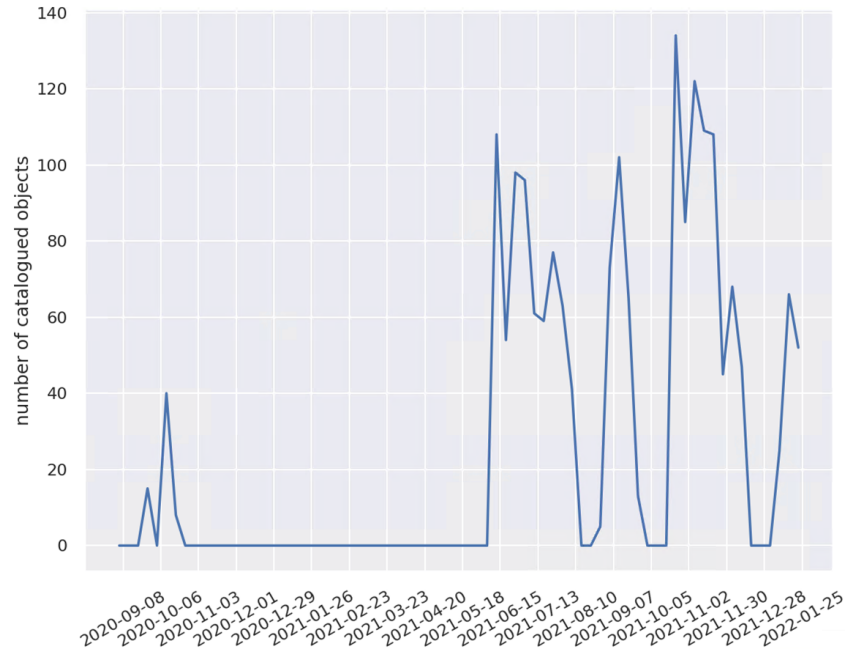
FIGURE 6.19: Visualization of the catalogue object trend during the cataloguer activity.
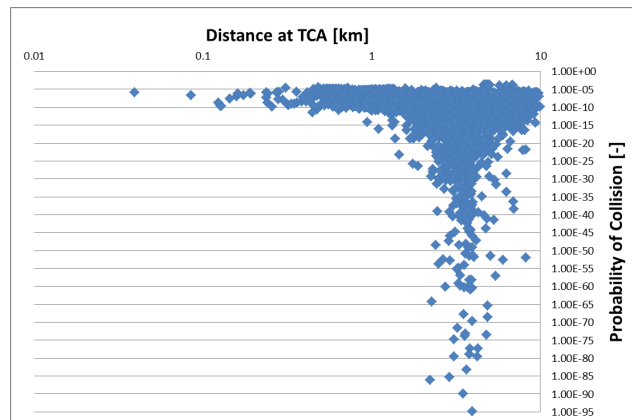
FIGURE 6.20: Probability of collision in logarithmic scale in relation to the minimum distance at *Time of Closest Approach* (TCA).

FIGURE 6.21: Example of close passage between two objects as a result of a conjunction survey. Credits: ART in [4].

conjunction assessment tool, giving as input 10787 LEO objects from space-track for 14 hours of propagation during the night of the 1st July 2021.

The number of close passages between objects in a ellipsoid of 10 km in tangential direction and 4 km in the other two directions, gives as results an amount of ~ 4358 conjunctions.

6.3.1.1   Survey of Conjunctions

As presented in 4.2.2.4, the default ART cataloguer plan can be enriched with an automatic selection of conjunction survey tasks. Depending on the area of interest, e.g., LEO region below 1000 km of orbit altitude and the sensor available, e.g., ART, the number of visible conjunctions can be extremely reduced and allows an easy integration inside a normal CM plan.

This is the case for the example presented in Fig. 6.20, where out of 4358 estimated conjunctions, only 13 conjunctions have been estimated to be visible and detectable. Each survey task at such a short orbit altitude, below 1000 km, requires around 20 s of survey time. In total the original CM plan has been affected of only 4 mins and 30 s of conjunction surveys. In Fig. 6.21, is presented an example of a conjunction survey as observed with ART.

6.3.1.2   Survey of Fragmentation Events

As presented by the author in [38], the VD algorithm finds immediately a suitable application for fragmentation detection and cataloguing.

As simulation scenario, it has been selected a hypothetical catastrophic event of a collision between two LEO objects: the micro-satellite *SEDSAT 1* NORAD 25509 and the Starlink satellite 1730 NORAD 46563. The close conjunction happened on 24th of June 2021 at 18:07:16. The conjunction has been predicted with the new SPOOK's conjunctions screening tool, [4] [36]. The predicted absolute relative distance at time of conjunction was 90.94 m with a relative velocity of $5.7260\,\mathrm{km\,s^{-1}}$. Accordingly to the literature [28], a collision can be considered to be catastrophic when the
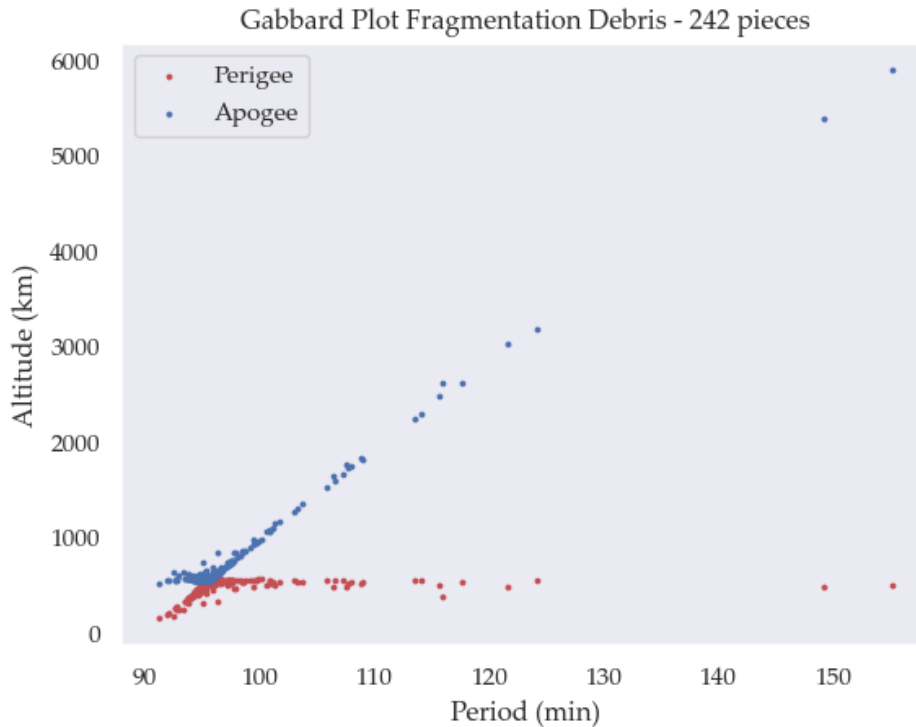
FIGURE 6.22: Gabbard plot of the debris distribution originated after a simulated collision.

ratio between the kinetic velocity of the projectile and the mass of the satellite is over $40\,000\,\mathrm{J\,kg^{-1}}$. Threshold largely reached in this case. The fragmentation event has been simulated with the SPOOK's fragmentation tool that uses the same fragmentation model of NASA's EVOLVE 4.0 as presented in [22].

The fragmentation tool has been developed by the author to fulfil this analysis, and it has been validated through comparison with known collisions.

The fragmentation results are visible in the Gabbard plot in Fig.s 6.22, 6.23 and 6.24. In Fig. 6.22is shown the Gabbard plot of the debris distribution originated after the simulated collision between object NORAD 46563, considered as the target, and the object NORAD 25509, considered as the projectile on 24th of June 2021 at $18:07:16$. The Gabbard plot shows the distribution of apogee and perigee radii for all the fragments of the collision.

For this simulation, a 7-sensors[1] network has been considered, as visible in Tab. 6.4, where are listed their characteristics and locations. For simplicity of the simulation, the Starlink satellite has been considered to have a mass of $260\,\mathrm{kg}$ and a characteristic length of $5\,\mathrm{m}$. The results of the fragmentation simulation totally found 262 objects greater than $10\,\mathrm{cm}$. The physical properties, visible in Fig. 6.24, have been used as an initialization parameter for each object for the next simulation, during which the

---

[1]The sensors used in this work are to be considered not real. Selected by the author accordingly to the principle of the best coverage in the 5 continents.

Table 6.4: Characteristics of the sensors used during the simulations:

Name	Coordinates	FOV dimension	Sensor accuracy
ART	$-6.63°$W $38.22°$N	$\varnothing = 2.43\,\text{deg}, 1.38\,\text{deg}$	$\sigma_\alpha = 0.5'', \sigma_\delta = 0.5''$
CG_AUS_1	$145.786°$W $-27.481\,05°$N	$\varnothing = 3.0\,\text{deg}, 3.0\,\text{deg}$	$\sigma_\alpha = 1'', \sigma_\delta = 1''$
CG_FPO_1	$-149.4826°$W $-17.6641°$N	$\varnothing = 3.0\,\text{deg}, 3.0\,\text{deg}$	$\sigma_\alpha = 1'', \sigma_\delta = 1''$
CG_FGU_1	$-53.4916°$W $3.6685°$N	$\varnothing = 3.0\,\text{deg}, 3.0\,\text{deg}$	$\sigma_\alpha = 1'', \sigma_\delta = 1''$
CG_ARG_1	$-69.0801°$W $-35.8522°$N	$\varnothing = 3.0\,\text{deg}, 3.0\,\text{deg}$	$\sigma_\alpha = 1'', \sigma_\delta = 1''$
CG_USA_1	$-76.1975°$W $41.1947°$N	$\varnothing = 3.0\,\text{deg}, 3.0\,\text{deg}$	$\sigma_\alpha = 1'', \sigma_\delta = 1''$
CG_SCA_1	$-14.042°$W $28.310\,89°$N	$\varnothing = 3.0\,\text{deg}, 3.0\,\text{deg}$	$\sigma_\alpha = 1'', \sigma_\delta = 1''$
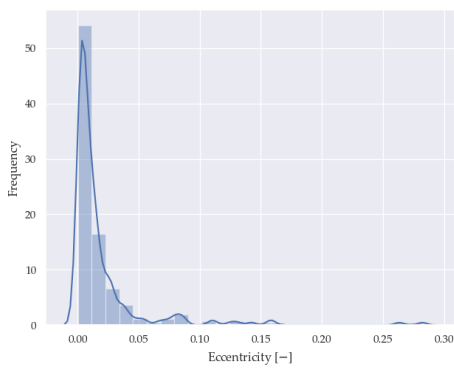
FIGURE 6.23: Eccentricity distribution of the orbits of the fragments result of the collision.
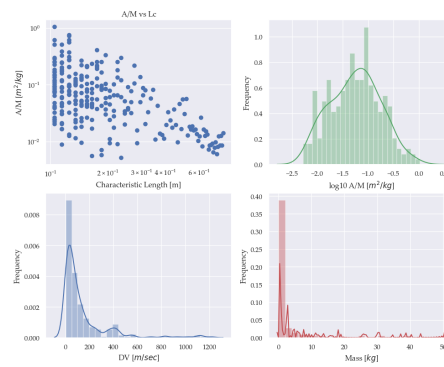
FIGURE 6.24: Physical properties' distribution of the collision debris.

objects generated will be propagated for a time span of 10 days from the epoch of the collision. Looking at Fig. 6.24:

- On the top left: the distribution of the Area-to-Mass A/M ratio in logarithmic scale with respect to the characteristic size of the object.

- On the top right: the count of objects for each A/M ratio value.

- On the bottom left: the distribution of fragments accordingly to the Δv perturbation of the Debris from the master object (the Starlink satellite).

- On the bottom right: the distribution trend of the objects accordingly to their Mass.

A visualization rendering of the propagation of the debris positions after the collision at two different time steps is visible in Fig.s 6.25 and 6.26. This simulation is so composed:

1. First, the collision's debris are propagated for all the simulation time.

2. During the collision, the sensors are simulated to point in the direction of the conjunction (if accessible). See, conjunctions planner of SPOOK in [36] and sec. 4.2.2.4.

FIGURE 6.25: Fragment debris orbit visualization 1 hour after after the collision event.

FIGURE 6.26: Fragment debris orbit visualization 7 hours later the collision event.

3. Observations are simulated for the first sensor who is able to observe the immediate new passage of the debris cloud after the collision. In that case, it was the Argentinian observer *CG_ARG_1*.

4. To be conservative, out of the whole set of 262 observable debris, only a 20% of them has been considered able to generate successfully linked tracklets. And 50 tracklets have been considered as first set of measurements to set the VD algorithm, as in Fig. 4.7.

5. The observations have been simulated as follows:

   - Processing time of 6 hours (to be conservative);
   - Observation by the full network for 1 day.

The simulation has been done for 10 consecutive days of observation, from 25-06-2021 to 07-07-2021.

All the observations have been planned to be sidereal with a $0.1\,\text{s}$ exposure time. In this way the trailing losses are reduced to minimum and the observers do not need to perform active tracking of such fast objects.

In Fig. 6.27 it is shown an example of CAR region obtainable from a short arc observation of a fragment object. For all the simulations, the minimum tracklet length for a short arc to be processable has been considered to be 3 measurements. For safety reasons, the first measurement in a tracklet has always been neglected, since it is usually associated with the maximum noise level. The 2nd and 3rd measurements are used to compute the first CAR area, using the following constraints:

- minimum range from the observer: $0.03 \cdot R_{Earth} \approx 191.34\,\text{km}$;

- maximum range from the observer: $3 \cdot R_{Earth} \approx 19\,134\,\text{km}$;

- maximum eccentricity: 0.25;

- minimum semi-major axis: $6500\,\text{km}$;

- maximum semi-major axis: $16\,000\,\text{km}$.
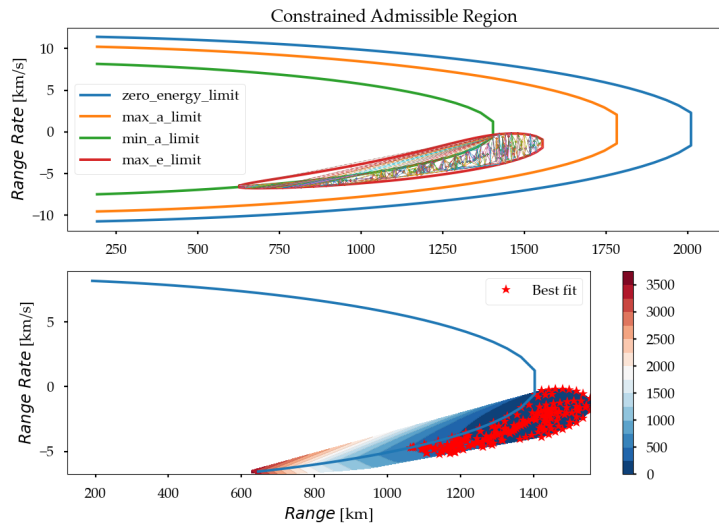
FIGURE 6.27: LEO example of a CAR. Generated by one of the observed fragments by observer in Argentina on $24^{(th)}$ June 2021.

The typical length of a tracklet is between 3 and 5 measurements. The results of this simulation, partially shown in Fig.s 6.28 and 6.29, are a total of 230 objects (out of the 240 objects with eccentricity below 0.25 originated from the fragmentation) observed. Among them, only 178 debris have been observed more than 3 times in 3 different passages, that is the condition for a proper *Tracklet-to-Tracklet* correlation initialization (see Fig. 4.6). The 90% of the observed debris, around 208 objects, have been observed at least two times. These results may increase further if the VD algorithm would be initialized with an higher number of tracklets after the fragmentation event, instead of the 20% of tracklets utilized in this simulation, and considering less restrictive processing times. In this simulation, the processing of short arcs for the VD algorithm has been considered to be operated with a centralized processing unit and considering a total of 6 hours of time span to process the images, collect the measurements and execute the VD algorithm pipeline.

6.4 Dynamic Tracking

One of the most challenging task for a robust SST scenario is to implement a functional real-time controller for a specific sensor. One idea of real-time controller is the so-called *stare-and-chase* scenario. A development of this functionality and its integration inside SPOOK has been proposed in Thesis [26], supervised by the author.
The integration inside SPOOK has been possible through the realization of an image simulator, able to recreate astronomical images of objects propagated with SPOOK as observed by a given sensor. A representation of this simulation framework is presented in the block diagram in Fig. 6.30. The *stare-and-chase* scenario is specific type of survey observation mode in which the sensor is initially supposed to point
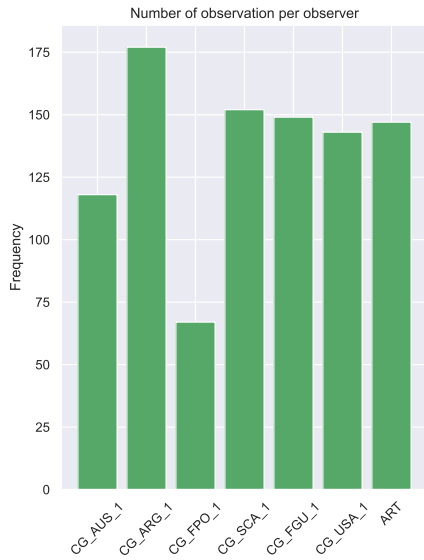
FIGURE 6.28: Number of observations for each observer during all the simulation.
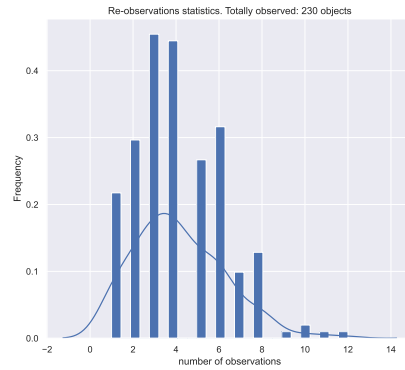
FIGURE 6.29: Observation statistics of revisits for all the observed debris.
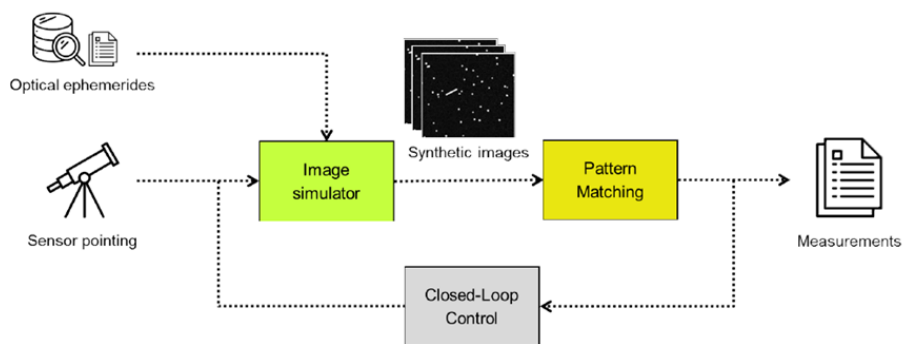
FIGURE 6.30: Closed-loop simulation framework for the auto-tracker campaign. Credits: [26].

(or stare) in a fixed direction in the sky looking for objects of interests that as soon as cross the FOV they begin to be tracked and observed thoroughly their visibility arc. A detailed representation of the auto-tracker loop is proposed in Fig. 6.31.
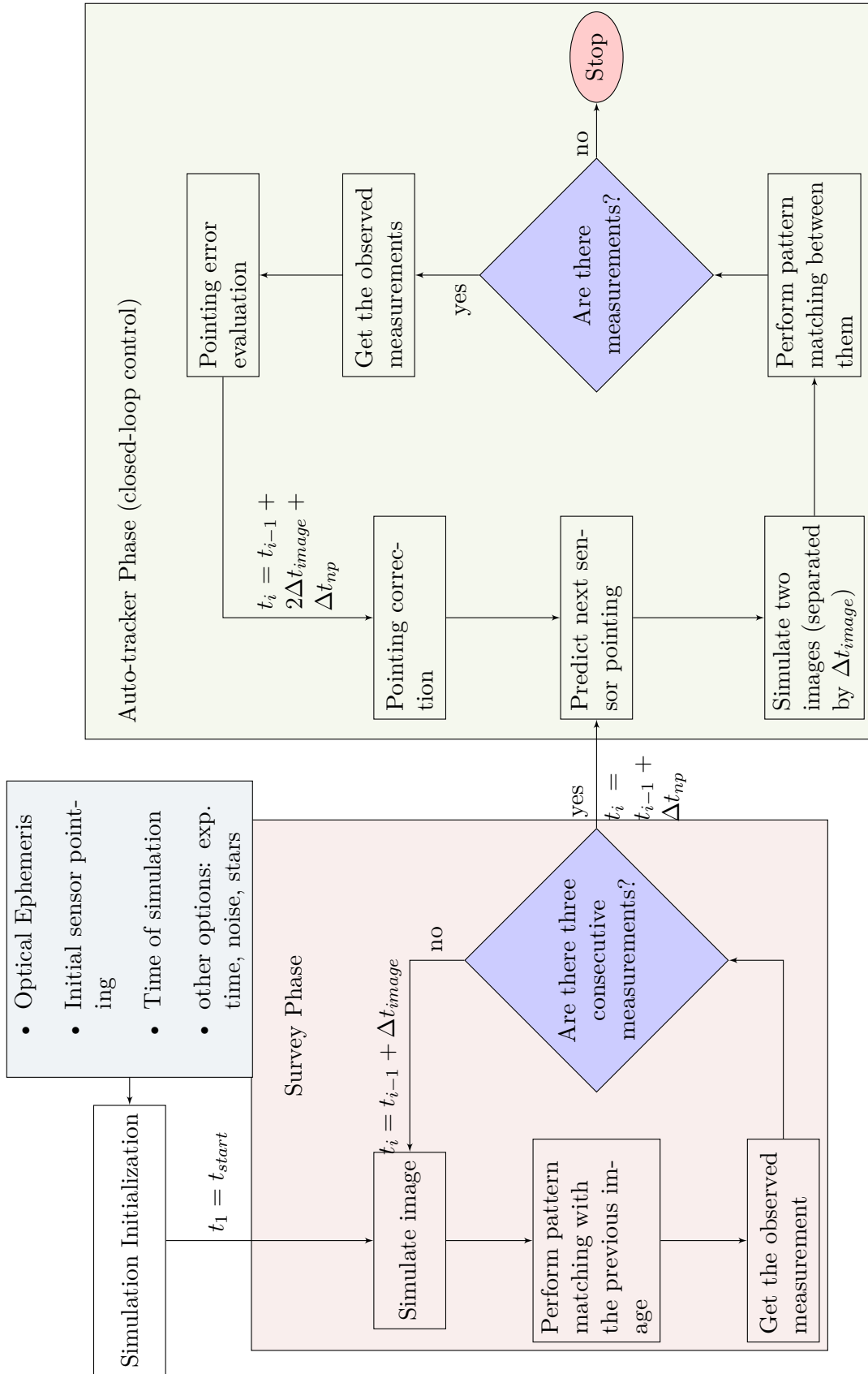
FIGURE 6.31: Block-diagram schematization of the stare-and-chase scenario presented in 6.4.

This work tried to find a point of contact between the cataloguing state-of-the-art and the observation scheduling strategies. Most of the new technologies applied for the post-processing of measurements can have a direct influence also on the way the observations are planned. This thesis pointed its focus on how, and with which limitations, some of the classical cataloguing tools can be applied to simulated scenarios to trigger a possible decision-making algorithm to schedule new observations. So has been done in chapter 3, where multi-target finite statistics methods, currently utilized for the real-time processing of tracking data, can be utilized for the scheduling task of a sensor network.

Similarly, in chapter 4, correlation methods have been used to generate a set of possible pointing directions to attempt the follow-up of uncatalogued objects.

As symbolically represented in Fig. 7.1, and presented in chapter 1, the Thesis found
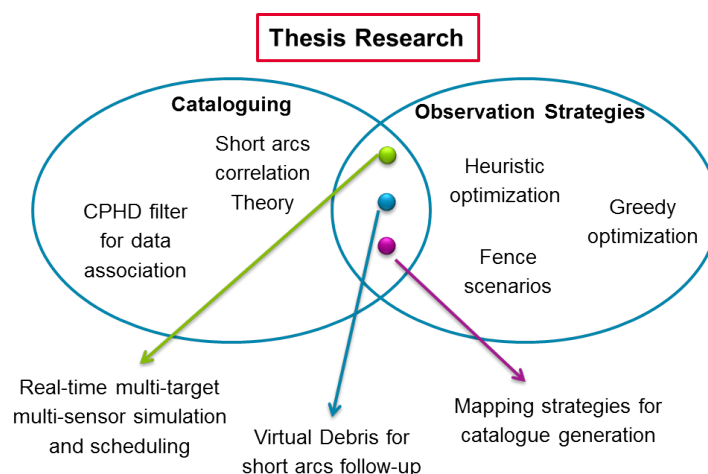
FIGURE 7.1: Analytical approach to optimization of observation strategies for cataloguing.

some points of contact between the cataloguing studies and observation strategies research. These innovations have been:

- The application of FISST-based multi-target filters to the sensor scheduling problem, simulating measurements to select the best pointing direction in terms of gain of information for a catalogue.

- The application of up-to-date techniques for IOD and correlation into the scheduling problem to allow the follow-up of short arc observations.

- The combination of survey observation strategies with post-processing techniques to improve the CG abilities for events of interest; in the case this is realized in real-time, the *stare-and-chase* scenario has been validated to be possible, and for centralized processing systems the combination of mapping strategies and VD algorithm showed a valid application for fragmentation detection and coverage.

The studies presented in this Thesis have a good range of possible applications since have been designed taking always into account their practicality. This pragmatic approach to observation strategies allowed to see the cataloguing operations from a new point of view: of trying to observe what can be processed. The current literature, which has been instead based on the idea of trying to process what has been observed, reached a high level of accuracy in estimation but (if outside simulation scenarios) lacks practicability, being always substantially unable to predict what is going to be observed. Anyway, the limitations of the new theories introduced with this Thesis are still many. The CM algorithms showed to have a good application for small catalogues and network scenarios. This is the case of the *greedy-method* applied in the Airbus autonomous cataloguer as to the default scheduling tool, where in this case the sensor was only one and there were a few hundred objects to be maintained. This is the case also with the CPHD-based filter, that has been applied to small networks and the GEO catalogue. The application of these theories to a comprehensive space-debris catalogue is still challenging, both from practical constraints in sensor communications and computational capabilities that are hard to recreate.

To conclude, the Operations of a network of sensors should find an optimal trade-off between CM activities and CG tasks. Sensors should be ready to change and mutates their operations in case of unexpected events. A good sensor autonomy is connected with a low computational effort (stare-and-chase scenario).

7.1 Future Work

The aforementioned limitations of the new theories could be overcome with the realization of bigger scenarios simulations and high power computational resources. The combinatorial essence of the scheduling problem involves the allocation of all the possible resources, if the bigger-sized problem can be analysed, different and more performant observation scenarios could be studied.

One first aspect that would be essential to be studied, if more resources were available, is the CM and CG for a comprehensive LEO catalogue. As shown in chapter 6, the mapping survey approaches can give already a good level of analysis of the possible coverage of LEO objects by a space-based sensor. However, together with the involvement of space-based facilities different problems, from the point of view of centralized controllability, are arising. If assuming a sensor able to slew and steer, not completely passive as in the aforementioned example, a certain level of autonomy shall be guaranteed to the sensor itself. Low computational power and fast reaction time, would suggest the implementation of techniques similar to the presented *stare-and-chase* scenario. In those cases, full processing of the images would not be required nor the connection to a full catalogue. The results of this first raw processing together with the full images obtained can be downloaded offline to a centralized unit for further processing with the most advanced techniques.
To overcome also the practicability constraints of some of the state-of-the-art techniques in front of bigger sensor networks and catalogues (the reader can recall the ESA model estimation of 130 million of debris on orbit), new and not-analytical techniques could be studied: like machine learning techniques. In that scenario a comprehensive and centralised catalogue can be initially trained starting from images and results of smaller catalogues collected by different users and SST systems, as is the actual situation, and use the acquired knowledge to process more sensing data all at once and schedule efficiently new observations, eventually in real-time.

As for the Airbus framework, the future works that can be the direct continuation of this Thesis are:

- Integration of real-time autonomous scheduler inside SPOOK cataloguer.

- streamline of cataloguing activities to incorporate the advantages of the scheduling outputs.

Bibliography

[1] John Africano, Thomas Schildknecht, Mark Matney, Paul Kervin, Eugene Stansbery, and Walter Flury. A geosynchronous orbit search strategy. *Space Debris*, 2(4):357–369, 2000. ISSN 1572-9664. doi: 10.1023/B:SDEB.0000030025. 04930.08.

[2] G. Beutler. *Methods of Celestial Mechanics: Volume I: Physical, Mathematical, and Numerical Principles*. Number 1. Springer-Verlag Berlin Heidelberg, 2005. ISBN 9783540268703. doi: 10.1007/b138225.

[3] CFSCC CJ3/6. Space-track.org, 2022. URL https://www.space-track.org/. Visited on 2021-01-19.

[4] Giovanni Cirillo, Maria GV Dimitrova, Jens Utzmann, Yannick Heinz, Guido Pedone, and David Vallverdu Cabrera. Performance evaluation of the airbus robotic telescope and the spook data processing framework. In *Proceedings of the 8th European Conference on Space Debris*, page 58, 2021.

[5] A. Console. Command and control of a multinational space surveillance and tracking network. *Joint Air Power Competence Centre (JAPCC): Kalkar, Germany*, 2019. doi: 10.34688/2019/0081.

[6] Howard Curtis. *Orbital Mechanics for Engineering Students*, volume 1 of *Mechanical Engineering Series*. Springer-Verlag Berlin Heidelberg, 2nd edition, 2005. ISBN 9789896540821. doi: 10.1016/C2011-0-69685-1.

[7] Emmanuel Delande, Carolin Frueh, Jose Franco, Jérémie Houssineau, and Daniel Clark. Novel multi-object filtering approach for space situational awareness. *Journal of Guidance, Control, and Dynamics*, 41(1):59–73, 2018. ISSN 07315090. doi: 10.2514/1.G002067.

[8] Kyle J. DeMars and Moriba K. Jah. Probabilistic initial orbit determination using Gaussian mixture models. *Journal of Guidance, Control, and Dynamics*, 36(5):1324–1335, 2013. ISSN 15333884. doi: 10.2514/1.59844.

[9] Joachim Ender, Ludger Leushacke, Andreas Brenner, and Helmut Wilden. Radar techniques for space situational awareness. In *2011 12th International Radar Symposium (IRS)*, pages 21–26. IEEE, 2011.

[10] ESA: Space Safety. SPACE SURVEILLANCE AND TRACKING - SST SEGMENT, 2017. URL https://www.esa.int/Our_Activities/Space_Safety/Space_Surveillance_and_Tracking_-_SST_Segment. Visited on 2019-08-20.

[11] Davide Farnocchia, Giacomo Tommei, Andrea Milani, and Alessandro Rossi. Innovative methods of correlation and orbit determination for space debris. *Celestial Mechanics and Dynamical Astronomy*, 107(1):169–185, 2010. ISSN 09232958. doi: 10.1007/s10569-010-9274-6.

[12] O. Rodriguez Fernandez, J. Utzmann, U. Hugentobler, Airbus Defence, and Space GmbH. Correlation of optical observations to cataloged objects using multiple hypothesis filter. In *Proc., 1st NEO and Debris Detection Conf., edited by T. Flohrer, R. Jehn, and F. Schmitz. Darmstadt, Germany: ESA Space Safety Programme Office*, pages 22–24, January 2019.

[13] Oscar Rodriguez Fernandez, Jens Utzmann, and Urs Hugentobler. Spook: A comprehensive space surveillance and tracking analysis tool. *Acta Astronautica*, 158:178–184, 2019. doi: 10.1016/j.actaastro.2018.02.008.

[14] Justin Fletcher, Ian McQuaid, Peter Thomas, Jeremiah Sanders, and Greg Martin. Feature-based satellite detection using convolutional neural networks. In *Proceedings of the Advanced Maui Optical and Space Surveillance Technologies Conference*, page 11, 2019.

[15] José Freitas, João Fidalgo Neves, Raúl Domínguez-Gonzalez, Jaime Nomen, Miguel Santos, Margarida Vieira, Nuno Ávila Martins, and Noelia Sanchez Ortiz. Portuguese sst capability-the portuguese space surveillance network system. In *Proceedings of the 8th European Conference on Space Debris*, page 131, 2021.

[16] C. Frueh, H. Fiedler, T. Schildknecht, and J. Herzog. Multi-Target Tracking for SMARTnet: Multi-Layer Probability Hypothesis Filter for Near-Earth Object Tracking. In *Proceedings of the 8th European Conference on Space Debris*, number May, pages 20–23, 2021.

[17] Carolin Frueh, Hauke Fielder, and Johannes Herzog. Heuristic and optimized sensor tasking observation strategies with exemplification for geosynchronous objects. *Journal of Guidance, Control, and Dynamics*, 41(5):1036–1048, 2018. ISSN 07315090. doi: 10.2514/1.G003123.

[18] Carolin Frueh, Bryan Little, and John McGraw. Optical sensor model and its effects on the design of sensor networks and tracking. In *Proceesings of the Advanced Maui Optical and Space Surveillance Technologies Conference (AMOS) (Sept. 2019)*, 2019. doi: 10.1109/AMOS46465.2019.9047790.

[19] Steven Gehly and James Bennett. Incorporating target priorities in the sensor tasking reward function. In *Proceedings of the Advanced Maui Optical and Space Surveillance Technologies Conference, Maui, Hawaii, USA*, number 34, 2016.

[20] Michael T. Goodrich and Roberto Tamassia. *Algorithm Design and Applications*, volume 363. Wiley Hoboken, 2015. ISBN 978-1-118-33591-8. doi: 10.1002/9781118335918.

[21] Hao-ran Ji and Guo-qiang Zeng. A method for spatial effective coverage analysis in space-based optical observation. *Optik*, 166:116–126, 2018. ISSN 00304026. doi: 10.1016/j.ijleo.2018.04.012.

[22] Nicholas L. Johnson, Paula H. Krisko, J-C. Liou, and Phillip D. Anz-Meador. Nasa's new breakup model of evolve 4.0. *Advances in Space Research*, 28(9): 1377–1384, 2001. ISSN 0273-1177. doi: 10.1016/S0273-1177(01)00423-9.

[23] T. S. Kelso. A new way to obtain gp data (aka tles), 2022. URL https://celestrak.com/NORAD/documentation/gp-data-formats.php. Visited on 2022-01-25.

[24] Bryan Little and Carolin Frueh. Comparison of optimizers for ground-based and space-based sensors. In *Proceedings of the Advances in the Astronautical Sciences*, volume 162, 2018. ISBN 9780877036456. doi: 10.2514/6.2018-2046.

[25] Bryan D Little and Carolin Frueh. Ssa sensor tasking: comparison of machine learning with classical optimization methods. In *Proceedings of the Advanced Maui Optical and Space Surveillance Technologies Conference*, pages 1–17, 2018.

[26] Juan Francisco Lopera Zafra. Simulation and validation of an auto-tracker campaign. 2021. Master Thesis completed in Airbus under the supervision of Guido Pedone.

[27] Robert E. Melchers and André T. Beck. *Structural Reliability Analysis and Prediction*, volume 2. John Wiley & Sons, 2018. ISBN 9780471983248. doi: 10. 1002/9781119266105. Chapter C: Bivariate and Multivariate Normal Integrals, pages 415–427.

[28] A. Milani, D. Farnocchia, L. Dimare, A. Rossi, and F. Bernardi. Innovative observing strategy and orbit determination for Low Earth Orbit space debris. *Planetary and Space Science*, 62(1):10–22, 2012. ISSN 00320633. doi: 10.1016/ j.pss.2011.11.012.

[29] Andrea Milani and Giovanni F. Gronchi. *Theory of Orbit Determination.* 2008. ISBN 9780521873895. doi: 10.1017/CBO9780511802681.

[30] Andrea Milani, Giovanni F. Gronchi, Mattia De Michieli Vitturi, and Zoran Knežević. Orbit determination with very short arcs. I admissible regions. *Celestial Mechanics and Dynamical Astronomy*, 90(1-2):59–87, 2004. ISSN 09232958. doi: 10.1007/s10569-004-6593-5.

[31] Reto Musci, Thomas Schildknecht, Tim Flohrer, and Gerhard Beutler. Concept for a catalogue of space debris in geo. In *Proceedings of the 4th European Conference on Space Debris*, volume 587, page 601, 2005.

[32] Kevin M Nastasi and Jonathan Black. An autonomous sensor management strategy for monitoring a dynamic space domain with diverse sensors. In *In collection of the 2018 AIAA Information Systems-AIAA Infotech@ Aerospace*, page 0890. 2018. doi: 10.2514/6.2018-0890.

[33] Victor P. Osweiler. Covariance estimation and autocorrelation of norad two-line element sets. 2006. doi: 10.2514/1.22459. Thesis and Dissertation from the Air Force Institute of TechnologyAir.

[34] Panos M. Pardalos, Robert Murphey, and Don Grundel. *Theory and Algorithms for Cooperative Systems*, volume 4. World Scientific, 2004. ISBN 978-9812386413. doi: 10.1142/9789812702722.

[35] Guido Pedone. Strategies and data processing for the optical observation of space debris. 2019.

[36] Guido Pedone, David Vallverdu Cabrera, Maria Gloria Dimitrova Vesselinova, Giovanni Cirillo, Yannick Heinz, Fabian Schiemenz, and Jens Utzmann. SPOOK: A tool for space objects catalogue creation and maintenance supporting space safety and sustainability. *Acta Astronautica*, 188(1):89–98, 2021. ISSN 00945765. doi: 10.1016/j.actaastro.2021.07.026.

[37] Guido Pedone, Jens Utzmann, and Roger Förstner. Baseline algorithm definition for a future real-time autonomous sensor scheduling strategy for sst. In *Proceedings of the 8th European Conference on Space Debris*, page 59, 2021.

[38] Guido Pedone, Jens Utzmann, and Roger Förstner. Survey on new strategies and state of the art for space debris catalogue generation for optical sensor networks. In *Proceedings of the 19th Advanced Maui Optical and Space Surveillance (AMOS) Technical Conference*, number 1, 2021.

[39] Joseph N. Pelton. Tracking of orbital debris and avoidance of satellite collisions. *Handbook of Satellite Applications*, 1:1–13, 2016. doi: 10.1007/978-1-4614-6423-5_106-2.

[40] Branko Ristic, Ba Ngu Vo, and Daniel Clark. A note on the reward function for PHD filters with sensor control. *IEEE Transactions on Aerospace and Electronic Systems*, 47(2):1521–1529, 2011. ISSN 00189251. doi: 10.1109/TAES.2011.5751278.

[41] Fabian Schiemenz, Jens Utzmann, and Hakan Kayal. Adaptive Gaussian Mixture based Orbit Determination with combined atmospheric density uncertainty consideration. *Advances in Space Research*, pages 1–32, 2020. ISSN 02731177. doi: 10.1016/j.asr.2020.05.042.

[42] T. Schildknecht. The search for space debris objects in high-altitude orbits. *Astronomical Institute, University of Bern*, 2003. doi: 10.1007/s12036-008-0035-0.

[43] Thomas Schildknecht, U. Hugentobler, and M. Ploner. Optical surveys of space debris in geo. *Advances in Space Research*, 23(1):45–54, 1999. doi: 10.1016/S0273-1177(99)00884-8.

[44] Thomas Schildknecht, Alessandro Vananti, Emiliano Cordelli, and Tim Flohrer. Esa optical surveys to characterize recent fragmentation events in geo and heo. In *Proceedings of the Advanced Maui Optical and Space Surveillance (AMOS) Technologies Conference*, page 34, 2019.

[45] S. W. Sloan. A fast algorithm for constructing Delaunay triangulations in the plane. *Advances in Engineering Software (1978)*, 9(1):34–55, 1987. ISSN 01411195. doi: 10.1016/0141-1195(87)90043-X.

[46] Spaceforce. Ussf announces initial operational capacity and operational acceptance of spa, 2021. URL https://www.spaceforce.mil/News/Article/2129325/ussf_announces_initial_operational_capability_and_operational_acceptance_of_spa/. visited on 2022-01-25.

[47] Jens Utzmann, MG Dimitrova Vesselinova, and O Rodriguez Fernandez. Airbus robotic telescope. In *Proceedings of the 1st NEO and Debris Detection Conference, Darmstadt, Germany*, pages 22–24, 2019.

[48] David A. Vallado. *Fundamentals of Astrodynamics and Applications*, volume 12. Springer Science & Business Media, 2001. doi: 10.1007/978-3-319-31367-4.

[49] Ba Ngu Vo and Wing Kin Ma. The Gaussian mixture probability hypothesis density filter. *IEEE Transactions on Signal Processing*, 54(11):4091–4104, 2006. ISSN 1053587X. doi: 10.1109/TSP.2006.881190.

[50] Ba Tuong Vo, Ba Ngu Vo, and Antonio Cantoni. Analytic implementations of the cardinalized probability hypothesis density filter. *IEEE Transactions on Signal Processing*, 55(7 II):3553–3567, 2007. ISSN 1053587X. doi: 10.1109/TSP.2007.894241.

[51] E.A. Wan and Rudolph Van Der Merwe. The unscented Kalman filter for nonlinear estimation. *Adaptive Systems for Signal Processing, Communications, and Control Symposium 2000. AS-SPCC. The IEEE 2000*, (3):153–158, 2002.

[52] Brian Weeden. Space situational awareness fact sheet. *Secure World Foundation*, pages 2–3, 2017. Secure World Foundation: www.swfound.org.

[53] Sam Wishnek, Marcus J. Holzinger, Patrick Handley, and Sue Hagerty. Robust Initial Orbit Determination Using Streaks and Admissible Regions. *Journal of the Astronautical Sciences*, 68(2):349–390, 2021. ISSN 21950571. doi: 10.1007/s40295-021-00264-1.

Airbus SSA Department

The work of this Thesis has been conducted within the SSA department in Airbus Defence and Space GmbH, in Friedrichshafen, Germany. In particular, the project has supported the activities of SST team with the development of a dedicated software tool SPOOK, and the observation and maintenance operations with ART. Fig. 1 shows the ART telescope, since 2018 the ART telescope is operative for SST activities commanded remotely by Airbus in Germany. Fig. 2 has been taken during a maintenance visit to the telescope in 2022, from left to right: Dr. Jens Utzmann (project manager), the author Guido Pedone and David Vallverdu Cabrera both PhD students in Airbus.

Both software suite and telescope have been a great validation and testing framework for the new developments introduced with this Thesis. The properties and functionalities of both have been extensively presented in various publications [13], [47], [36] and [4]. ART observations, in particular, supported the validation of various algorithms, e.g. the deployment of cataloguing pipeline, providing real-world optical measurements. While the software SPOOK has been a powerful resource of high-precision tools like SP orbit propagators and measurement estimators.

FIGURE 1: ART facility in Extremadura, Spain.

FIGURE 2: Visit to the telescope facility by some members of the SST team in May 2022.

RTN Frame

The *Radial, Tangential, Normal* (RTN) frame is a commonly used body-fixed reference frame for space objects. It provides a convenient way to describe the relative position and motion of an object with respect to its central body (e.g., a planet, moon, or star). The RTN frame consists of three mutually orthogonal unit vectors: $\hat{R}$ (Radial), $\hat{T}$ (Tangential), and $\hat{N}$ (Normal), as depicted in Fig.3. These vectors are defined as follows:

$\hat{R}$: Radial vector, points outward from the central body, aligned with the radial direction.

$\hat{T}$: Tangential vector, tangent to the object's orbit, along the direction of motion.

$\hat{N}$: Normal vector, perpendicular to the orbital plane, points in orbital angular momentum direction.

The RTN frame is particularly useful for analyzing the relative motion of spacecraft, satellites, or other space objects in orbit around a celestial body. It allows for a
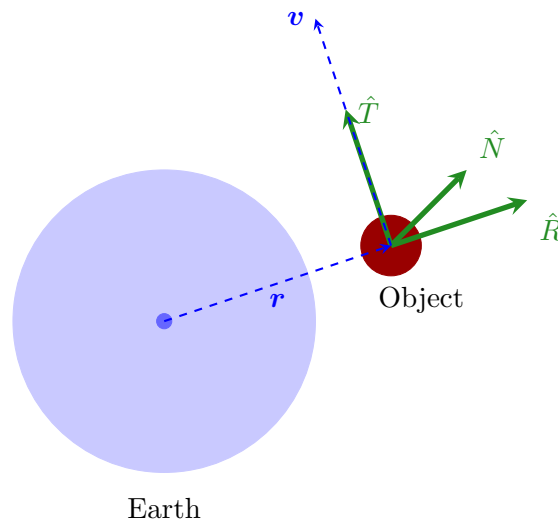
FIGURE 3: Illustration of the RTN (Radial, Tangential, Normal) frame with an orbiting object (sphere) and dashed vectors for r and v.

straightforward decomposition of position and velocity vectors into radial, tangential, and normal components.

In mathematical terms, the RTN frame can be defined as follows:

$$\hat{R} = \frac{\boldsymbol{r}}{\|\boldsymbol{r}\|}$$
$$\hat{T} = \frac{\boldsymbol{v}}{\|\boldsymbol{v}\|}$$
$$\hat{N} = \hat{R} \times \hat{T}$$

Where, $\boldsymbol{r}$ is the position vector from the central body to the space object and $\boldsymbol{v}$ is the velocity vector of the space object. The RTN frame provides a local reference frame that rotates with the object as it moves along its orbit. This rotation ensures that the $\hat{R}$, $\hat{T}$, and $\hat{N}$ vectors remain aligned with their respective directions relative to the object's position and velocity.

The RTN frame is a valuable tool for analyzing the motion of space objects in orbit. It simplifies the description of their position and velocity vectors and is particularly useful in space navigation, guidance, and control applications.